Size Optimization of Magnetic Nanoparticles for Biomedical Applications via a Novel Size-Selective Fractionation Process

by

Hunter Bradley Rogers

A thesis submitted to the Graduate Faculty of
Auburn University
in partial fulfillment of the
requirements for the Degree of
Master of Science

Auburn, Alabama
December 13, 2014

Keywords: Iron Oxide Nanoparticles, Size-Selective Fractionation, Magnetic Resonance
Imaging

Approved by

Allan E. David, Chair, John W. Brown Assistant Professor
Mark E. Byrne, Daniel F. & Josephine Breeden Associate Professor
Elizabeth Lipke, Assistant Professor

Abstract

Magnetic nanoparticles, especially those composed of iron oxide, are extremely attractive options when it comes to MRI contrast agents and magnetically targeted therapies. Their superparamagnetic properties as well as their high magnetic saturation and susceptibility make iron oxide MNPs excellent contrast agents for magnetic resonance imaging (MRI). In addition, their high surface-to-volume ratio enables a high loading of functionalities including imaging agents, targeting moieties, biocompatible ligands, and anticancer drugs. However, the inability to synthesize them in a monodisperse manner above ~20 nm in size has hindered their optimization for *in vivo* use. A novel and efficient approach to the size-selective fractionation of an original magnetic nanoparticle suspension into a number of more distinct size distributions has been developed and used to study the effect of size on the relaxometric properties of the particles. A series of experiments were conducted using particle suspensions of hydrodynamic diameters of 96.3 ± 9.0, 123.6 ± 7.9, and 141.5 ± 10.8 nm obtained from an original polydisperse suspension of nanoparticles to determine the effect of size on the transverse relaxation time (T2) in both aqueous suspensions and tissue mimicking phantom gels using MRI. The use of this size separation technique will allow for important size studies to be conducted in the future that will be critical to the optimization of magnetic nanoparticle for biomedical applications.

Acknowledgements

First and foremost I would like to express the highest levels of gratitude to my wife, Leah Rogers, for her relentless love and support through the entirety of this work and beyond. Thanks to my family, specifically my parents, Edwin and Janice Rogers, for all of their love and support over the years.

This work would have unquestionably been impossible without the guidance of my advisor, Dr. Allan David. Special thanks to all the members of the David Lab, especially Dr. Young Suk Choi for teaching me how to properly grow cells, Tareq Anani and Xin Fan for being there with me from the beginning, Alan Hanley for running a myriad of experiments for/with me, and Alex Kelly for the helicopter and Titan rides. Special thanks to Dr. Ronald Beyers for his assistance with all of the MRI aspects of this work and squeezing me in at the last minute on multiple occasions so that I could finish on time. I would be remiss not to convey my gratitude to Dr. Christopher Roberts for giving me my first research opportunity over 5 years ago which set me on the course I am today. And lastly, thank you to Auburn University and the Chemical Engineering department for being an amazing place to call home for the past six years.

Table of Contents

List of Tables

List of Figures

<center>**Chapter 1**</center>

<center>**Introduction**</center>

1.1 The Current Challenges of Nanomedicine

Nanomedicine refers to a broad area of modern research that focuses on the development of new technologies that utilize nanomaterials for the diagnosis, treatment, and prevention of diseases (Freitas Jr. 1999). The use of nanomaterials in biomedical applications presents the unique opportunity to create engineered materials with highly controlled properties and functions that are comparable in scale to biological molecules and structures (Kim et al. 2010).

Nanomedicine has become an area of great interest and has produced a large number of new technologies ranging from biomimetic nanomaterials, targeted drug delivery systems, and diagnostic imaging agents. However, in contrast to the ever-growing list of nanomaterials being developed for medical applications, the number of these technologies that have been approved for clinical use is very small. This is largely due to an overall paucity of fundamental knowledge and understanding of how the physical and chemical properties of nanomaterials affect their interaction with biological systems (Doane & Burda 2011). The behavior of nanomaterials within biological environments, including their stability and biodistribution, is dependent on their chemical composition and physical properties such as size and geometry (Moghimi et al. 2005). Therefore, in order for nanomaterials to achieve their full potential in *in vivo* and *in vitro*

<center>1</center>

applications, studies must be conducted to identify the underlying principles of nanomaterial properties and the effect on physiological processes and environments. Likewise, methods that allow for the highly controlled alteration of nanomaterial properties, such as size, must be developed to facilitate such studies.

1.2 Iron Oxide Nanoparticles: Properties and Synthesis Methods

Iron oxide nanoparticles are some of the most studied nanomaterials for biological applications due to their unique properties and favorable toxicity profile (Cole et al. 2011). Iron is a naturally present substance within the human body, typically in the range of approximately 3500 mg of iron within a healthy individual at any given time (Corot et al. 2006). Approximately half is contained within hemoglobin for the transport of oxygen in the blood and the other half is contained in ferritin complexes present in all cell types. Synthetic iron oxide nanoparticles are typically produced with a core-shell structure in which the core is composed of some form of iron oxide, such as magnetite (Fe_3O_4) or maghemite (γ-Fe_2O_3), and the shell is composed of a biocompatible material that enables functionalization of the surface.

1.2.1 Properties of IO-MNPs

One of the most desirable properties of iron oxide nanoparticles is their superparamagnetic properties, as illustrated in Fig. 1.1. Superparamagnetism occurs when the size of the particles (i.e. nanoscale) allows thermal fluctuations to cause random flipping of magnetic moments. This random flipping results in an overall average magnetic moment of zero in the absence of an external magnetic field. This property is

ideal for *in vivo* applications as it prevents potential aggregation of particles that could lead to an increased rate of clearance by the mononuclear phagocyte system or could induce thrombosis (Cole et al. 2011). These superparamagnetic properties also induce a strong magnetic distortion around the particles that enables them to be superior contrast agents (Corot et al. 2006).

Superparamagnetic nanoparticle
Diameter < ~30 nm
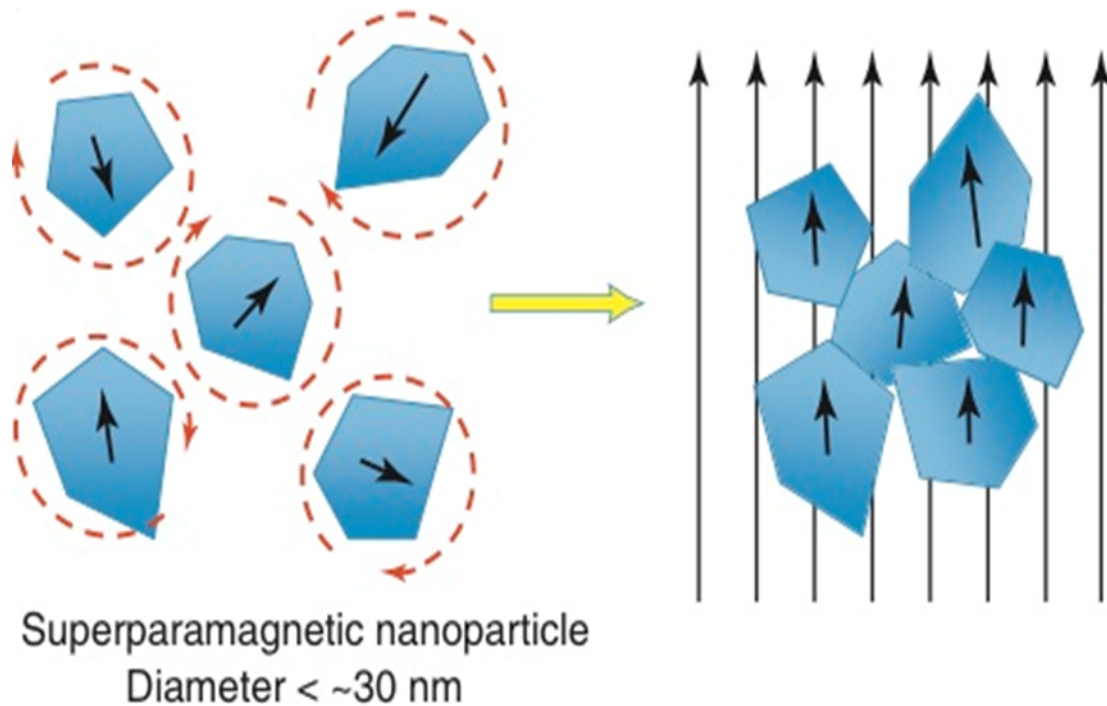
Figure 1.1 Illustration of the superparamagnetic behavior exhibited by iron oxide nanoparticles possessing a single magnetic domain (i.e. ~<30 nm). In the absence of an applied magnetic field, the net magnetization of the particles is zero as seen on the left. However, when a magnetic field is applied, the domains align in the direction of the applied magnetic field resulting in magnetization of the nanoparticles. (Cole et al. 2011).

In addition, iron oxide nanoparticles also possess increased magnetic saturation and susceptibility compared to larger, paramagnetic materials (Cole et al. 2011). This is because the saturation magnetization of the iron oxide nanoparticles decreases with increasing size, which is detrimental to the relaxivity of the nanoparticles when they are being used as contrast agents (Corot et al. 2006). For this reason, MNPs with core sizes larger than 30nm typically are composed of multiple smaller crystals rather than a single large crystal (Cole et al. 2011). To date, there have been several iron oxide nanoparticle based contrast agents that have been approved for clinical use by the FDA including Feridex® and Resovist®, and multiple patents granted for contrast agent platforms using iron oxide nanoparticles (Yoon et al. 2012).

1.2.2 Synthesis of IO-MNPs

Since the first instances of the use of ferromagnetic contrast agents in the late 1980's, many different synthesis methods have been developed for iron oxide nanoparticles (Renshaw et al. 1986). Despite the progress that has been made, there are still many challenges in synthesizing MNPs including: defining experimental conditions that result in reproducible monodispersivity of MNPs, the need for a coating that allows the MNPs to be soluble in aqueous and/or biological media, and scalability (Corot et al 2006). Here we provide some details on the most frequently used techniques for MNP synthesis.

Chemical Precipitation

Chemical precipitation methods are one of the simplest approaches to iron oxide nanoparticle synthesis in which iron oxide MNPs are obtained via the co-precipitation of ferrous and ferric salts in an aqueous medium under a nitrogen environment to prevent oxidation (Burda et al. 2005). There are two primary processes involved in this method, an initial burst of nucleation and then subsequent growth of the crystalline nuclei that is formed (Lodhia et al. 2010). Although the co-precipitation approach enables the production of large quantities of MNPs, the particles are not monodisperse and tend to have fairly wide size distributions. In response to this, the focus has been on optimizing the synthesis conditions, such as Fe^{2+}/Fe^{3+} molar ratio and pH, in order to achieve more monodisperse MNPs. Polymer surface complex agents (e.g. dextran and silica) have also been utilized in the synthesis process to limit the growth of the nuclei (Jolivet et al. 1992; Bautista 2005). In addition to inhibiting growth, the polymers also enable MNP solubility in aqueous/biological media, allow for surface functionalization, and increase the biocompatibility of the MNP complex (Jun et al. 2005). While chemical precipitation is one of the most promising techniques in terms of scalability, the current issues regarding wide size distributions and poor crystallinity must be solved before this approach could be used for mass production of iron oxide MNPs for biomedical applications, especially for their use as MRI contrast agents.

Liposome and Micelle Formation of MNPs

The synthesis of iron oxide MNPs via chemical reactions within lipids structures like those shown in Figure 1.2 is another approach that has been found to be effective.

When iron oxide MNPs are synthesized via liposomes, they are called magnetoliposomes and the iron oxide is either located within the liposome at the center of the structure in an area known as the liposomal lumen or within the lipid bilayer (Bulte et al. 1993; Gonzales et al. 2005). The latter form has been used to produce MRI contrast agents specifically for bone marrow (Bulte et al. 1999). To synthesize these contrast agents, iron oxide nanoparticles are initially created in solution, solubilized, and then stabilized by a surfactant. An excess of phospholipids is then added to the stabilized iron oxide particles and the solution is subjected to dialysis for a period time. During this time, the surfactant on the surface of the particles is exchanged for phospholipid molecules and results in the formation of a bi-lipid layer on the particles (Gonzales 2005).

Additionally, both micelles and reverse micelles can be used to synthesize iron oxide MNPs; however, reverse micelles are of more commonly used for the synthesis of MRI contrast agents (Lodhia et al. 2010). Typically, reverse micelles are created in aqueous iron salt solutions and encapsulated by a surfactant that separates them from the organic phase (Tartaj et al. 2002). It has previously been shown that by controlling the iron salt, surfactant, and solvent concentrations, the particle size can be controlled to produce monodisperse particles in the 2-10nm size range (Lee et al. 2005). However, the use of reaction based synthesis is subject to its own set of challenges including the complex chemistry that can be required to produce the micelles and liposomes. These synthesis methods must be simplified to allow for mass production of these forms of iron oxide nanoparticles
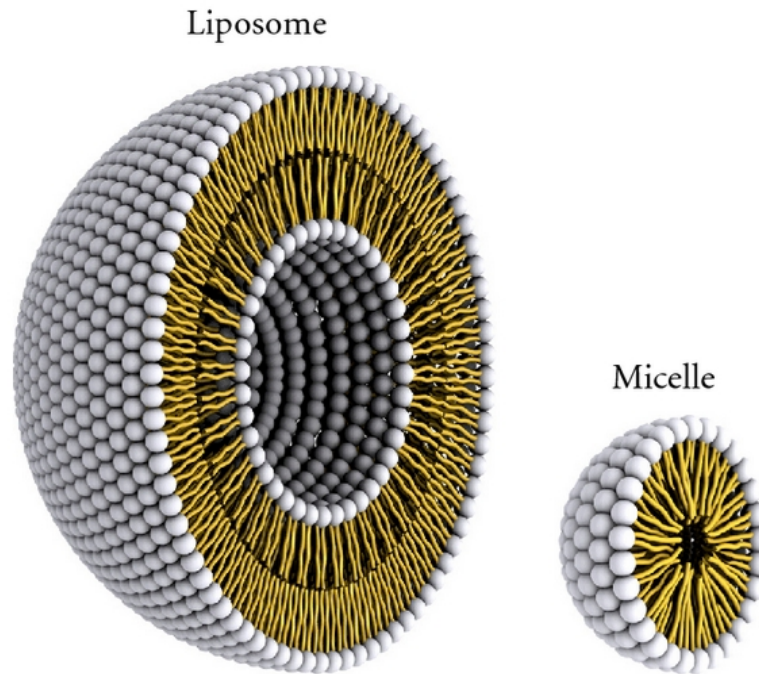
Figure 1.2: A representation of the phospholipid structure of liposomes and micelles. As can be seen, liposomes are constructed of a bilayer of lipids while micelles are composed of a single lipid layer (Bitounis et al. 2011).

Thermal Decomposition

The use of high temperature synthesis methods have proven to be effective at producing iron oxide MNPs that are both monodisperse and possess high crystallinity. This approach relies on the decomposition of iron complexes in the presence of organic solvents and surfactants. Many researchers have had success in synthesizing iron oxide MNPs with small size distributions and good crystallinity properties (Lodhia et al. 2010). Recently, Kim et al. reported their work on the large-scale synthesis of iron oxide nanoparticles to be used as MRI contrast agents using thermal decomposition. The authors were able to successfully synthesize "extremely small" iron oxide nanoparticles (ESIONs) of sizes <4nm via the thermal decomposition of iron-oleate complex in the presence of oleic acid and oleyl alcohol in diphenyl ether, images of which can be seen below in Figure 1.3. The size of the ESIONs was controlled by varying the ratio of oleyl alcohol and oleic acid as well as varying the temperature of the aging step. The aging temperatures were varied from 200°C to 280°C resulting in nanoparticles with averages size in the range of 1.54nm to 3.74 nm, respectively. The authors state that the synthesis process could be easily scaled for the production of "multigrams of nanoparticles" and that ESIONs could easily be functionalized with PO-PEG ligands to make them biocompatible and dispersible in aqueous media (Kim et al. 2011).
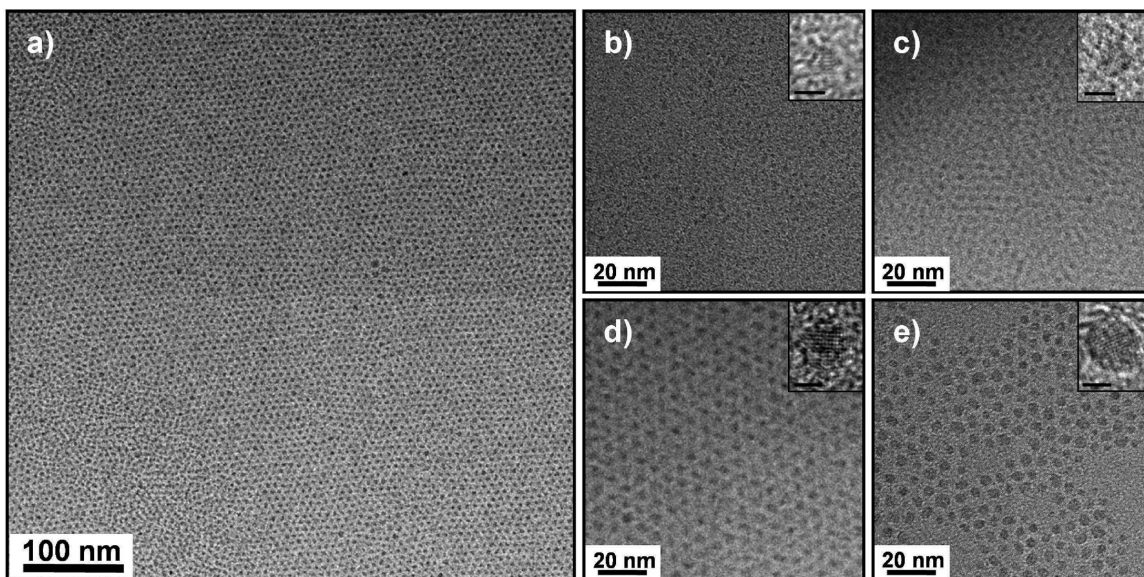
Figure 1.3 TEM images of ESIONs synthesized via thermal decomposition. (a) 3 nm-sized ESPIONs at a magnification of 40K. (b-e) ESIONs of various diameters including (b) 1.5nm, (c) 2.2nm, (d) 3nm, and (e) 3.7 nm at 200K magnification (Kim et al. 2011).

As seen from the work detailed above, thermal decomposition methods offer relatively simple means of achieving both size control and high crystallinity for the synthesis of small nanocrystals. Thermal decomposition is therefore a promising approach to the large-scale manufacturing of small iron oxide MNPS. However, more work needs to be done in the area to ensure that the energy needs required to make large quantities of iron oxide MNPs is economically feasible due to the cost of synthesizing large batches at high temperatures. Future studies are also needed to ensure that the monodispersity and crystalline properties achieved in small-scale production are reproducible at larger scales.

1.3 Principles of Magnetic Resonance Imaging

In recent years, magnetic resonance imaging has become one of the most common medical imaging techniques and a standard of care for the diagnosis of a variety of diseases, with over 32 million scans performed in the United States alone in 2011 (IMV 2012). The reasoning for the increasing prevalence of MR imaging in disease diagnosis lies with its advantages over other medical imaging approaches, such as computerized tomography (CT). MRI scans provide far better soft tissue definition and as such can reveal abnormalities not found in CT scans, making it an excellent cancer diagnosis tool (Shah et al. 2004). In addition, whereas CT exposes patients to potentially harmful ionizing radiation, MRI utilizes magnetic energy and radio frequency to obtain images, limiting patient risk (Parry et al. 2005).

1.3.1 Magnetization and Radiofrequency Pulses

MR imaging is based on the ability to manipulate the magnetic moment and spin of hydrogen atoms found in water and fatty tissue. Spin, or spin quantum number, is a value given to subatomic particles that is proportional to their angular momentum, which is necessary in order for a particle to be subjected to nuclear magnetic resonance (NMR). Hydrogen atoms possess a spin of I=1/2 and 2 measurable energy levels when the nucleus is exposed to an applied magnetic field (Becker 1980). In the absence of an applied magnetic field, the magnetic moments of hydrogen nuclei within a patient are randomly oriented, resulting in a net magnetization of zero. However, when a magnetic field is applied to the patient, such as that within an MRI machine, of field strength B_o, the nuclei align with or against the field, resulting in a non-zero magnetization.

In order to induce an MR signal, a second, rotating magnetic field, B_1, is applied perpendicular to B_o with the same resonance frequency as the hydrogen nuclei' spin. B_1 is produced by a radiofrequency coil and is much weaker than B_o. This transverse field results in a tipping of the net magnetization and what is called the RF flip angle. This angle, α, can be calculated using the following equation:

$$\alpha = \gamma B_1 t_p \tag{1}$$

where γ is the gyromagnetic ratio and t_p is the length of time B_1 is applied. The resulting angular rotation of the net magnetization with respect to B_o produces either positive or negative energy changes within the system. Following this excitation, B_1 is removed and the magnetization returns to its original state via relaxation.

1.3.2 T1 and T2 Relaxation

There are two forms of relaxation that occur after the application of a RF pulse, longitudinal (T1) and transverse (T2) relaxation. T1 relaxation, also known as spin-lattice relaxation, refers to the recovery of the longitudinal magnetization to its original state at thermal equilibrium. T2 relaxation, or spin-spin relaxation, refers to the decay of the transverse magnetization to zero after RF pulse perturbation. This is an intrinsic process that occurs via random spin interactions that result in the loss of phase coherence in the transverse plane. Both types of relaxation time are dependent on the tissue type and can be altered in the presence of large macromolecules.

1.3.3 T1-Weighted and T2-Weighted Contrast

The two forms of relaxation provide the means of producing MR images of tissues. These images are made possible by differences in signal intensities within tissues that result in varying contrast throughout the imaged area. Images can either be T1-weighted or T2-weighted depending on the repetition time (TR) and echo time (TE) that are used. TR refers to the amount of time between RF pulses and consequently the amount of time that the longitudinal magnetization is allowed to recover. Shorter TR values result in T1-weighted images as the longitudinal magnetization is not given much time to recover thus emphasizing differences in T1 relaxation times of tissues. Conversely, if longer TR values are used, the longitudinal magnetization practically reaches its thermal equilibrium state between pulses thereby reducing the signal intensity differences between tissues with different T1 values. TE coincides with the formation of a spin echo, which is described in detail in Figure 1.4. Using a shorter TE minimizes T2

differences, while using a longer TE results in greater signal intensity variation between

tissues with different T2 values (Brant & de Lange 2012). The contrast between tissues

can be further increased by the introduction of contrast agents as detailed below.
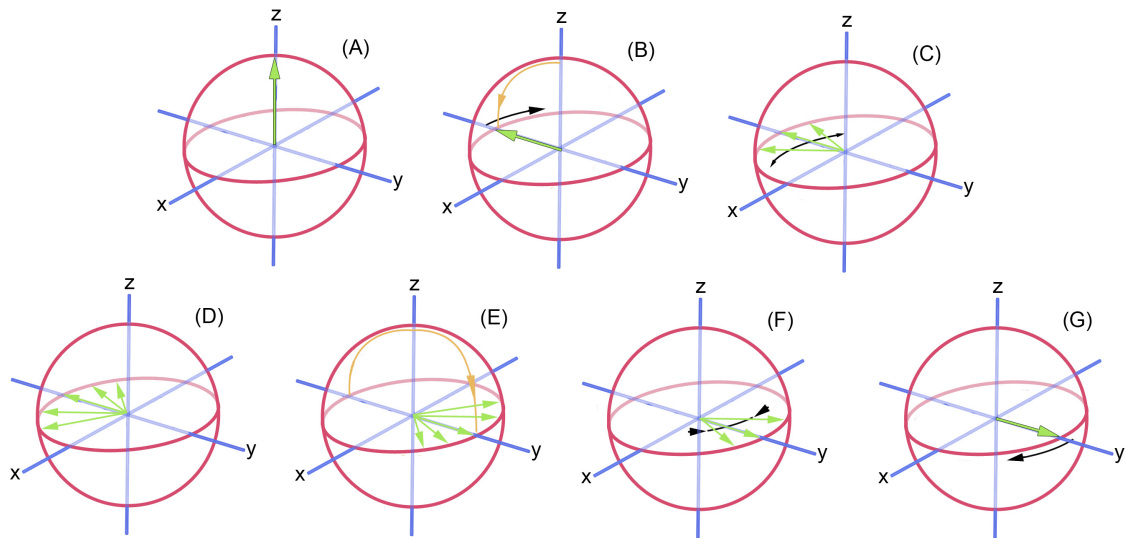
Figure 1.4 Illustration of the spin echo mechanism where the green arrow represents the average magnetic moment. (a) Before the application of the first pulse the average magnetic moment is aligned with the constant magnetic field B_o. (b) A pulse is applied perpendicular to B_o and the average magnetic moment is flipped accordingly. (c-d) As time progresses the net moment begins to precess due to inhomogeneities within the local magnetic fields of the protons resulting in signal decay. (e) A 180° refocusing pulse is applied resulting in the flipping of the magnetic moment and (f) the rephrasing of the transverse magnetization vectors. (g) After some time this refocusing results in the formation of an echo (Filler 2009).

1.4 Iron Oxide Nanoparticles as Diagnostic Tools for Prostate Cancer

Currently, the most studied use of iron oxide nanoparticles is their use as MRI contrast agents. Although non-enhanced MR imaging can provide excellent image quality in some tissues, the development of contrast enhancing agents further the applicability of MR imaging. While iron oxide nanoparticles have been used as diagnostic tools for many different diseases, the following sections will focus on the development and use of iron oxide nanoparticles for the diagnosis and potential treatment of prostate cancer.

1.4.1 IO-MNPs as MRI Contrast Agents

While MRI has been used for cancer diagnosis for many years, there have been limitations to its use in the diagnosis and monitoring of prostate cancer. These limitations included a restricted ability to achieve capsular penetration, an inability to distinguish tumors from other sources of signal reduction, and a lack of information regarding tumor grade and vascularity (Padhani, A. 2000). In 1996, Jager et al. published their work in which the ability of using endorectal MR imaging for the local staging of prostate cancer was studied. The study population consisted of 34 male patients in which the presence of prostate cancer had been previously confirmed via biopsy. In this study a T1 contrast agent known as gadopentetate dimeglumine, or Magnevist®, was used. It was found that MR imaging correctly depicted the location of 67% of prostatic tumors. In addition, 20% of the lesions that were seen in the images appeared to be false-positive cases. All of the tumors unable to be detected by MR imaging were located centrally and ventrally within the prostate. The accuracy of tumor volume prediction using MR imaging was also tested and in only 10 cases tumor volume was shown to be within 25% of the actual volume. In

16 cases the tumor volume was overestimated by more than 25% and was underestimated in the remaining 8 cases (Jager et al. 1996). Clearly, the results in the study indicated that improvements to MRI were needed to allow for accurate diagnosis and monitoring of cancer in the prostate. A few years later, Padhani et al. set out to improve upon Jager et al.'s attempt to correlate MR images of prostate cancer and histological analysis. Magnevist® was also used in this study to obtain MR images in 48 patients with confirmed prostate cancer. As can be seen in Fig. 1.5, the quality of images obtained via MRI greatly improved over the few years between the work of Jager and Padhani due to advances in techniques and instrumentation. The images that were obtained allowed reviewers to identify tumors in 45 of the patients, a marked improvement over the previous work. However, despite the improved image quality leading to more accurate identification of tumors, no histological correlation was able to be obtained in this study. It was concluded that enhancement characteristics do not directly correlate with properties such as tumor stage, tumor grade, or serum PSA levels (Padhani, A. 2000). However, the biggest problem with this study is its use of T1 contrast agents to image the prostate tumors. With the introduction of iron oxide MNP contrast agents and their T2 relaxation properties, the amount of information that was able to be obtained via MR imaging greatly increased.
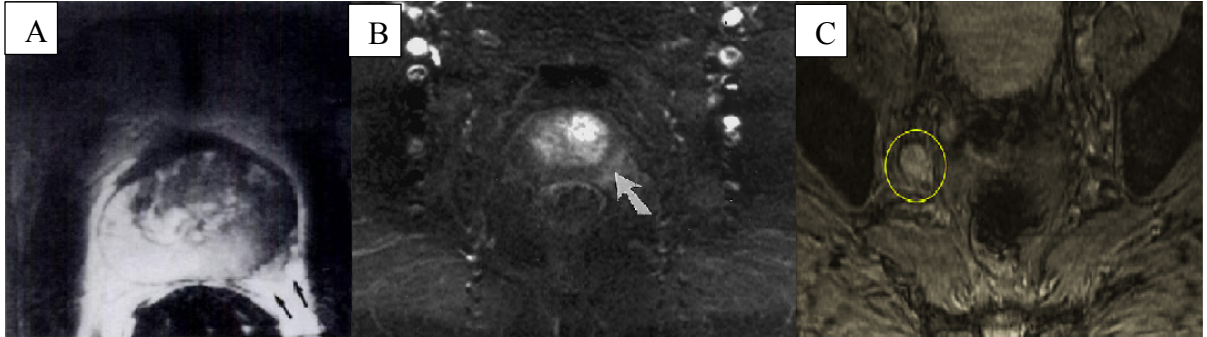
Figure 1.5 The development of MR imaging of the prostate for prostatic cancer diagnosis. (A) Image of tumor from Jager et al. study. (B) Image of tumor from Padhani et al. study. (C) Image of the metastasis of prostate cancer in the prostatic lymph nodes using iron oxide nanoparticles (Jager et al. 1996, Padhani 2000, & Dassai et al. 2009).

1.4.2 IO-MNPs as Contrast Agents for Hybrid Imaging Approaches

Despite the progress that has been made in both MRI technology and contrast agents, the acceptance of MR imaging for prostate cancer detection and treatment planning is still not universal due to limitations that are still present in translating MR images into quantitative information (i.e. aggressiveness). As a result, there has been growing interest in the development of a hybrid imaging technology that combines MR imaging with positron emission tomography (PET). PET is a well-established imaging technique that displays tracer distributions within the body that are dependent on the level of biological activity within cells. This can be very advantageous for analyzing cancer as tumor cells are known to possess increased glycolytic rates when compared to normal cells. These areas of cells can then be seen as areas of high activity in PET images as seen in Fig. 1.6. The main reason for the growing interest in simultaneous PET/MR imaging is the idea that it would provide superior spatial registration of both the molecular PET and anatomical MRI, thus providing qualitative and quantitative data regarding the disease. The combination of image modalities is also beneficial in that it can minimize patient motion and the resulting tissue deformation that is often seen when the two types of images are taken separately. This can result in issues and errors when trying to derive information from the two sets of images (Lee et al. 2008). With the development of new imaging technologies comes the need for new contrast agents and iron oxide MNPs are being looked to as the best candidates for these types of applications.
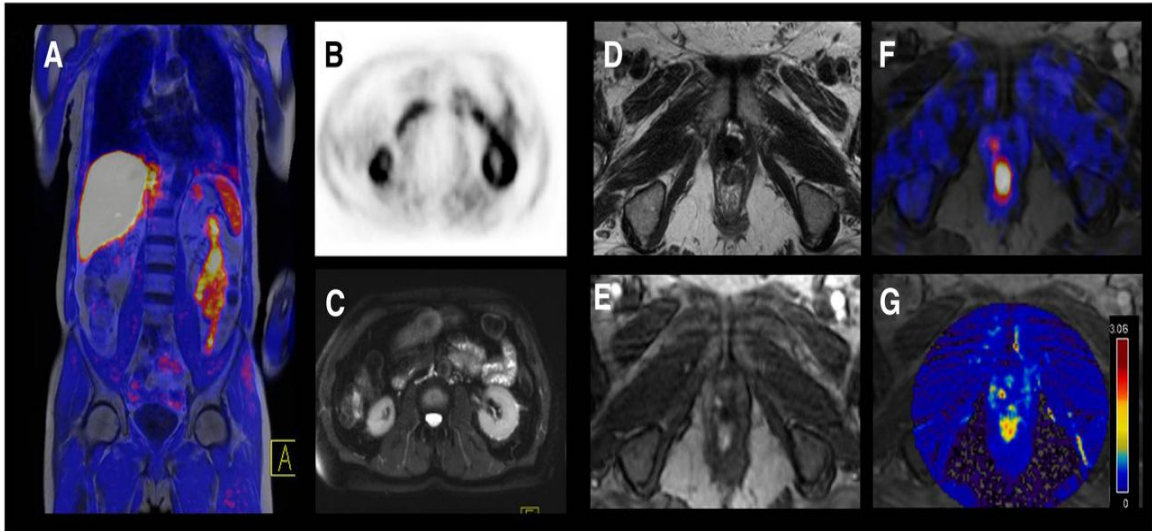
Figure 1.6 Example of combined PET/MR imaging of the prostate (A, F-G) (Martinez

Moller et al. 2012).

Recently, Lee *et al.* reported the development of RGD-conjugated radiolabeled iron oxide nanoparticles to be used as PET/MRI agent for tumor imaging. The iron oxide particles were coated with polyaspartic acid (PASP) and functionalized with the radionucleotide ^{64}Cu as a PET imaging agent. The iron oxide MNPs were also functionalized with targeting ligands for increased accumulation in tumor tissue via recognition by integrin $\alpha_v\beta_3$. Using a mouse model, the dual imaging capabilities of these contrast agents were tested and proven (Lee et al. 2008). While more testing is required and further development of PET/MRI technologies is needed, the value of this work is extremely high as not only were they able to develop iron oxide MNPs with both PET and MR imaging capabilities but the synthesis method used is very simple and holds great potential for scale-up.

1.5 Iron Oxide Nanoparticles as Therapeutic Tools for Prostate Cancer

While IO-MNPs are most often associated with imaging applications, research has also been done using iron oxide nanoparticles as therapeutic agents as well. The discussion herein of IO-MNPs used as prostate cancer therapies will focus on thermotherapy and drug carrier applications.

1.5.1 Thermotherapy

One of the most common applications of magnetic nanoparticles in the treatment of cancer is the ability to use them in thermotherapy. Thermotherapy is defined by the localized heating of tumor tissue via an alternating externally applied magnetic field applied to injected magnetic nanoparticles. This increase in temperature is known to

cause cell death within the tumor. In the first clinical trial of its kind, the use of IO-MNPs as thermotherapy agents for the treatment of locally recurrent prostate cancer was conducted Johannsen *et al.* in 2006. In this study, 10 patients who had confirmed local recurrence of prostate cancer were subjected to thermal treatment in order to determine the feasibility of thermotherapy and its analysis as a potential standard therapy for local recurrence. The IO-MNPs in this study had an average core size of 15nm and were coated with an aminosilane-typeshell. Patients were injected with an amount of the IO-MNP solution and the first thermotherapy session was performed 1-2 hours post-injection. The magnetic field was increased to a point that could be tolerated without causing discomfort to the patient and was sustained for 1 hour. During this time, the temperature at the site of the nanoparticles rose to 45°C-49°C. It is known that temperatures >45°C cause direct cell death and therefore care must be taken to ensure that the increase in temperature is restricted to the tumor site. From the results of this study it was found that thermotherapy of the prostate was indeed feasible as thermoablative temperatures were achieved at relatively low magnetic field strengths, causing little to no discomfort in the patients (Johannsen et al. 2007). While their results are promising, work is still needed in ensuring a homogeneous distribution of the nanoparticles throughout the prostate.

1.5.2 Targeted Drug Delivery

IO-MNPs are very good platforms for targeted drug delivery due to their superparamagnetic properties and their large surface-to-volume ratio that enables functionalization with various targeting moieties. IO-MNPs can therefore be targeted to a specific site by the influence of an external magnetic field and/or by targeting cell surface

receptors or some other marker specific to the target cell or tissue. Several potential diagnostic markers have been identified that are specific to prostate cancer which could potentially be targeted for drug delivery purposes. DD3 transcripts and cysteine-rich secretory protein-3 (CRISP-3) are examples of known diagnostic markers that could be potentially targeted for drug delivery. DD3 have been shown to be abundant in primary prostate tumors and metastases. Interestingly, it is not found in benign prostate hyperplasia or normal prostatic tissue making it a good determinant of the type of prostate cancer present. CRISP-3 has been identified as one of the most up-regulated genes in prostate tumors. In one study a 21-fold overexpression of CRISP-3 was found in prostate cancer tissue when compared to the adjacent tissue (Meyer et al. 2004). Prostate specific membrane antigen (PSMA), a transmembrane glycoprotein, is one of the most studied targets for prostate cancer therapies. PSMA is typically targeted via the addition of aptamers or folate ligands to the surface of nanoparticles as seen in Figure 1.7 (Byrne et al. 2008).
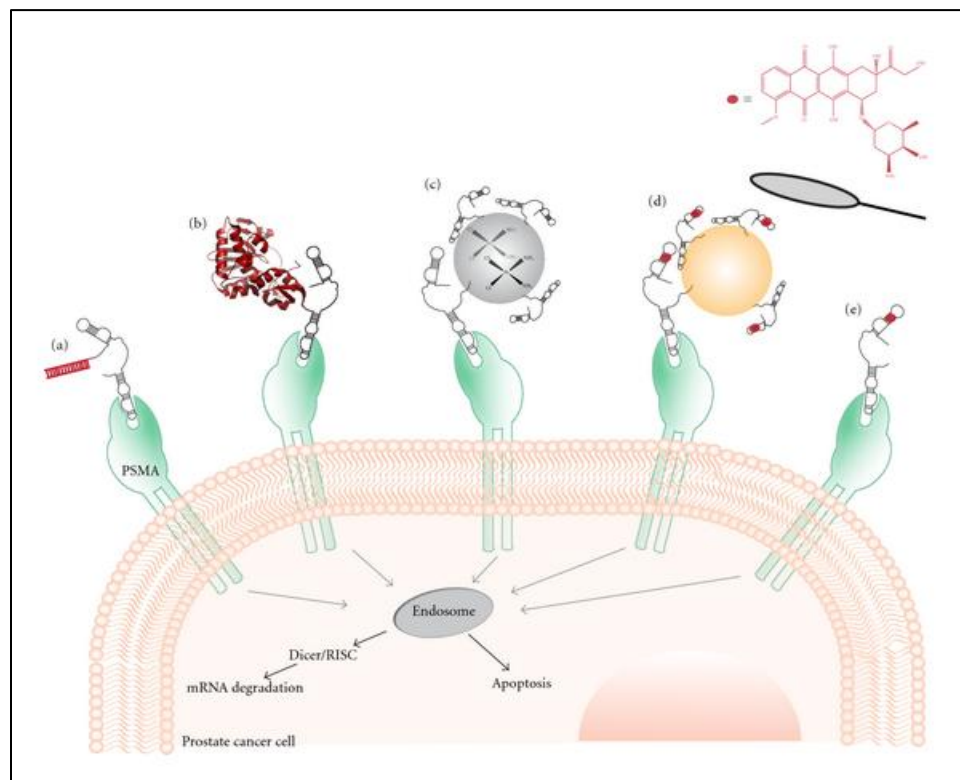
Figure 1.7 Targeting PSMA using aptamers conjugated to (a) siRNAs, (b) cytotoxic molecules, (c) organic nanoparticles, (d) inorganic nanoparticles and quantum dots, and (e) drugs such as doxorubicin. (Meyer et al. 2011).

Aptamers are RNA or DNA oligonucleotides that are able to bind to specific target molecules, which in this case is PSMA. The benefits of using aptamers as a targeting method include their small size and lack of immunogenicity. Farokhzad first reported the use of nanoparticle-aptamer bioconjugates in 2004. In this study, rhodamine-labeled dextran was used as a model drug and was loaded onto nanoparticles for proof-of-concept studies. Nanoparticles were functionalized with RNA aptamers that are known to target PSMA to achieve targeted drug delivery. The level of cellular uptake and binding was then studied *in vitro* using prostate LNCaP and PC3 cell lines. It was found that there was a 77-fold binding enhancement and modest enhancement of PSMA endocytosis versus the control group (Farokhzad, O.C. 2004). These results lend credit to the emerging support for the use of PSMA specific aptamers as a means of targeting nanoparticle drug systems to prostate cancer sites. New potential targeting sites are continually being discovered and it will be the responsibilities of researchers to determine the most effective targets whose corresponding functionalities can be easily applied to the surface of IO-MNPs.

1.6 Size Effect on the *in vivo* Biodistribution and Pharmacokinetics of IO-MNPs

The effectiveness of nanomaterial systems for *in vivo* applications is largely determined by their biodistribution and pharmacokinetics. This is because in order to be effective, the nanomaterials must be able to overcome various biological barriers in order to reach their target while avoiding clearance from circulation (Kettiger et al. 2013). As a result, there has been a growing interest in determining how the physical and chemical properties of nanoparticles affect their uptake and distribution *in vivo* (Dobrovolskaia et

al. 2008; Thorek and Tsourkas 2008; Win and Feng 2004). The fate of nanoparticles is principally determined by properties such as surface chemistry, charge, and size. While work has been done in determining the effect of surface chemistry and particle charge, the discussion here will focus on the effect of size on nanoparticle behavior *in vivo.*

While nanoparticle size is understood to have an effect on the biodistribution and pharmacokinetics, our understanding is fairly rudimentary. It is generally accepted that nanoparticles in the size range of 10-200 nm are best suited for *in vivo* applications for reasons explained further below (Gupta & Gupta 2004; Laurent et al. 2008; Xie et. al 2009). However, this large size range is based on a myriad of proof-of-concept studies as opposed to fundamental investigations leading to discrepancies in reports of size optimization of nanomaterials (Albanese et al. 2012). If nanomaterials are to reach their full potential as diagnostic and therapeutic tools, precisely controlled experiments must be conducted to adequately evaluate the impact of size and other properties on *in vivo* behavior.

1.6.1 Effect of Size on Clearance of Nanoparticles

The body has many different methods of clearing foreign materials, such as IO-MNPs, from the blood and this clearance has been shown to be highly dependent on size. One of the most common forms of clearance that nanoparticles must overcome to achieve long-circulation, especially in the case of intravenous injection, is the mononuclear phagocyte system (MPS). The MPS refers to a component of the immune system that is composed of various types of phagocytic cells, including macrophages, and is responsible for clearing and degrading foreign materials that may enter the bloodstream (Moghimi et

al. 2001). The uptake of nanoparticles by the MPS can prevent them from reaching their target and may possibly lead to adverse effects such as inflammation (Naqvi et al. 2010). Previously, it has been shown that the size of nanomaterials affects macrophage uptake (Clift et al. 2008; Walkey et al. 2011). In most cases, particles greater than 500 nm in size can be expected to be taken up via phagocytosis by macrophages (Hillaireau & Couvreur 2009). However, particles smaller than 500 nm have been shown to be taken by the MPS as well (Krpetić et al. 2011). This discrepancy can be explained by the role that proteins, known as opsonins, play in phagocytic uptake.

Once introduced into physiological environments, nanomaterials are exposed to a variety of serum proteins that quickly adsorb onto their surface which can lead to alterations of the physical and chemical properties of the nanomaterial. These surfaced adsorbed proteins become what is known as the "protein corona" (Walkey & Chan 2012). The corona is composed of a number of different proteins, including opsonins, which enhance macrophage uptake, and proteins that may induce enzymatic cascades leading to thrombosis or anaphylaxis. (Moghimi et al. 2010; Patel, H.M. 1992). For this reason, most nanomaterials intended for biological applications are coated with some material, such as polyethylene glycol (PEG), which reduces protein adsorption by interfering with protein binding sites (Jeon et al. 1991).

1.6.2 Effect of Size on Biodistribution

With the need for nanomaterial therapies to reach their desired site of action, there has been great interest in determining how to optimize the biodistribution of administered nanoparticles. The biodistribution is determined by a number of factors, including the

properties of the nanomaterial, anatomical barriers, and disease state (Moghimi et al. 2005). With respect to size, nanoparticles less than 6 nm are filtered out by the kidneys and those larger than 200 nm tend to accumulate in the liver and spleen (Choi et al. 2007; Moghimi 1991). While the effect of size on the biodistribution has been extensively characterized for some nanomaterials (i.e. gold and polymeric nanoparticles), data regarding the biodistribution of differently sized iron oxide nanoparticles is very limited (Chouly et al. 1996).

1.6.3 Effect of Size on Tumor Accumulation

Given that tumors possess leaky vasculature and altered lymphatic drainage, cancer provides abnormal morphology and transport conditions that can be exploited to achieve increased accumulation of nanoparticles within tumors. This altered physiology lends itself to what is known as the enhanced permeability and retention (EPR) effect as illustrated in Figure 1.8 (Maeda et al. 2000). The leaky vasculature is a result of the increased rate of angiogenesis found within the tumor microenvironment. These gaps between endothelial cells form pores that allow for easier extravasation into the tumor tissue. The pore cutoff size has been found to generally be approximately 400 nm, however it is generally accepted that nanoparticles >200 nm are most effective (Yuan et al. 1995). Coupled with the defective lymphatic drainage, the EPR effect permits nanoparticles to enter and remain within the tumor microenvironment. However, studies have shown that if nanoparticles are too small (i.e. <20 nm), they may experience decreased accumulation due to increased permeation through the tumor and into

surrounding tissues (Perrault et al. 2009). Therefore, in order to achieve maximum tumor

accumulation via passive targeting, size optimization of nanoparticles is needed.
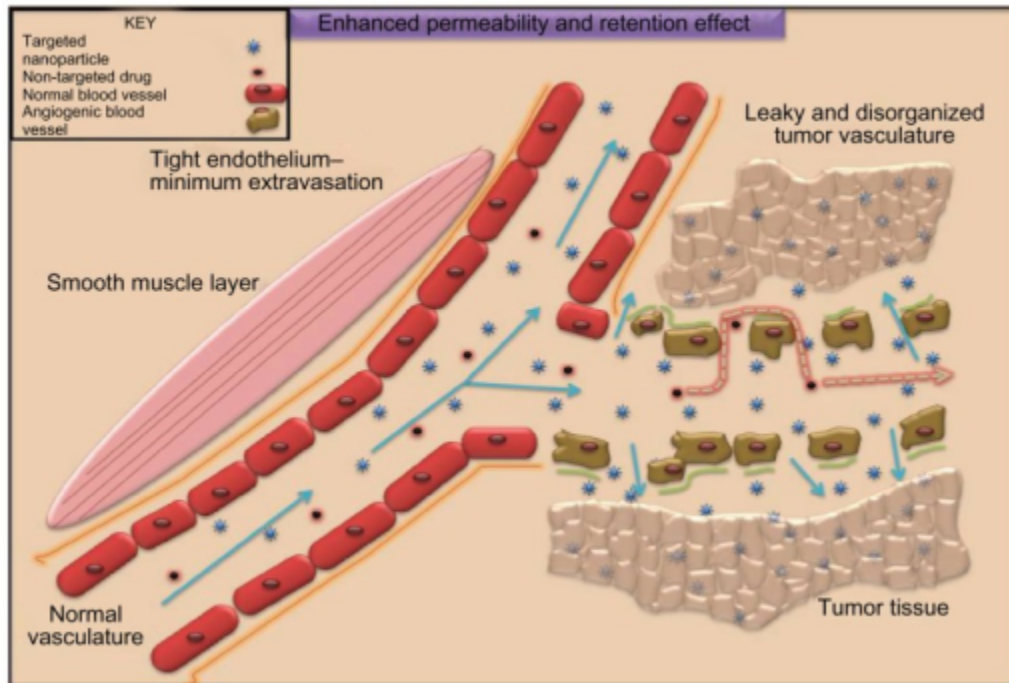
Figure 1.8 Illustration of the enhanced permeability and retention effect, including that leaky vasculature characteristic of tumor tissue that allows for passive targeting of therapies (Ranganathan et al. 2012).

1.7 Size-selective Fractionation of Magnetic Nanoparticles

It is overwhelmingly clear that size optimization of nanomaterials meant for any biomedical application is necessary. However, in the case of IO-MNPs this task is much harder to accomplish than other types of nanomaterials (i.e. starch or gold) whose size can easily be controlled during synthesis to achieve distinct size distributions. While very small IO-MNPs (<10 nm) can be synthesized in a highly size-controlled manner, these nanoparticles are too small for biomedical applications. The synthesis of IO-MNPs in the desired size range of 20-200 nm requires synthesis methods that result in a highly polydisperse final product (Gupta & Gupta 2004). Therefore, an effective post-synthesis size-selective fractionation method is needed to optimize IO-MNPs for different applications.

One potential approach to this problem is the use of magnetic field-flow fractionation (FFF). Magnetic FFF was first reported in 1980 by Vickrey and Garcia-Ramirez in which they wrapped Teflon tubing around a small electromagnet in an attempt to separate magnetic materials from a fluid. FFF is based on the separation of materials via the combined effects of the force from a mobile phase within a channel and an additional force perpendicular to flow. In the case of magnetic FFF the perpendicular force is derived from an externally applied magnetic field. An illustration of the underlying mechanisms of magnetic FFF can be found in Figure 1.9. Magnetic FFF is largely based on the exploitation of size-dependent hydrodynamic and magnetic forces. The drag force experienced by a nanoparticle in laminar flow is determined by the equation:

$$F_{\mathrm{D}} = 6\pi\eta R v \tag{2}$$

where F_D is the drag force in Newtons, η is the solvent viscosity, R is the hydrodynamic radius of the nanoparticle, and v is the velocity of the mobile phase. The magnetic force exerted on a nanoparticle by an applied magnetic field is described by the equation:

$$F_{mag} = \frac{V_p \Delta\chi (\nabla B^2)}{\mu_o}$$

(3)

where F_{mag} is the magnetic force, V_p is the nanoparticle volume, $\Delta\chi$ is difference in magnetic susceptibility between the nanoparticle and the media, B is the induced magnetic field, and μ_o is the free space permeability (Pankhurst et al. 2003). As can be seen from these two equations, both forces are dependent on the size of the nanoparticle thus allowing them to be used to manipulate magnetic nanoparticles in a size-dependent manner.

Typically, a magnetic FFF setup includes a single piece of tubing that is either wrapped around a permanent magnet or is surrounded by an electromagnet. The magnetic nanoparticle solution is injected into the tubing until the volume of the tubing is filled. The nanoparticle solution is then allowed to remain stationary for some time in order to allow the nanoparticles to reach a steady state distribution at the accumulation wall. Size-dependent elution of nanoparticles is then achieved by introducing the mobile phase and either varying the flow rate or the strength of the magnetic field.
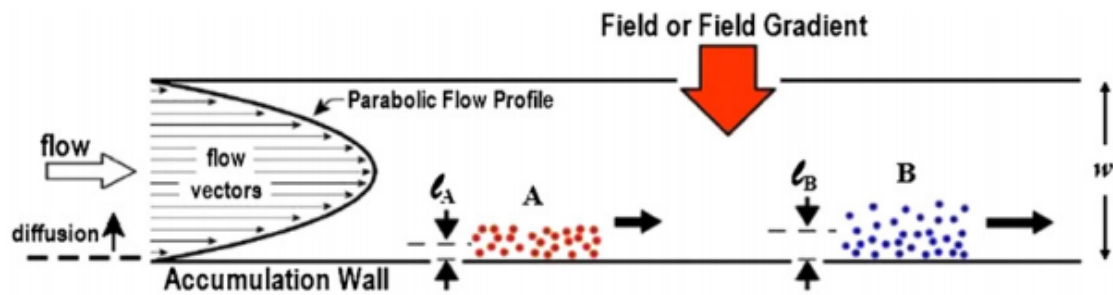
Figure 1.9 Illustration of magnetic field-flow fractionation mechanism. Zone A represents the initial accumulation of magnetic particle due to interaction with the magnetic field gradient. Zone B illustrates the removal of a fraction of the accumulated particles due to the introduction of the mobile phase (Carpino et al. 2007).

While there has been interest in the area of magnetic FFF for many years now, most of the work that has been done has focused on using it as a means of characterizing very small volumes of nanoparticles, such as estimating their magnetic moments, or separating magnetic from non-magnetic nanoparticles (Carpino et al. 2005; Latham et al. 2005). Very few have suggested its potential use as a means of improving the polydispersity of magnetic nanoparticle solutions, and even fewer have attempted its use for this purpose. So far, only one group has focused on the use of magnetic FFF for size separation using a technique known as differential magnetic catch and release (DMCR) to separate nanoparticles with sizes less than 20 nm (Beveridge et al. 2009). Additionally, hexane is used as the mobile phase making an additional phase-transfer step necessary in order for the separated nanoparticles to be used for biomedical applications. Therefore, the development of similar methods that utilize an aqueous mobile phase, can achieve size-selective separation of magnetic nanoparticles within the size range desired for *in vivo* use, and are able to produce larger volumes of separated size distributions would be advantageous for the optimization of nano-sized therapeutics.
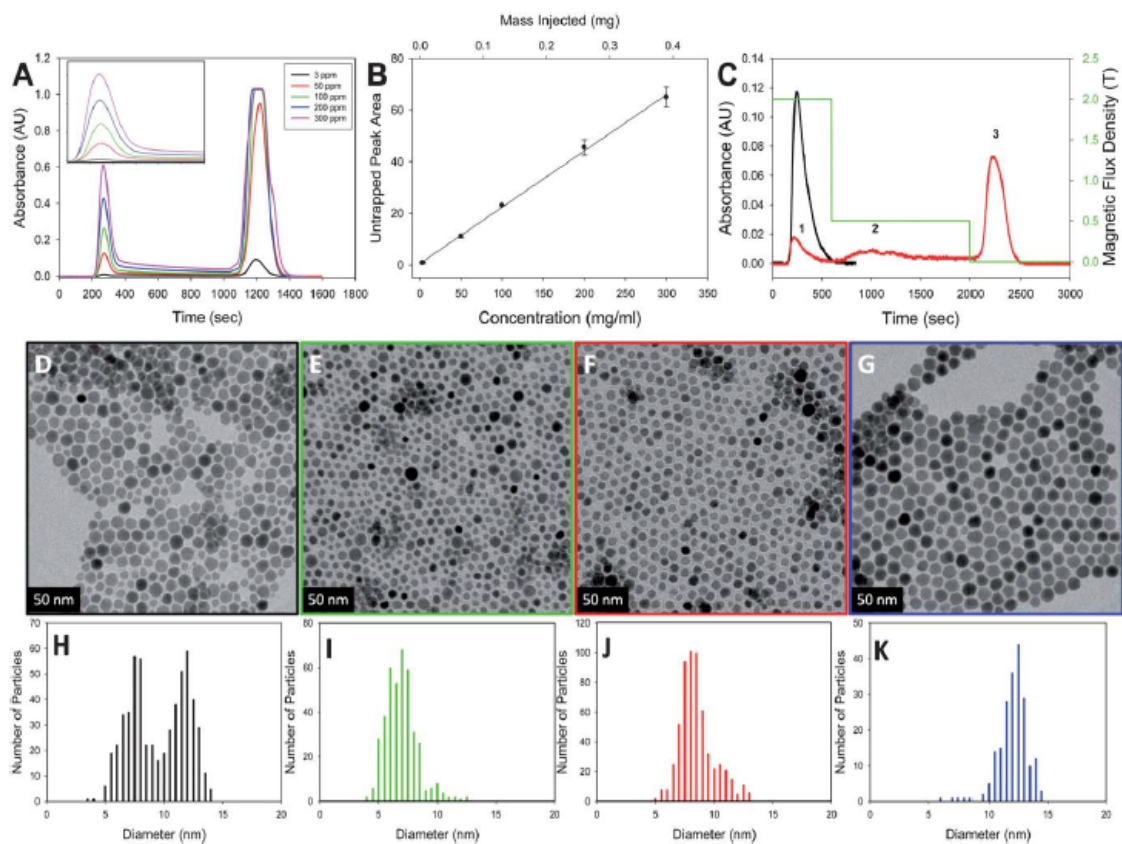
Figure 1.10 Size separations of CoFe$_2$O$_4$ nanoparticles in hexane achieved using DMCR of average sizes (D) 9.3 ± 2.4, (E) 6.7 ± 1.4, (F) 8.3 ± 1.5, and (G) 11.8 ± 1.3 nm. (Beveridge et al. 2011).

Chapter 2

The Identification of an Effective Size-selective Separation Method for Magnetic

Nanoparticles

2.1 Introduction

Magnetic nanoparticles, specifically those composed of iron oxide, are used in a variety of applications, especially in the area of drug delivery and biomedical imaging. However, the inability to synthesize MNPs larger than ~20 nm in a monodisperse manner has greatly limited their optimization for biomedical applications as resulting broad size distributions and batch-to-batch variability leads to unpredictable behavior when used clinically. This is because the *in vivo* biodistribution and pharmacokinetics are size-dependent properties. Therefore, the lack of size control with current synthesis methods results in questions regarding safety and prevents the clinical translation of many promising nanomedicines. In order to ensure the success of current and future nanomedicines, methods must be developed that either allow for size-monodisperse synthesis of iron oxide nanoparticles or enable the size-selective fractionation of magnetic nanoparticles post-synthesis.

The size of nanomaterials can have a significant effect on their fate once introduced into the body. For example, upon entering the bloodstream the size of a nanomaterial can affect how it interacts with other components present in the

bloodstream, such as macrophages. It has previously been shown that nanoparticles larger than 500 nm are typically taken up by macrophages via phagocytosis (Hillaireau & Couvreur 2009). Additionally, the body has a number of anatomical barriers in place to remove foreign materials. The kidneys are able to filter out nanomaterials smaller than 6 nm and nanomaterials larger than 200 nm are often found to accumulate within the liver and spleen (Choi et al. 2007; Moghimi 1991). Disease state can also affect the biodistribution and pharmacokinetics of nanomaterials as well. In the case of cancer, tumors typically possess a heterogeneous morphology that includes leaky vasculature and altered lymphatic drainage which results in what is known as the enhanced permeability and retention (EPR) effect. The presence of the leaky vasculature enables easier extravasation of nanomaterials into the tumor microenvironment. However, it has been shown that there is a pore cutoff size of approximately 400 nm in regards to the gaps present between endothelial cells, with particles of size <200 nm typically being most effective (Yuan et al. 1995). It is then clear that methods that allow for the optimization of nanomaterial size will be needed in order for the potential of iron oxide nanoparticles to be fully realized. A promising solution to this problem is the use of magnetic field-flow fractionation as a means to separate polydisperse distributions of magnetic nanoparticles into monodisperse fractions. This process is based on the separation of materials via the combined effects of the size-dependent drag force from a mobile phase within a channel and an additional size-dependent magnetic force perpendicular to the flow. This chapter details the investigation of magnetic separation as a feasible means of size-selectively separating magnetic nanoparticles.

2.2 Experimental

2.2.1 Materials

fluidMAG-D (starch-coated magnetite (Fe_3O_4)) iron oxide nanoparticles (75mg/mL) were obtained from Chemicell® GmBH (Berlin, Germany). Succinimidyl polyethylene glycol (mPEG-NHS) of molecular weight 5 kDa was obtained from Nanocs (New York, NY). Dimethyl sulfoxide (($CH_3)_2SO$, 99.9%) was obtained from BDH Chemicals. Epichlorohydrin (C_3H_5ClO, 99%) was obtained from Alfa Aesar. Sodium hydroxide (NaOH, 97%) was obtained from BDH chemicals. Ferrozine iron reagent, monohydrate was obtained from J.T. Baker. Neocuproine hydrochloride monohydrate ($C_{14}H_{12}N_2 \cdot HCl \cdot H_2O$, 99%) was obtained from Acros. Ammonium acetate, ACS (CH_3COONH_4, 97% min) was obtained from Alfa Aesar. L-ascorbic acid ($C_6H_8O_6$) was obtained from BDH. Iron standard solution (1.00 mg/L as Fe) was obtained from HACH. Deionized water (DI-H_2O) was obtained using an ELGA PURELAB Flex water purification system.

2.2.2 Surface Modification of Iron Oxide Nanoparticles

The IO-MNPs were cross-linked, aminated, and PEGylated according to previously established methodology as shown in Figure 2.1 (Cole et al. 2010). First, 2 mL of MNP suspension (42 mg/mL) was incubated with 2.6 mL 6M NaOH for 15 minutes. 1.3 mL of epichlorohydrin was then added and the mixture was incubated for 24 hours at 25°C with shaking. After incubation, the solution was thoroughly dialyzed against DI-H_2O using a 8-10 kDa MWCO Float-A-Lyzer® G2 dialysis device (Spectrum Laboratories, Inc., Rancho Dominguez, CA). The purified product was then incubated

with 2 mL of concentrated NH₄OH (30% ammonia) for a period of 24 hours at 25°C with shaking. The aminated-MNP suspension was then sufficiently dialyzed against DI-H₂O and the final product was concentrated using a Sphero™ Fleximag Separator (Spherotech, Lake Forest, IL).

The PEGylation of the MNPs was achieved by utilizing NHS chemistry. First, 15mg of mPEG-NHS was dissolved in a mixture of 320 µL of DMSO, 320 µL of DI-H₂O, and 320 µL of pH 8 phosphate buffer. 320 µL of aminated-MNP solution was then added and the mixture was incubated at 25°C with shaking. At the completion of incubation, the solution was diluted to ~7mL with DI-H₂O, placed on the magnetic separator, and then subjected to several washes with fresh DI-H₂O. After washing, the PEG-MNP solution was diluted to the final desired concentration.
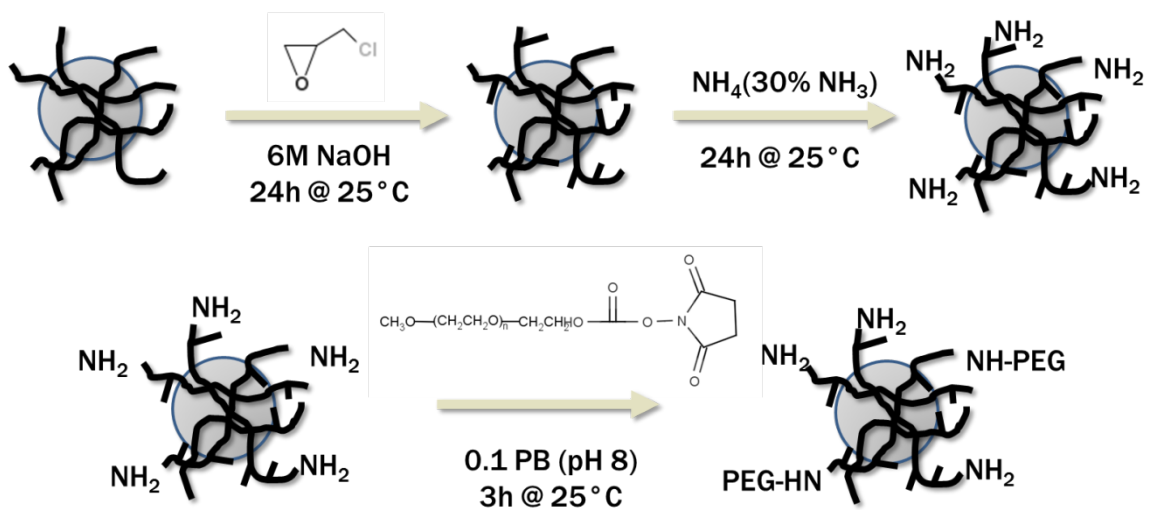
Figure 2.1 Reaction scheme used for the surface modification of iron oxide nanoparticles with polyethylene glycol (PEG).

2.2.3 Characterization of MNPs

Dynamic Light Scattering (DLS) – Dynamic light scattering was used to measure the intensity-weighted size (hydrodynamic diameter) distribution. Measurements were taken in triplicate using a ZetaSizer Nano ZS90 sizing instrument (Malvern, Worcestshire, UK).

Transmission Electron Microscopy (TEM) – A Zeiss EM 10 TEM operating at a voltage of 60K was used to determine size distributions of MNPs. TEM samples were prepared by placing a single drop of a MNP solution onto a carbon type B, 300 mesh grid. The grid was then placed in a petri dish and allowed to dry at ambient conditions. Size distributions were obtained using ImageJ software to size a sufficient number of MNPs from multiple TEM images taken of each sample.

Iron Content Assay – The iron content of MNP solutions was determined using a ferrozine assay. Briefly, a 200 μL dilution (typically 1:1000) of the MNP sample was obtained in combination with 1M HCl. 230 μL of $KMnO_4$/HCl was added to the sample and mixed via pipette. The $KMnO_4$/HCl solution was made by mixing equal volumes of 4.5% w/v $KMnO_4$ with 1.4M HCl. The mixture was then incubated for 2 hours at 60°C followed by a 10 minute cooling period. The sample was then mixed and transferred to a well plate via two 180 μL aliquots. 30 μL of prepared ferrozine solution was then added to the samples, mixed, and incubated at ambient conditions for 30 minutes. The prepared ferrozine solution was composed of 6.5mM ferrozine, 6.5mM neocuprine, 2.5M ammonium acetate, and 1M ascorbic acid dissolved in DI-H_2O. The absorbance of the samples at 550nm was then measured using a SpectraMax i3 plate reader (Molecular Devices, Sunnyvale, CA). Standard curves were created using an iron standard solution.

2.2.4 Modeling MNPs in Fluid Flow Through Magnetic Field

A MATLAB script was created to model and predict the size-dependent behavior of MNPs subjected to fluid flow through a magnetic field gradient.

Particle Forces

The behavior of MNPs introduced to flow through a constant magnetic field is determined by the system of forces, most of which are size-dependent, experienced by the individual particles. For this model the drag force, magnetic force, and random force in Brownian motion were all considered. Particle-particle interactions were considered to be negligible.

Drag Force

In fluid dynamics, the drag force refers to the resistive force acting on an object opposite the direction of the flow velocity. For the case of small spherical particles in a fluid possessing a small Reynolds number, the drag force F_D can be described using Stokes drag, which is defined as:

$$F_D = -6\pi\eta r v \tag{4}$$

where η is the fluid viscosity, r is the hydrodynamic radius of the particle, and v is the velocity (Bird 1963). The drag force is therefore directly proportional to the size of the particle.

Magnetic Force

The magnetic force $\vec{F}_M$ experienced by a magnetic particle within an applied magnetic field $\vec{B}$ is given by the following equation:

$$\vec{F}_M = (\vec{m} \cdot \nabla)\vec{B} \tag{5}$$

where $\vec{m}$ is the magnetic moment of the magnetic particle. The magnetic moment of a particle can be calculated using the equation:

$$\vec{m} = \rho V \vec{M} \tag{6}$$

where ρ is the density of the particle, V is the volume of magnetic material in the particle, and $\vec{M}$ is the magnetization of the particle (Shevkoplyas et al. 2007). According to equation 6, the magnetic force experienced by a particle is proportional to $\sim r^3$ and therefore as particle size increase, the experienced magnetic force increases proportionally.

Brownian Motion

For very small particles in a fluid, collisions with molecules result in a source of diffusion known as Brownian motion. The diffusion length L_D traversed by a particle in two-dimensions over some time interval t is determined by the equation:

$$L_D = \sqrt{4Dt} \tag{7}$$

where D is the particle-specific diffusion coefficient, which is defined as:

$$D = \frac{k_B T}{6\pi\eta r} \tag{8}$$

where k_B is the Boltzmann's constant and T is the absolute temperature (Berg 1993). From this relation it can be seen that diffusion due to Brownian motion is size-dependent and the rate of diffusion increases as particle size r decreases.

Prediction of Particle Trajectories

The movement of particles within the modeled system was predicted by using a summation of the forces acting on a single particle at some coordinate $(x_{MNP}(t), y_{MNP}(t))$ to determine the particle's new x $(x_{MNP}(t+1))$ and y $(x_{MNP}(t+$

1)) position after a time-step dt. The new position of the particle was determined using the following equations:

$$x_{MNP}(t + 1) = x_{MNP}(t) + D_{Bx} + \left[\frac{v_x(t)+v_x(t+1)}{2}\right] dt \qquad (9)$$

$$y_{MNP}(t + 1) = y_{MNP}(t) + D_{By} + \left[\frac{v_y(t)+v_y(t+1)}{2}\right] dt \qquad (10)$$

where D_{Bx} and D_{By} refer to the diffusion length in the x and y-direction, respectively, and v_x and v_y are the respective velocities in the x and y–directions. The diffusion length in each direction was calculated for each time-step by assigning a random percentage of the size-dependent diffusion length L_D calculated using equation 7 for each particle for time-step dt to the x-direction and the balance percentage to the y-direction. This was done to mimic the random-walk phenomenon that occurs as a result of Brownian motion.

A two-dimensional channel with a length of 60mm and a diameter of 1.6mm was used to simulate a proposed experimental design of using similarly sized tubing run across a series of 5 ¼"x¼" cylindrical neodymium magnets. Particles were introduced into the mobile phase at a randomly generated distance from the wall opposite the magnets no greater than 100µm and the predicted path was calculated for each particle individually. The size of particles to be run in the simulation were taken from size distribution data obtained using DLS. Approximately 100 particles were run in each simulation with the frequency of each size reflective of the frequency observed in the intensity-based size distribution such as that shown in Figure 2.3. A y-split connector was assumed to be used with this system and therefore the separation of particles was determined by their y-position at the end of the channel (x = 60mm). If the final y-position of a particle was greater than zero (center of the channel is at y = 0) then it was

44

considered to be in Fraction 1. However, if the final y-position was equal to or less than zero, the particle was considered to be in Fraction 2.
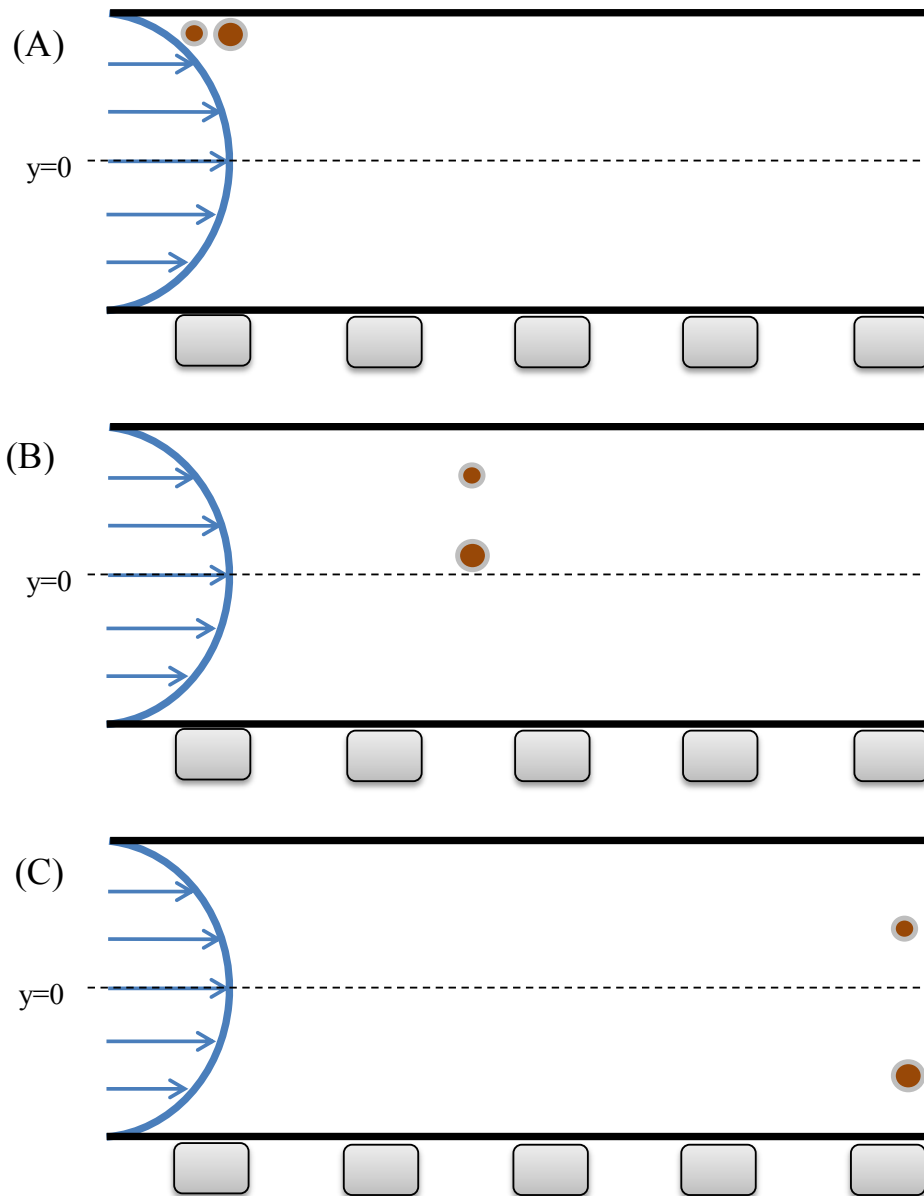
Figure 2.2 Illustration of the proposed mechanism for size-selective separation. (A) Magnetic nanoparticles are introduced into flow at the wall opposite the source of the magnetic field gradient. (B) As the particles flow through the magnetic field they begin to separate according to their size across the channel width. (C) At the end of the channel the particles have reached some size-dependent distribution across the channel and can now be separated into Fraction 1 ($y > 0$) and Fraction 2 ($y \leq 0$).
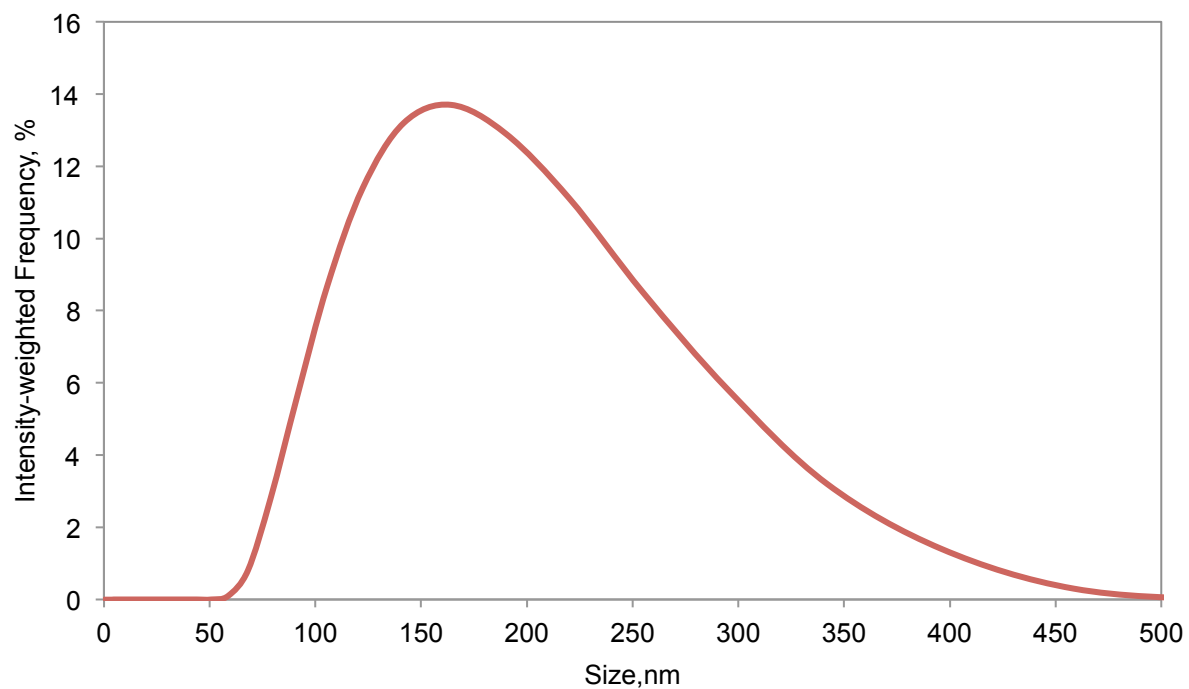
Figure 2.3 Representative size distribution of the original suspension of PEGylated nanoparticles as determined using DLS used in MATLAB simulations.

Magnetic Field Map

For the purpose of this simulation, a magnetic field map was created using data provided by the manufacturer representing five non-interacting ¼"x¼" cylindrical neodymium magnets (K&J Magnetics, Pipersville, PA) secured in permanent positions with 7.5 mm spacing between each one as seen in Figure 2.4a. The use of a series of equally spaced smaller magnets was chosen over a single large magnet in an effort to limit the chances of particle agglomeration that might occur if the particles were constantly magnetized.

(A)

(B)
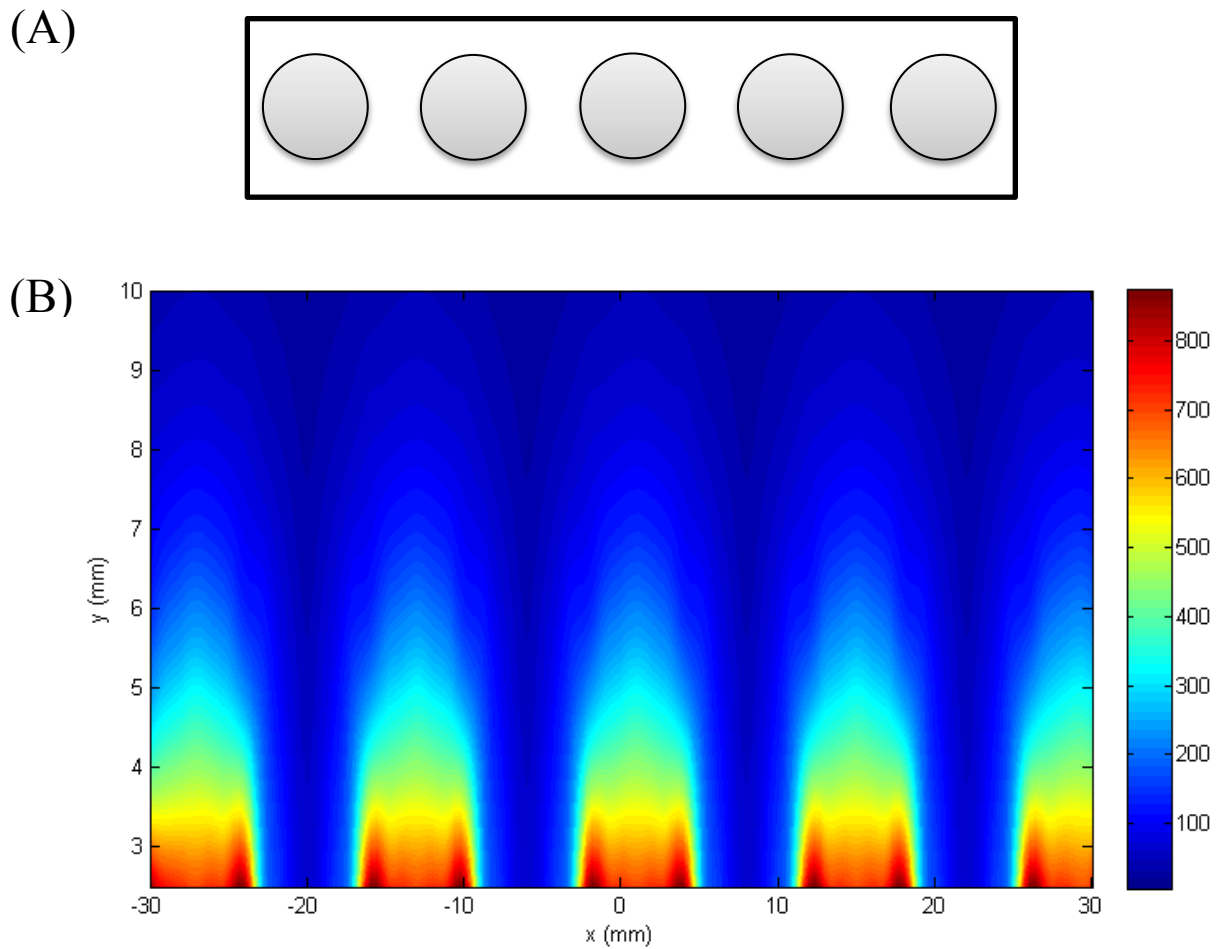
Figure 2.4 (A) Illustration of the orientation of the sequence of magnets used for the simulation. (B) Magnetic field map generated using data from the manufacturer in MATLAB for a series of five non-interacting ¼" cylindrical magnets. The temperature map legend is shown here in units of mT.

2.2.5 Magnetic Separation Prototype Operation

An experimental setup was created similar to the system modeled using MATLAB as seen in Figure 2.5. This magnetic separation prototype was created using styrofoam to create a container for the 5 cylindrical magnets and a platform for the tubing. 1/16" I.D. silicone tubing (VWR) was used to replicate the 2D channel in the simulation. 100μm flexible fused silica capillary tubing (Molex, Lisle, IL) was used to inject the nanoparticle solution into the mobile phase at the wall opposite the magnets. This tubing was connected to a 1mL syringe fitted with a 30G needle via a small section of 0.011" ID polyethylene tubing (Clay Adams, Sparks, MD). The mobile phase was supplied by two syringe infusion pumps (KD Scientific, Holliston, MA) in order to control the flow rate of the system.

For a typical run, the desired flow rate of the mobile phase was set using the syringe pumps and infusion was started. The nanoparticle solution was then injected into the tubing by applying a small amount of pressure to the syringe plunger. The nanoparticle suspension was continually injected until the desired volume had been run through the magnetic separation prototype. After this, infusion of the mobile phase was terminated and the two obtained fractions were characterized. The whole system was flushed sufficiently with DI water to ensure no cross-contamination between runs.
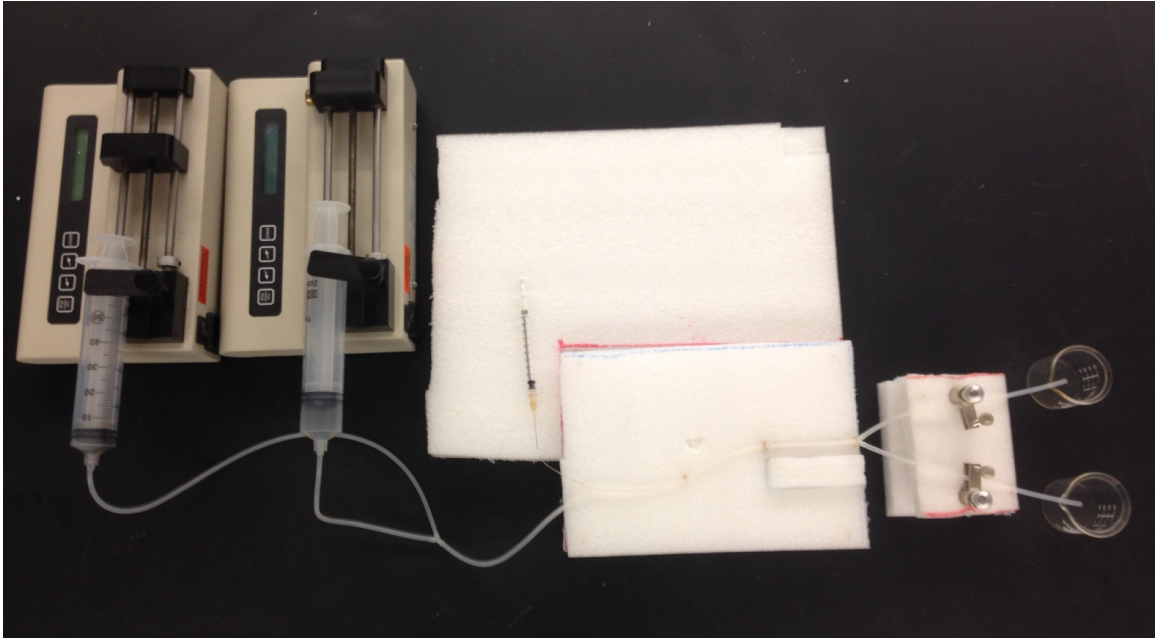
Figure 2.5 Digital image of magnetic separation prototype developed to replicate the conditions of the MATLAB simulation.

(A)
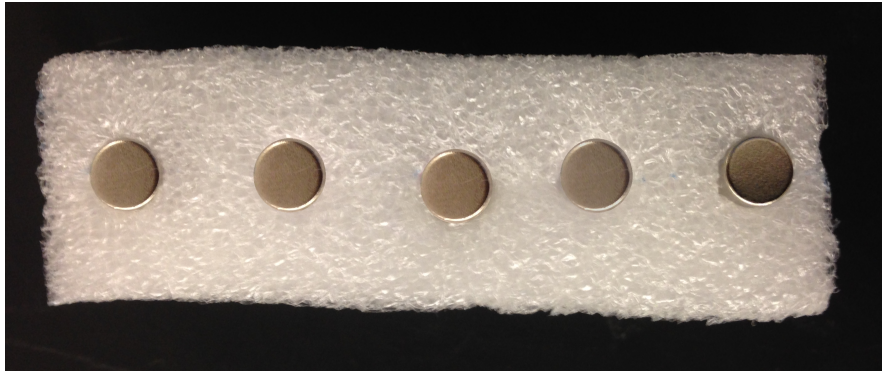
(B)
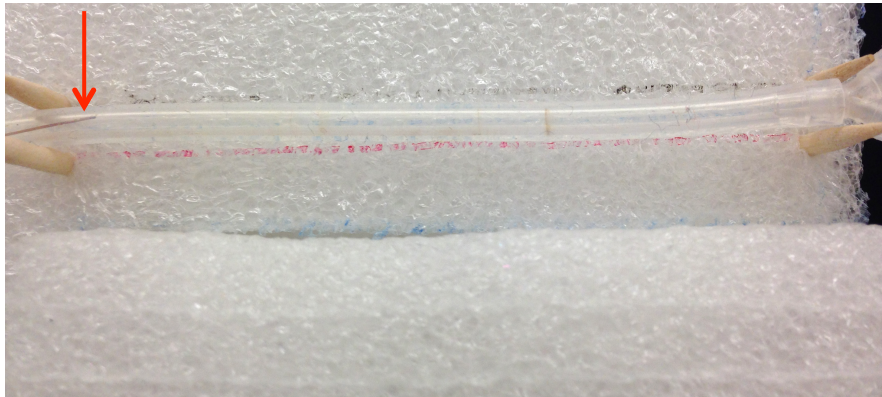
Figure 2.6 Digital images of (A) the sequence of magnets used to replicate the magnetic field used in the MATLAB simulations and (B) a closer look at the tubing at the surface of the magnets. The red arrow highlights the location of the microtubing used to inject the particles at the wall opposite the magnets.

2.2.6 Field-Flow Fractionation Prototype Operation

For all experiments used in determining the feasibility of field-flow fractionation for size-selective separation, the desired volume of concentrated nanoparticle suspension was injected into 1/8" ID silicone tubing (VWR, Radnor, PA) in the absence of flow from the mobile phase. The nanoparticles were then allowed to collect at the wall of the tubing closest to the magnet for a period of 15 minutes to allow for a steady-state distribution of particles at the tubing wall. The mobile phase was the introduced at a low initial flow rate using a peristaltic pump (Thermo Fisher Scientific, Waltham, MA) in order to wash away any MNPs which had not collected at the tubing wall. After a sufficient volume of the mobile phase had flown through the setup, flow from the pump was stopped, the sample volume was removed from the collection vessel for characterization, and then the collection vessel was rinsed with DI water and placed at the outlet. A higher flow rate was then introduced into the system and another sample was collected. This process was repeated for all desired flow rates supplied by the pump. Lastly, the MNPs that remained in the tubing were removed from the magnetic field and flushed from the tubing by shortly reintroducing the mobile phase. Each system was flushed sufficiently with DI water to ensure no cross-contamination between runs.

2.3 Results and Discussion

2.3.1 Determination of the Feasibility of Proposed Magnetic Separation Device

In order to determine the feasibility of separating magnetic nanoparticles in a size-selective manner by using flow through a magnetic field, a series of simulations were performed to discern whether the proposed method would allow for separation of

particles by size and, if so, identify optimal conditions required to obtain an efficient level of separation.

The Effect of Mobile Phase Viscosity and Velocity on Size Separation

As an initial feasibility study, two different sizes of nanoparticles, 50 nm and 150 nm, were selected from the range of sizes present in the PEG-MNP suspension observed via DLS to be modeled using the MATLAB script in order to understand how differences in size affect particle behavior in flow through a constant magnetic field gradient. In addition to determining the effect of size on the simulation outcome, a "high" and "low" value for both the viscosity and velocity of the mobile phase was used to discern the how the physical properties of the mobile phase affects particle behavior. The selection of these values was based on a series of preliminary simulations to determine what range of values would best illustrate the effect of the fluid viscosity and velocity. For the viscosity of the mobile phase, the viscosity of an aqueous 30wt% glycerine solution was used for the upper value of 2.5 mPa·s and the viscosity of water was used for the lower value of 1.005 mPa·s (Segur & Oberstar 1951). Both viscosities are for the selected fluids at 20°C. A velocity of 0.03 m/s was used as the upper value of the mobile phase velocity and 0.01 m/s was used as the lower value. The resulting particle trajectories for each condition can be seen in Figure 2.7.

From the simulation results it can be seen that the size of the particles has a significant effect on the resulting trajectories. The viscosity and velocity of the mobile phase also affect particle behavior, both individually and in combination with one another. The individual effects of the viscosity and velocity are shown in Figure 2.7b & 2.7c. Figure 2.7a illustrates the combined effect of the viscosity and velocity on the

predicted particle paths for the 50nm and 150nm nanoparticles for the low value conditions. At these condition the 150nm easily traverse the width of the channel indicating that all particles 150nm and larger would be collected in Fraction 2. Recall that if a particle has a final y-position greater than y = 0, it is assumed to be in Fraction 1, otherwise it is assumed to be in Fraction 2. The 50nm particles, however, which are some of the smallest particles observed in the original suspension, are also able to easily move across the channel resulting in a limited separation of differently sized particles. The level of dispersion observed with the 50 nm particles can be explained by the increased residence time within the magnetic field due to the lower velocity and the increased diffusion due to Brownian motion as a result of the lower viscosity as per equation 8. This results in a separation in which only the very small (i.e. around 50nm and smaller) will be present in Fraction 1 and the vast majority of particles will be collected in Fraction 2. On the other hand, if the viscosity and velocity of the mobile phase are too high, none of the particles are able to move across the channel as seen in Figure 2.7d. According to the simulation, at the conditions of high viscosity and high velocity, there is little difference in the behavior between the differently sized particles thereby resulting in no separation at the end of the channel. From this series of simulations it can be concluded that in order to achieve an effective level of size separation, an optimal mobile phase viscosity and velocity should be identified and used.
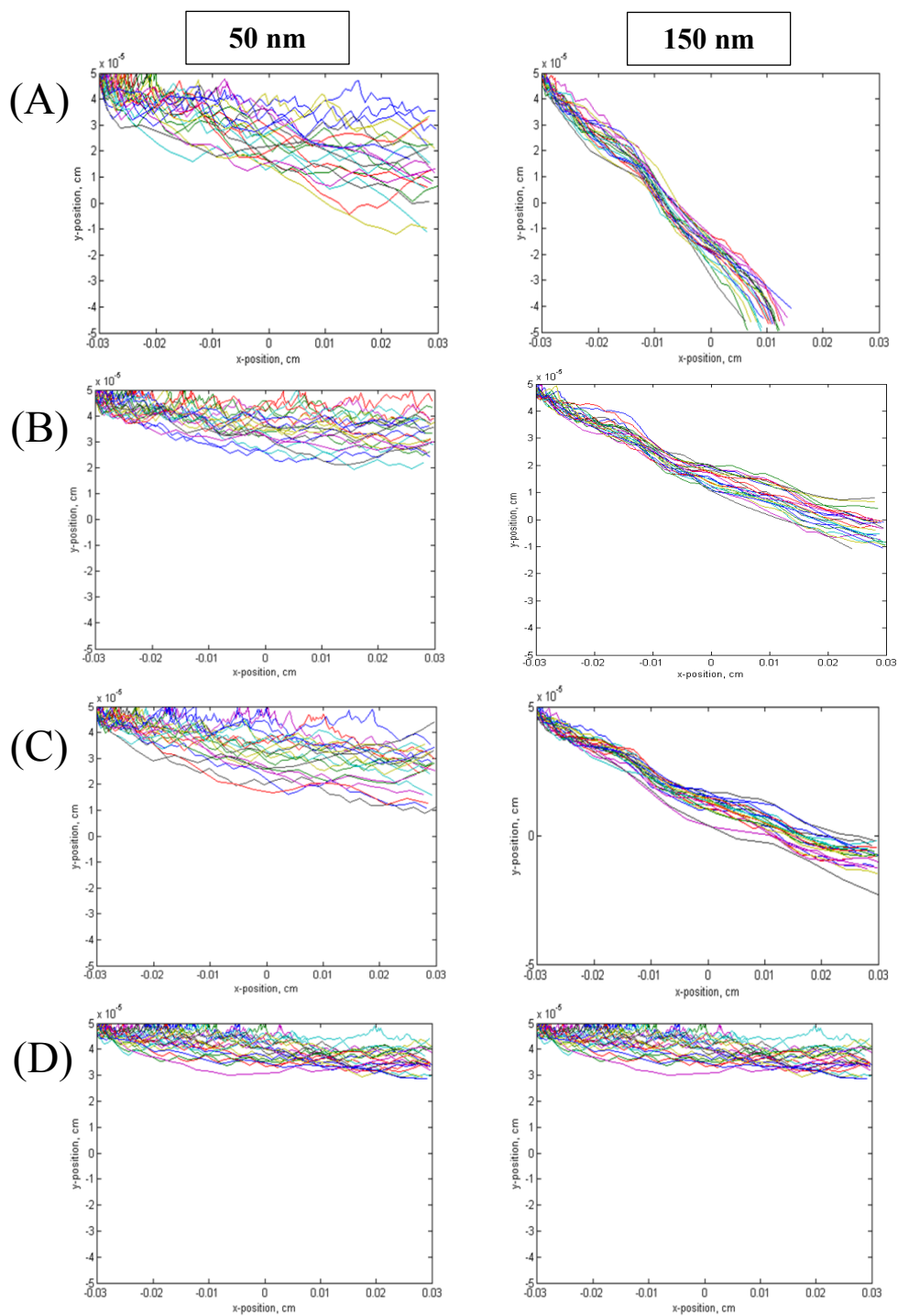
Figure 2.7 The predicted particle paths of 50nm and 150nm iron oxide nanoparticles in a1mm channel for mobile phase velocities and viscosities of (A) 0.01 m/s, 1.002 mPa·s, (B) 0.03 m/s, 1.002 mPa·s, (C) 0.01 m/s, 2.5 mPa·s, and (D) 0.03 m/s, 2.5 mPa·s, respectively.

	Viscosity/Velocity			
MNP Size	Low/Low	Low/High	High/Low	High/High
50 nm	34.2 ± 13.3%	19.1 ± 7.9%	20.8 ± 8.3%	12.2 ± 4.9 %
150 nm	100 ± 0.0%	52.8 ± 4.8%	59.3 ± 4.4%	29.9 ± 2.8 %

Table 2.1 The average percentage of the channel width traversed by 50nm and 150nm particles for each condition of the mobile phase (low viscosity = 1.002 mPa·s, high viscosity = 2.5 mPa·s, low velocity = 0.01 m/s, and high velocity = 0.03 m/s). Where 0% would be the wall at which the nanoparticles enter the mobile phase and 100% would be the wall closest to the magnets.

Identification of Effective Experimental Conditions

A series of simulations were run in which the viscosity and velocity of the mobile phase were varied in order to identify potential experimental conditions that would allow for the effective separation of the PEG-MNP suspension based on the limitations of the designed prototype. Specifically, the maximum infusion rate of the syringe pumps to be used (2.2 ml/min) was considered the upper limit for the range of velocities to be simulated. Additionally, the surface of the magnets was specified to be 10mm from the center of the tubing. With these specifications, a combination of velocity and viscosity values was sought that would allow for approximately 50% of the particles present in the solution to be collected in each Fraction. It was found that this type of separation could be achieved with a fluid velocity of 0.0182 m/s and viscosity of 1.005 mPa·s as seen in Figure 2.8b. Keeping all other conditions constant, distance of the magnet from the center of the tubing was varied in order to obtain two other separations, one in which the magnets were closer than 10mm (7.5 mm) and one where the magnets are farther than 10mm (11.5 mm), to be repeated experimentally. The predicted particle paths and theoretical resulting size distributions compared to the original size distribution can be found in Figure 2.8.
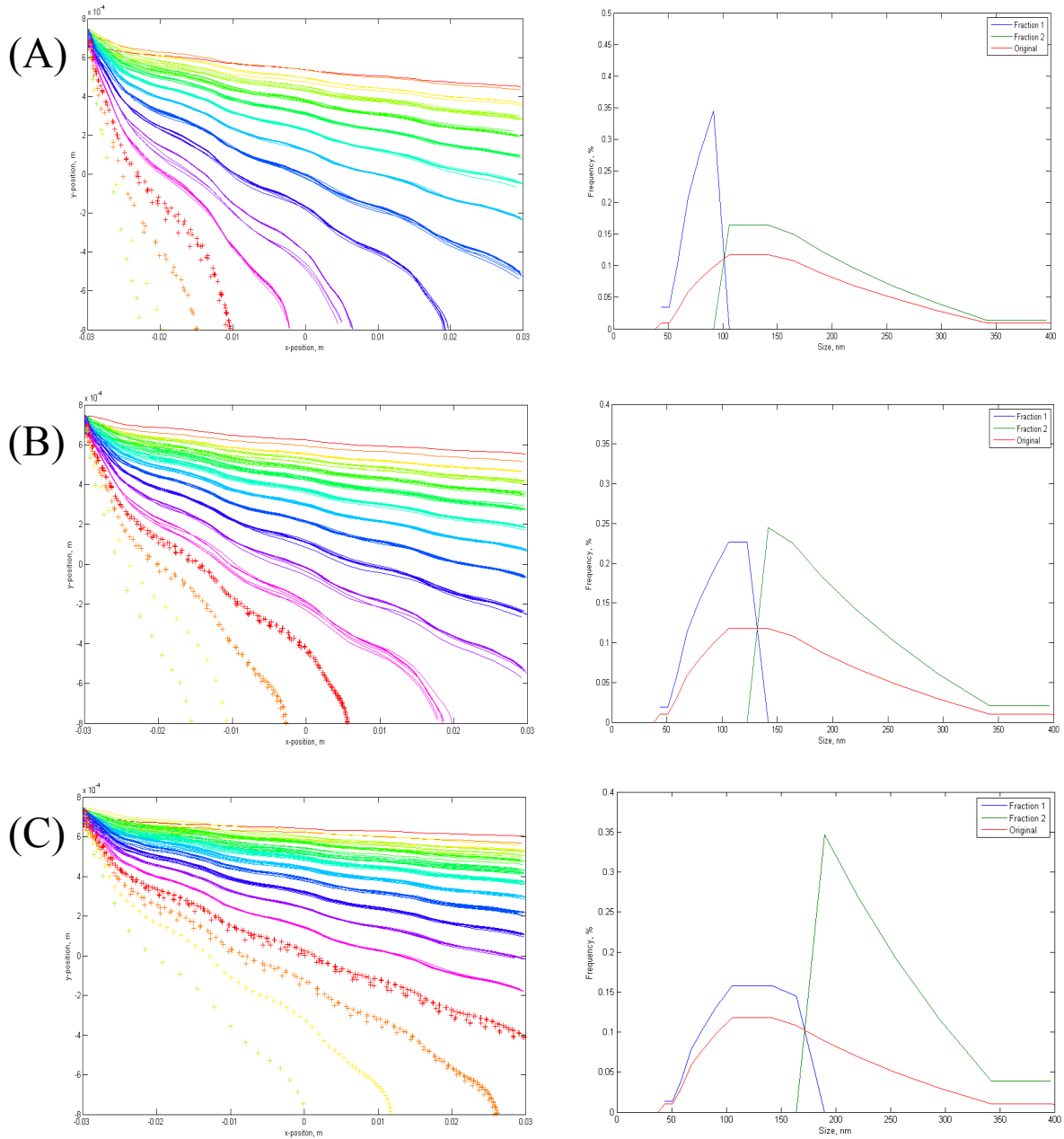
Figure 2.8 Predicted particle trajectories and resulting size distributions for Fraction 1 and Fraction 2 for magnet distances of (A) 7.5mm, (B) 10mm, and (C) 11.5 mm. Particle trajectory data sets based on size, with - 43.82 nm, - 50.75 nm, - 58.77 nm, - 68.06 nm, - 78.82 nm, - 91.28 nm, - 105.7 nm, - 122.4 nm, - 141.8 nm, - 164.2 nm, - 190.1 nm, - 220.2 nm, + 255.0 nm, + 295.3 nm, + 342.0 nm, & + 396.1 nm.

2.3.2 Experimental Validation of MATLAB Model

In order to confirm the results obtained using the MATLAB simulation, a magnetic separation prototype was created to reproduce the conditions of the simulation. As with the model, 1.6mm I.D. tubing was used to replicate the 2D channel and 100μm I.D. tubing was used to ensure that the MNPs entered the mobile phase at the wall opposite the magnets. The magnets were placed in a permanent location and markings were made at distances of 7.5 mm, 10 mm, and 11.5 mm from their surface so that the center of the tubing could be placed at the desired distances in a repeatable manner.

Upon completion of attempted separations at the three different tubing positions, the samples appeared as those pictured in Figure 2.9a. There was a clear visual difference in the samples taken from Fraction 1 (pictured on left) and Fraction 2 (pictured on right) for the three runs that seemed to coincide with the predicted behavior. For example, in the case of the magnets being 11.5 mm from the center of the tube (pictured top), it was predicted that a majority of the particles would be found in Fraction 1, with only the larger particles (>200 nm) being found in Fraction 2. The samples pictured in Figure 2.9a seem to agree with this result as the concentration in Fraction 1 appears to be higher than that of Fraction 2 due to the increased coloration. Conversely, in the case of a distance of 7.5 mm (pictured bottom), the Fraction 1 and Fraction 2 samples are the visual opposite of those for the distance of 11.5 mm. This is to be expected as from the simulation results a majority of the particles should be found in Fraction 2, as opposed to Fraction 1.However, when the collected samples were characterized using DLS it was found that all of the samples that had the golden coloring possessed size distributions nearly identical to that of the original solution as seen in Figure 2.9c. The samples that did not

show any signs of coloration (i.e. Fraction 2 for 11.5 mm & Fraction 1 for 7.5mm) were too dilute to obtain a DLS measurement, possibly indicating the complete absence of particles.

As mentioned, the MATLAB simulation was created as a simple model of the proposed system and therefore did not account for particle-particle interactions. After analyzing the obtained results, it was hypothesized that particle-particle interactions were causing the MNPs to behave as a ferrofluid-type entity as opposed to individual particles. It is well-established that with increasing concentration, inter-particle distance decreases resulting in an increase in particle-particle interactions (Kourki & Famili 2011). The original MNP suspension was significantly concentrated in an effort to limit the level of dilution that occurred upon the injection of the MNP suspension into the mobile phase. This dilution occurs due to the volume of MNP suspension injected during a run being a small fraction (~1:220) of the volume of the mobile phase. In response to these results, the experiments were repeated using dilutions of the original MNP suspension. However, these experiments were not successful as either the same results were obtained or the samples were too dilute to accurately characterize. It was therefore concluded that it was not possible to replicate the results of the simulation using the current prototype.
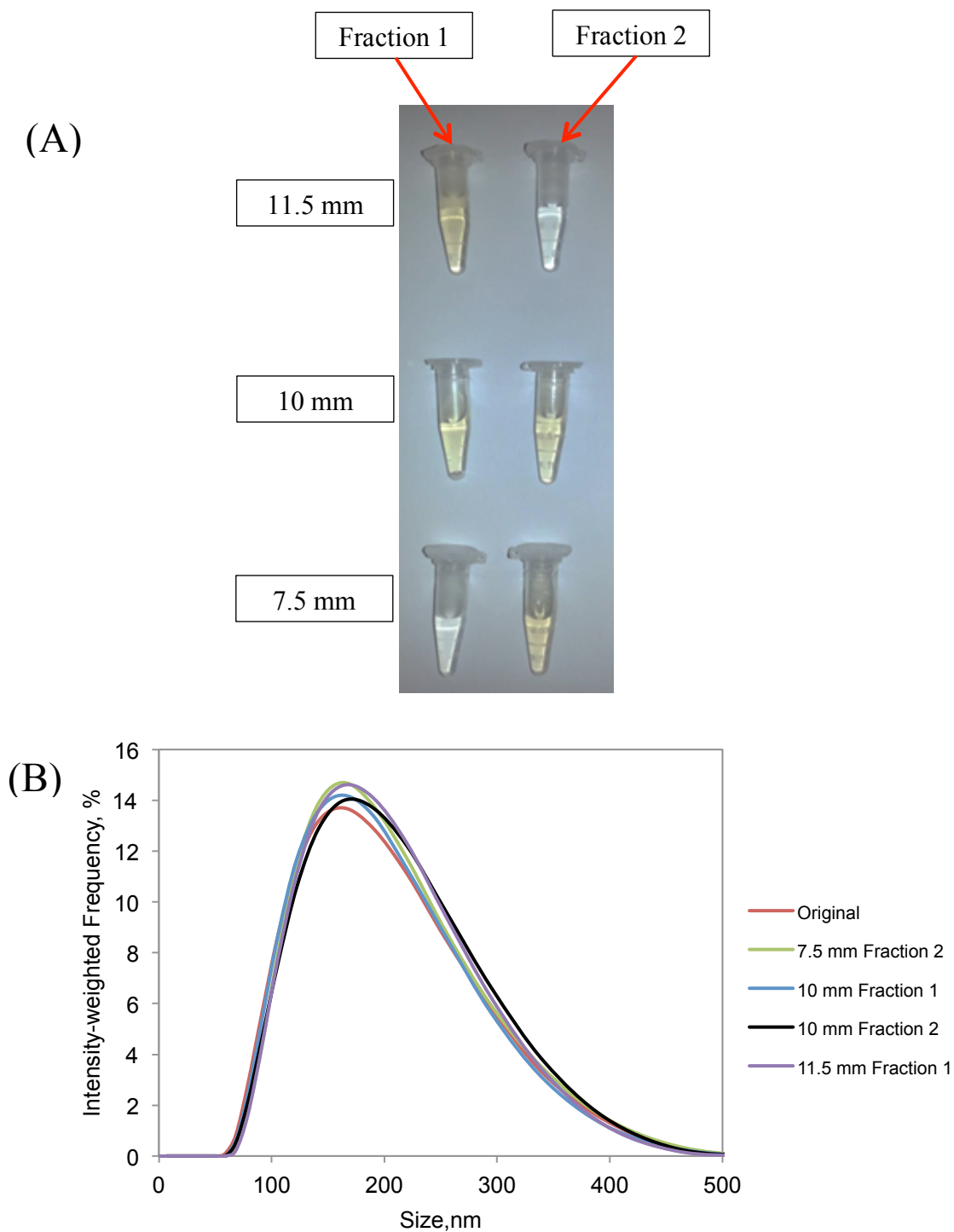
Figure 2.9 Results from experimental runs using the magnetic separation prototype. (A) Digital image of Fraction 1 (left) and Fraction 2 (right) samples collected from the magnet distances of, from top to bottom, 11.5 mm, 10 mm, and 7.5 mm. (B) Size distributions of the obtained colored samples compared to that of the original MNP suspension.

Sample	Average Hydrodynamic Diameter (nm)
Original	178.8 ± 71.6
7.5mm Fraction 2	183.2 ± 70.7
10mm Fraction 1	178.6 ± 69.6
10mm Fraction 2	185.5 ± 71.7
11.5mm Fraction 1	183.7 ± 68.6

Table 2.2 Average hydrodynamic diameter of samples obtained using magnetic separation prototype based on statistical analysis of intensity-weighted frequency data from DLS measurements.

2.3.2 Field-flow Fractionation Approach to Size-Selective MNP Separation

In response to the issues faced with the initial approach to the size-selective separation of magnetic nanoparticles, an alternative approach was considered. Whereas the previous approach attempted to separate the particles from fluid flow using magnetic force, the new approach sought to separate particles from a magnetic field using force due to fluid flow in a manner very similar to magnetic field-flow fractionation. Magnetic field-flow fractionation is based on the ability to exploit the differences in the experienced magnetic force of different materials. Briefly, the magnitude of the magnetic force in a constant magnetic field is a size-dependent property, with the magnitude increasing as particle size increases. Therefore, if two differently sized magnetic particles are in the same constant magnetic field, the force required to counteract the magnetic force experienced by the smaller particle is lower. This lends itself to the ability to separate particles in a size-dependent manner by applying a variable force to counteract the magnetic force. In this case of magnetic field-flow fractionation, the counteracting force is the fluid drag force experienced by particles when a mobile phase is applied..

MagLine

The first iteration of a prototype devised for the size-selective separation of magnetic nanoparticles using magnetic field-flow fractionation was termed MagLine and is pictured in Figure 2.10. In short, the MagLine was composed of three 3" rectangular magnets (Amazing Magnets,Irvine, CA) in line with one another secured in styrofoam. The original PEG-MNP was injected into the entire volume of the 1/8" I.D. tubing at the surface of the magnets. A total volume of 1.8 mL of MNP suspension could be separated in a single run using this setup. After allowing the particles to reach a steady-state

distribution at the tubing wall a series a flow rates was applied and samples collected for characterization. This process was repeated in triplicate to ensure repeatability and an average size distribution for each flow rate was determined. These average size distributions are plotted for comparison in Figure 2.11.Using statistical analysis of the average size distributions for flow rates of 10, 20, 30, 40, 50 ml/min as well as the flushed remaining particles (denoted as LO), the MagLine was able to separate the original MNP distribution into sizes of 104.3 ± 36.9, 118.8 ± 27.5, 134.3 ± 21.3, 149.8 ± 16.3, 158.3 ± 33.2, and 168.6 ± 11.6 nm, respectively.
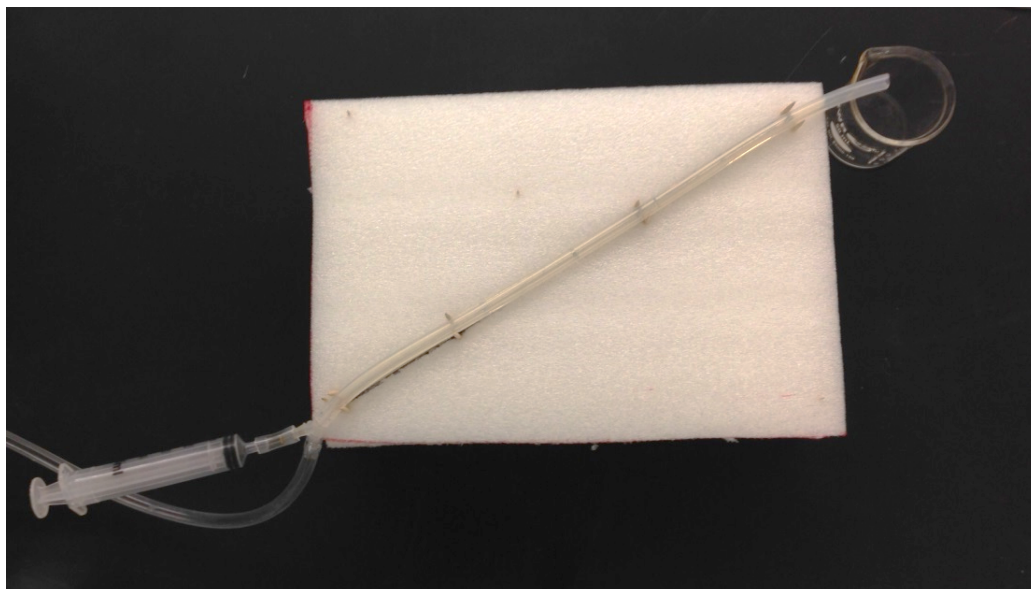
Figure 2.10 Digital image of MagLine magnetic separation prototype composed of 1/8"

I.D. run along the surface of three 3" bar magnets in series.
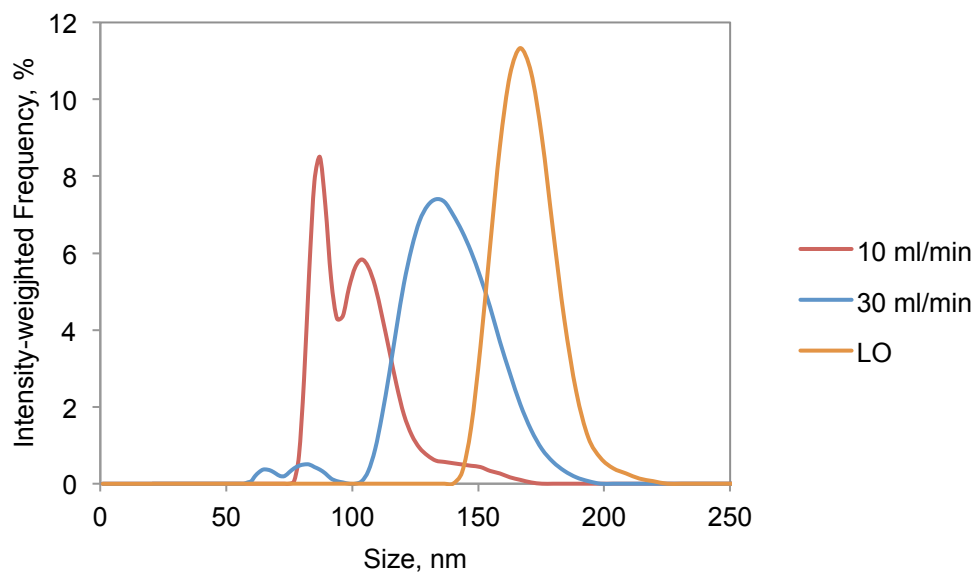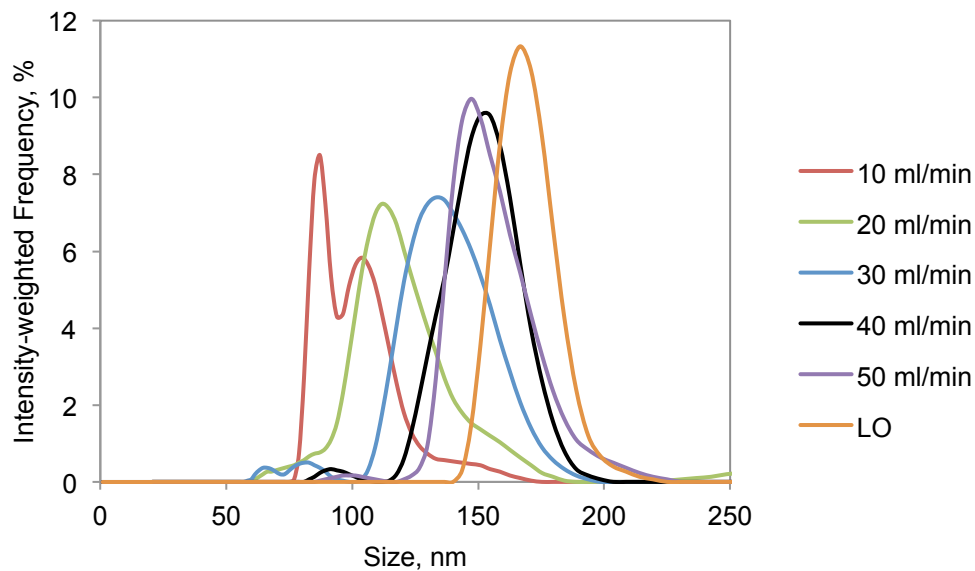
Figure 2.11 Average size distributions obtained using the MagLine prototype and flow rates of 10, 20, 30, 40, and 50 ml/min, as well as the flushed particles (LO) calculated from the results of three separate experimental runs. The second graph is provided to illustrate the three most distinct separations obtained out of the six samples characterized.

MagWrap

  Following the successful size-selective separation using the MagLine, a new arrangement was developed in an attempt to improve the quality of the separation and the scalability of the system. This new design, called the MagWrap, utilized a Grade N42 2" diametrically magnetized neodymium cylinder (Applied Magnetics, Plano, TX) with 1/8" I.D. tubing wrapped around so as to be in contact at both of its poles as seen in Figure 2.12. While the total volume of MNP suspension that could be separated in a single run was half that of the MagLine (0.9mL vs. 1.8 mL), it was hypothesize that the stronger magnetic field would enable a higher concentration of MNPs to be retained through the first flow rate, thus increasing the concentration of the samples obtained. The same approach was used as with the MagLine and the resulting size distributions that were obtained are shown in Figure 2.13. Utilizing the same flow rates as before, the MagWrap achieved samples of sizes 106.8 ± 9.0, 103.4 ± 6.1, 120.6 ± 28.9, 136.1 ± 15.3, 153.7 ± 15.6, and 173.4 ± 15.1 nm. The MagWrap appeared to provide slightly more distinct separations compared to those of the MagLine as evidenced by the overall decrease in the standard deviations of distributions obtained using the same flow rates.
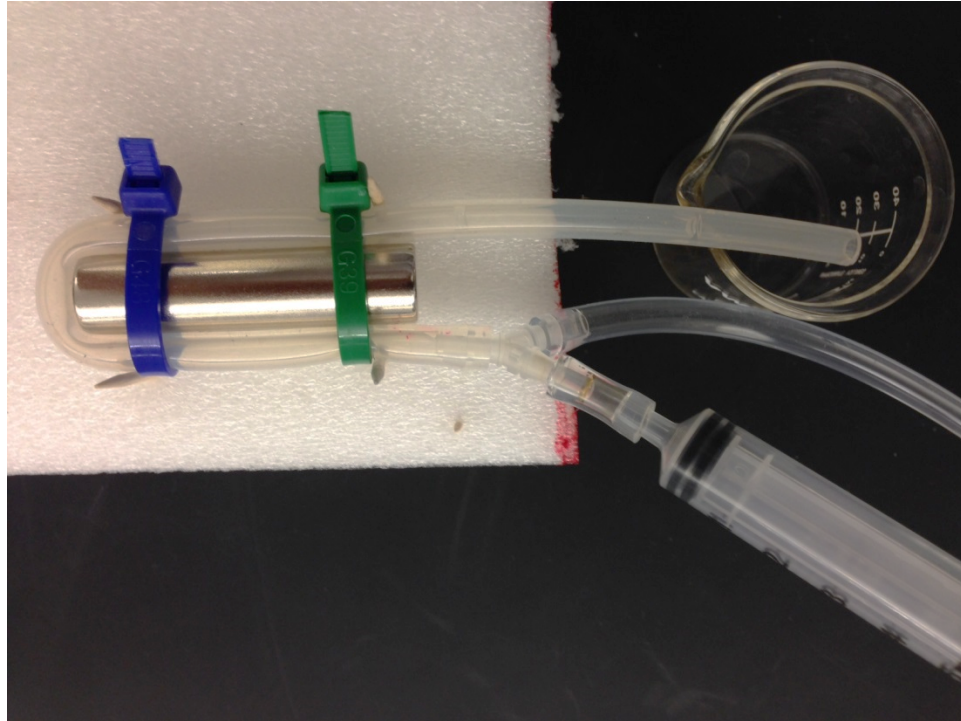
Figure 2.12 Digital image of MagWrap magnetic separation prototype composed of 1/8"

I.D. tubing wrapped along both poles of a 2" diametrically magnetized cylinder.
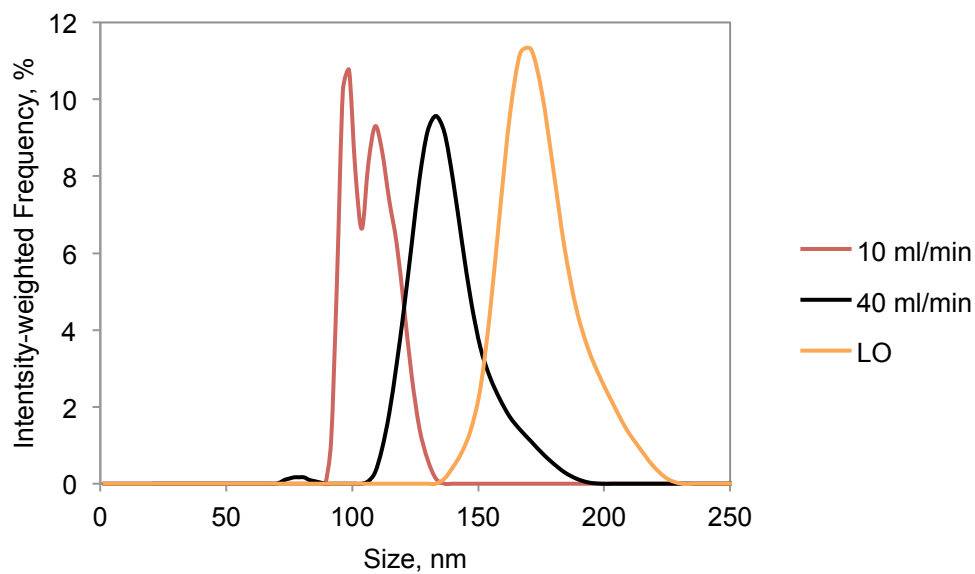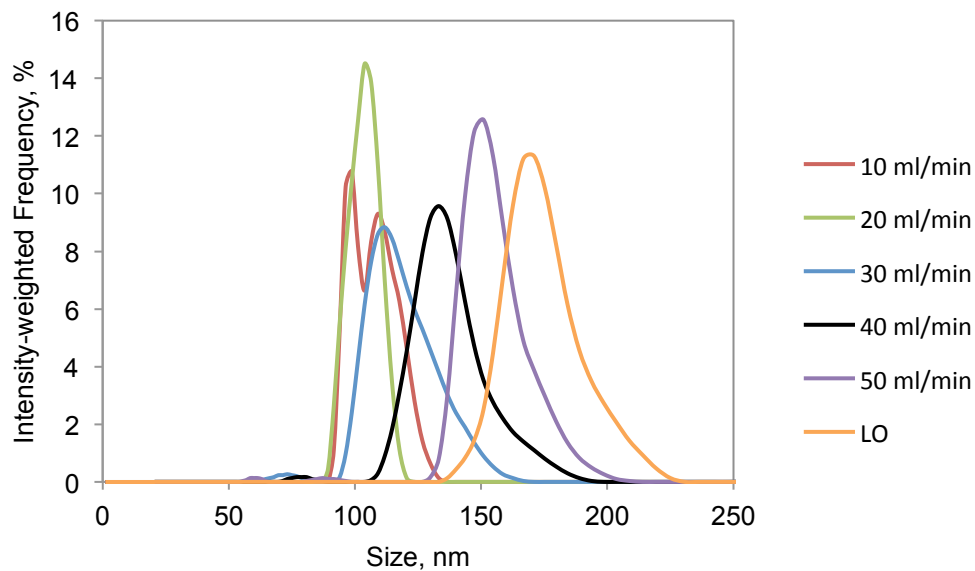
Figure 2.13 Average size distributions obtained using the MagWrap prototype and flow rates of 10, 20, 30, 40, and 50 ml/min, as well as the flushed particles calculated from the results of three separate experimental runs. The second graph is provided to illustrate the three most distinct separations obtained out of the six samples characterized.

MagCoil

To further improve the scalability and effectiveness of the system, a third design, termed MagCoil, was developed in which the tubing was wrapped around the cylindrical magnet several times over its entire length as seen in Figure 2.14. By wrapping the tubing in this manner, the utilized surface area of the magnet is maximized, thus allowing for MNP suspension volumes of up to 3.4 mL to be separated in a single run. The same approach was used for the separation and the resulting size distributions are show in Figure 2.15. Using the MagCoil and the same flow rates used with the MagLine and MagWrap, MNP sizes distributions of 112.8 ± 11.5, 119.8 ± 7.6, 136.0 ± 26.0, 142.5 ± 10.8, 152.2 ± 11.1, and 175.0 ± 14.6 nm were obtained. In addition to being more scalable than the previous two designs, the MagCoil was also noticeably more repeatable when comparing the results of obtained using each design.
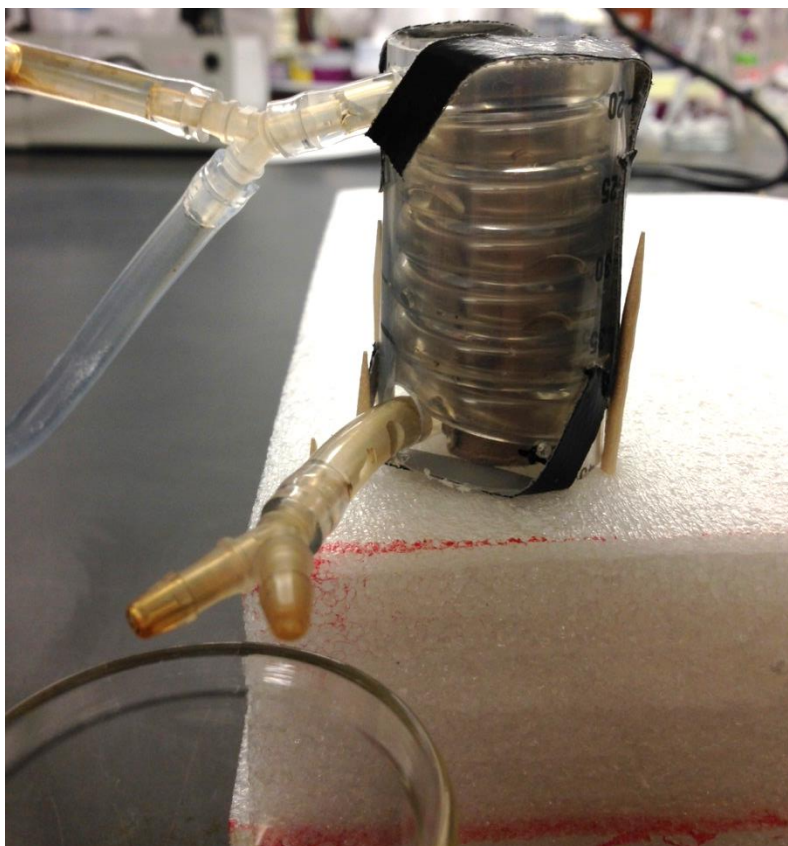
Figure 2.14 Digital image of MagCoil magnetic separation prototype composed of 1/8"
I.D. tubing wrapped around the length of a 2" diametrically magnetized cylinder encased
in a plastic column for stability.
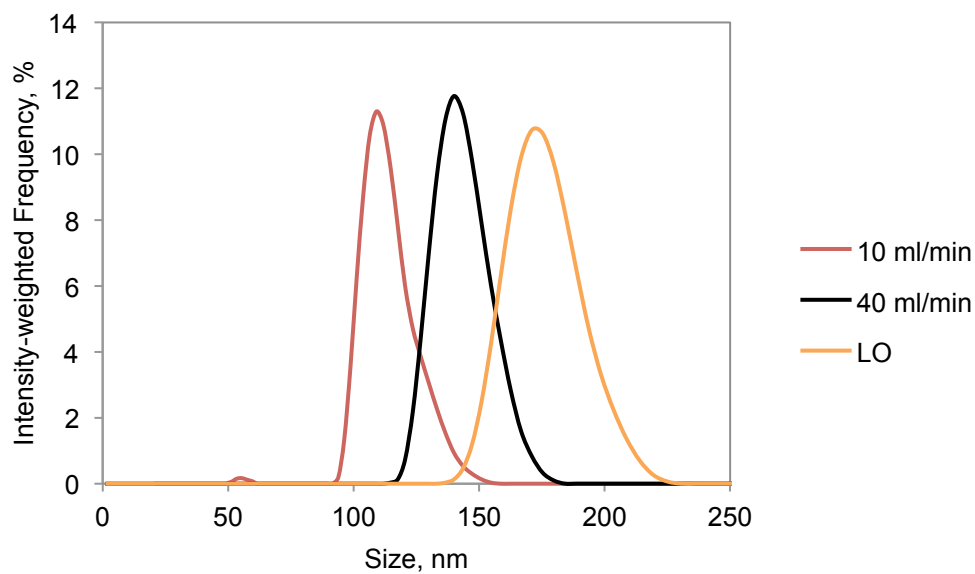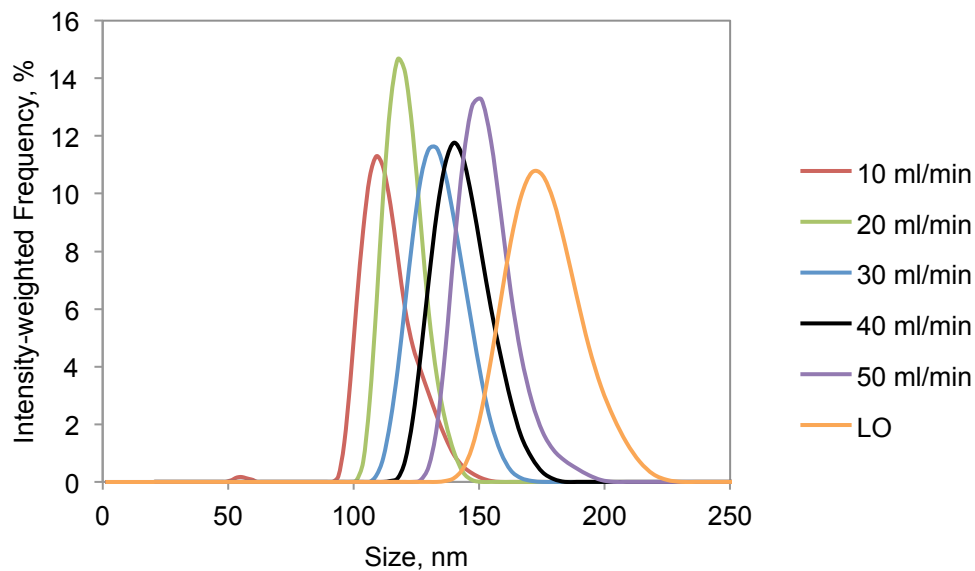
Figure 2.15 Average size distributions obtained using the MagCoil prototype and flow rates of 10, 20, 30, 40, and 50 ml/min, as well as the flushed particles calculated from the results of three separate experimental runs. The purpose of the second graph is to illustrate the three most distinct separations obtained out of the six samples characterized.

	MagLine	MagWrap	MagCoil
10 ml/min	104.3 ± 36.9	106.8 ± 9.0	112.8 ± 11.5
20 ml/min	118.8 ± 27.5	103.4 ± 6.1	119.8 ± 7.6
30 ml/min	134.3 ± 21.3	120.6 ± 28.9	136.0 ± 26.0
40 ml/min	149.8 ± 16.3	136.1 ± 15.3	142.5 ± 10.8
50 ml/min	158.3 ± 33.2	153.7 ± 15.6	152.2 ± 11.07
LO	168.6 ± 11.6	173.4 ± 15.1	175.0 ± 14.6

Table 2.3 Average hydrodynamic diameter of samples obtained using the MagLine, MagWrap, and MagCoil separator prototypes based on statistical analysis of intensity-weighted frequency data from DLS measurements.

TEM analysis was performed to both confirm the occurrence of size-dependent separation of the original MNP suspension and for comparison with the obtained DLS results. Figure 2.16 shows a TEM image of the original suspension, designated as MNP-O, and the corresponding histogram obtained from the subsequent analysis of TEM images. The average size of the original suspension was found to be 75.4 ± 47.7 nm compared to 137.21 ± 20.8 nm determined using DLS. It is important to note that TEM measurements provide the size of the core diameter while DLS measurements are based on the hydrodynamic diameter and should therefore be expected to be different from one another. Sample images that are representative of each size distribution analyzed are given in Figure 2.17 and histograms for each sample are shown in Figure 2.18. The distributions obtained after the separation were named according to their average size measured using DLS. Upon analysis of the TEM images the average core diameters were found to be 62.6 ± 27.2, 80.7 ± 45.1, and 104.6 ± 62.3 nm for the distributions MNP-96, MNP-124, and MNP-142, respectively. A comparison of the measured sizes using both TEM and DLS are given in Table 2.4.
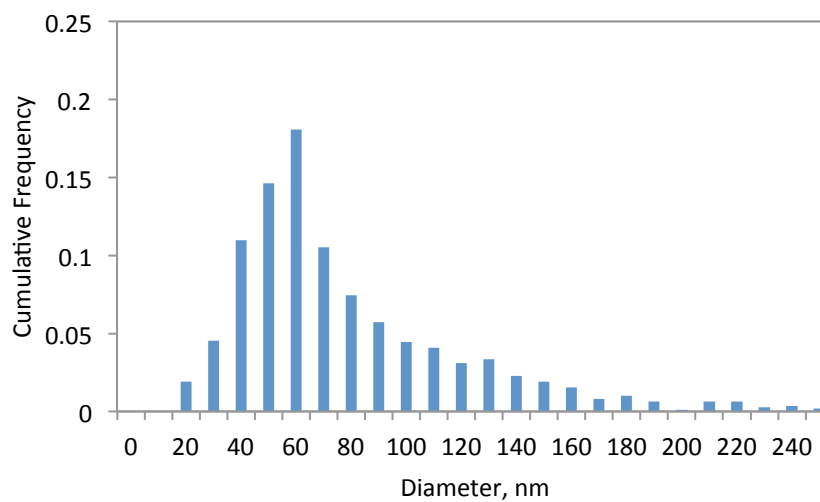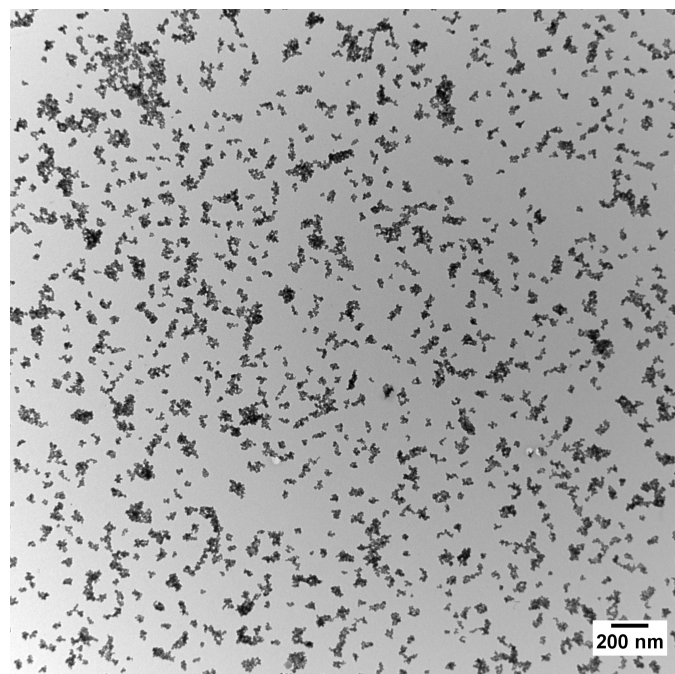
Figure 2.16 Representative TEM image at 12.5K magnification of original nanoparticle suspension, MNP-O, before separation and corresponding size histogram obtained from TEM analysis.
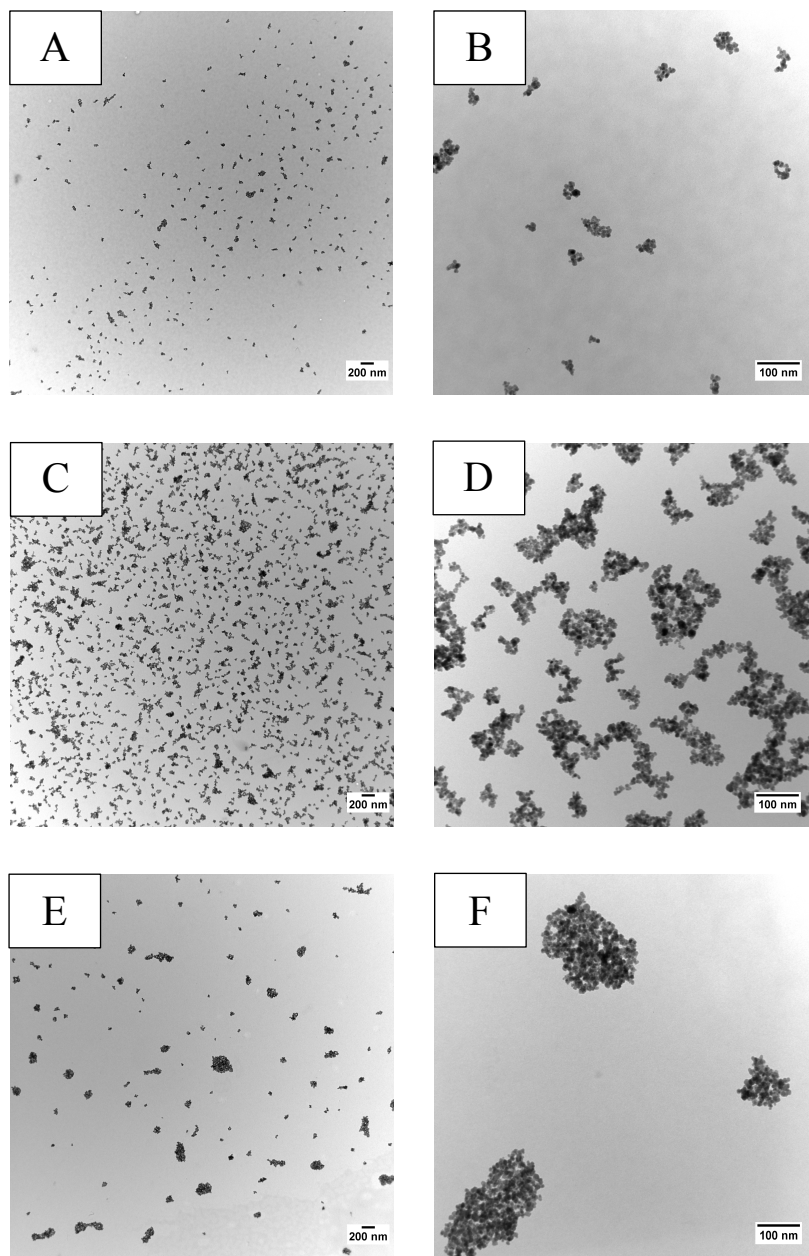
Figure 2.17 Representative TEM images of (A,B) MNP-96, (C,D) MNP-124, and (E,F) MNP-142 particle samples at 12.5K and 80K magnification, respectively.
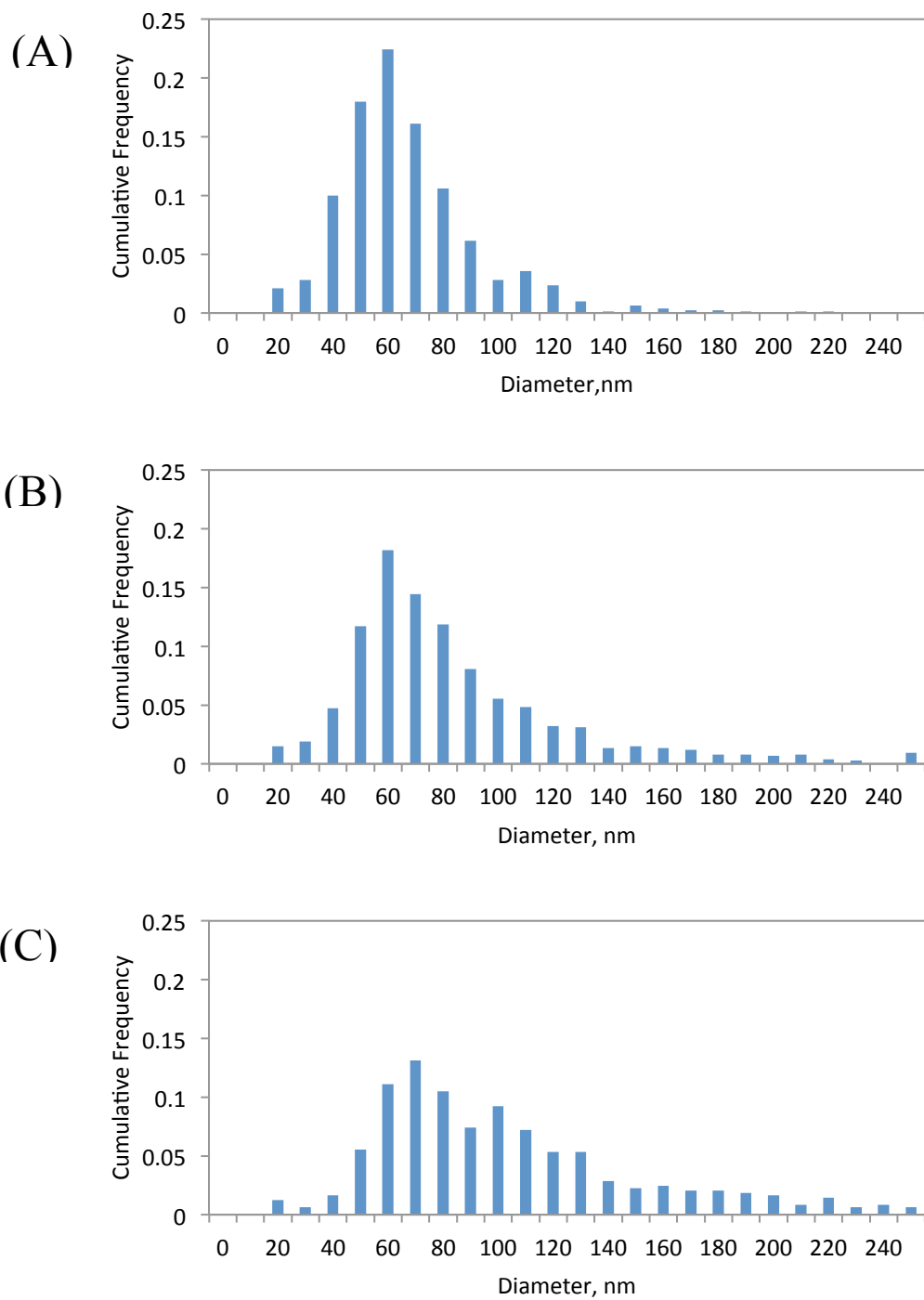
Figure 2.18 Size histograms obtained from TEM analysis of obtained separations (A) MNP-96, (B) MNP-124, and (C) MNP-142.

	DLS (nm)	TEM (nm)
MNP-O	137.21 ± 20.8	75.4 ± 47.7
MNP-96	96.3 ± 9.0	62.6 ± 27.2
MNP-124	123.6 ± 7.9	80.7 ± 45.1
MNP-142	141.5 ± 10.8	104.6 ± 62.3

Table 2.4 Comparison of average hydrodynamic diameters measured using DLS and average core diameters determined using TEM for MNP-O, MNP-96, MNP-124, and MNP-142 distributions.

2.4 Conclusions

For the full potential of magnetic nanoparticles in nanomedicine to be realized, methods must be developed that allow for the distinct control of their physical and chemical properties so that particles may be optimized for specific applications. One of the most important factors that determines the behavior of magnetic nanoparticles *in vivo* is their size; however, couldn't synthesis methods do not allow for sufficient size control for iron oxide nanoparticles of size greater than 20 nm. To address this problem, an effective and scalable technique for the size-selective separation of magnetic nanoparticles utilizing a form of field-flow magnetization been developed. This method is based on the removal of magnetic particles from a polydisperse suspension in a constant magnetic field gradient in a size-dependent manner by applying a series of increasing flow rates of a mobile phase. Three different designs using this technique were created and tested experimentally. The distributions obtained were analyzed using both TEM and DLS to confirm the level of size separation achieved. The third design created, the MagCoil, was found to be the most scalable and consistent in its separations as shown when comparing the size distributions obtained at each flow rate across the three experimental runs (Appendix B). Further studies and optimization of the system presented in these investigations could allow for the acquisition of highly monodisperse size distributions of magnetic nanoparticles within the size range relevant for biomedical application of 20-200 nm. These distinct distributions can then be used in *in vitro* and *in vivo* studies to optimize magnetic nanoparticle size.

Chapter 3

Determination of the Effect of Size of Iron Oxide Nanoparticles

3.1 Introduction

Iron oxide nanoparticles have recently garnered large levels of interest in biomedicine, especially in the area of medical imaging. Their superparamagnetic properties and ability to effectively shorten the proton relaxation time make them attractive contrast agents for use with MRI. And while there are already several commercially available contrast agents composed of iron oxide nanoparticles, including Feridex and Resovist, there are still questions regarding the optimization of their properties for imaging applications. The physical properties of these nanoparticles, such as particle size, geometry, and chemical composition, have been shown to not only affect their biodistribution and pharmacokinetics *in vivo* but have also been demonstrated to affect their capabilities as contrast agents by altering their relaxometric properties (Jun et al. 2004, Tromsdorf et al. 2007). Further, the tuning of these properties is difficult with current clinically used T2 contrast agents due to their high level of polydispersity. Therefore, many recent investigations have sought to study the effects of the physical and chemical properties of iron oxide nanoparticles for the purpose of optimization.

Magnetic resonance images are obtained by applying perpendicular magnetic fields, one constant and one produced by a radiofrequency pulse, to induce a series of net magnetization and relaxation of hydrogen atoms within tissue. There are two types of

relaxation mechanisms that occur that enable the acquisition of MR images. The first type of relaxation is called longitudinal, or T1, relaxation and occurs due to the return of protons to their thermal equilibrium state and is a result of interactions with surrounding tissue. The second mechanism of relaxation is known as transverse, or T2, relaxation. T2 relaxation occurs due to the interaction of proton spins that occur during the period of the applied RF pulse. Contrast agents are used to shorten T1 or T2 relaxation times resulting in images with greater contrast owing to either increased positive signal for T1 contrast agents or decreased negative signal for T2 contrast agents. Iron oxide nanoparticles have been shown to markedly shorten T2 relaxation times and are therefore most often used for T2-weighted imaging. It has previously been shown that the size of both individual iron oxide nanocrystals and aggregates of particles (less than 100 nm) affects the resulting T2 values of the magnetic nanoparticles (Duan et al. 2008; Berret et al. 2006). For these size ranges, it has been established that transverse relaxivity R2 increases with particle/aggregate size. This phenomenon is typically attributed to the increase in saturation magnetization that coincides with an increase in particle size (Roca et al. 2009). While the effect of size on relaxivity for small particles less than 15 nm is fairly well understood, very little has been explored in regards to aggregates, especially for sizes greater than 100 nm.

In this chapter, the previously developed methods for the size-selective separation of magnetic nanoparticles are used to obtain distinct size distributions of iron oxide nanoparticles for the purpose of studying the effect of size on their relaxometric properties. The fractionated distributions are used in a series of concentration based MRI phantom studies in both aqueous solutions and tissue mimicking phantom gels. The T2

values of the differently sized suspensions are determined using a 3T scanner via a spin-echo sequence to determine the influence of size on the relaxivity R2 for magnetic nanoparticles of hydrodynamic diameters above 100 nm.
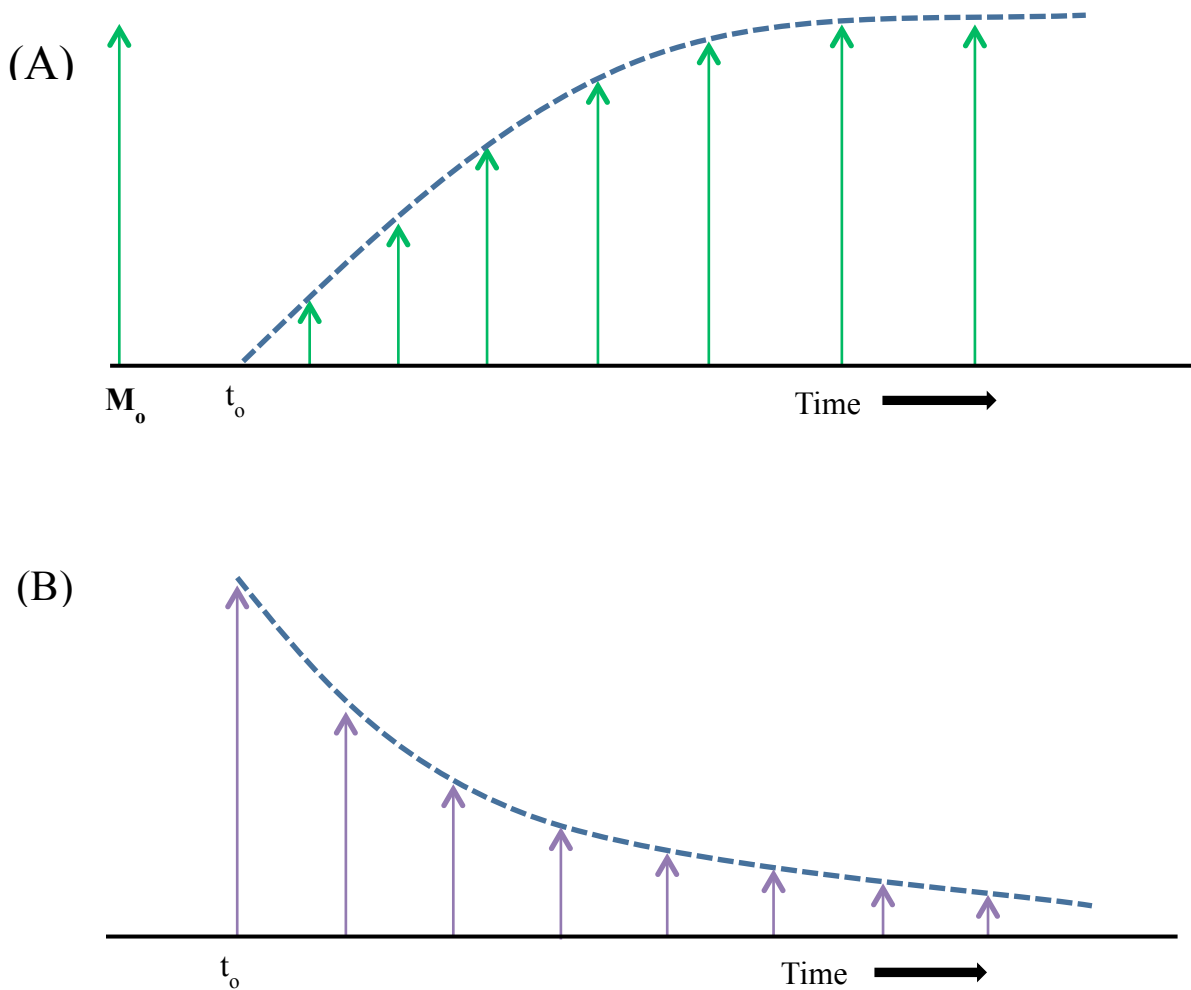
Figure 3.1 Illustration of T1 and T2 relaxation after the application of a 90° pulse at time t_o. The green and purple arrows represent the magnitude of the longitudinal and transverse magnetization, respectively. (A) At time t_o the magnitude of the longitudinal magnetization goes from M_o just after the pulse. As time progresses the magnetization returns to its equilibrium state M_o via T1 relaxation. (B) At time t_o the magnitude of the transverse magnetization goes from zero to some magnitude just after the pulse. As time progresses the magnetization returns to its equilibrium state at zero via T2 relaxation.

3.2 Experimental

3.2.1 Materials

fluidMAG-D (starch-coated magnetite (Fe_3O_4)) iron oxide nanoparticles (75mg/mL) were obtained from Chemicell® GmBH (Berlin, Germany). Succinimidyl polyethylene glycol (mPEG-NHS) of molecular weight 5 kDa was obtained from Nanocs (New York, NY). Dimethyl sulfoxide (($CH_3)_2SO$, 99.9%), sodium hydroxide (NaOH, 97%), and L-ascorbic acid ($C_6H_8O_6$) were obtained from BDH Chemicals. Epichlorohydrin (C_3H_5ClO, 99%), ammonium acetate, ACS (CH_3COONH_4, 97% min), . 1-propanol (C3H8O, 99+%), and thimerosal were obtained from Alfa Aesar. Ferrozine iron reagent, monohydrate was obtained from J.T. Baker. Neocuproine hydrochloride monohydrate ($C_{14}H_{12}N_2•HCl•H_2O$, 99%) was obtained from Acros.. Iron standard solution (1.00 mg/L as Fe) was obtained from Hach Company. Molecular biology grade agarose was obtained from IBI Scientific (Peosta, IA). 0.5M Biotechnology grade EDTA pH 8.0 solution was obtained from AMRESCO. Deionized water (DI-H_2O) was obtained using an ELGA PURELAB Flex water purification system.

3.2.2 Characterization of MNPs

Dynamic Light Scattering (DLS) – Dynamic light scattering was used to measure the intensity-weighted size (hydrodynamic diameter) distribution. Measurements of each sample were taken in triplicate using a ZetaSizer Nano ZS90 sizing instrument (Malvern, Worcestshire, UK).

Transmission Electron Microscopy (TEM) – A Zeiss EM 10 TEM operating at a voltage of 60K was used to determine size distributions of MNPs. TEM samples were

prepared by placing a single drop of a MNP solution onto a carbon type B, 300 mesh grid. The grid was then placed in a petri dish and allowed to dry at ambient conditions. Size distributions were obtained using ImageJ software to size at least 500 particles from multiple TEM images taken of each sample.

Iron Content Assay – The iron content of MNP solutions was determined using a ferrozine assay. Briefly, a 200 µL dilution (typically 1:1000) of the MNP sample was obtained in combination with 1M HCl. 230 µL of $KMnO_4$/HCl was added to the sample and mixed via pipette. The $KMnO_4$/HCl solution was made by mixing equal volumes of 4.5% w/v $KMnO_4$ with 1.4M HCl. The mixture was then incubated for 2 hours at 60°C followed by a 10 minute cooling period. The sample was then mixed and transferred to a well plate via two 180 µL aliquots. 30 µL of prepared ferrozine solution was then added to the samples, mixed, and incubated at ambient conditions for 30 minutes. The prepared ferrozine solution was composed of 6.5mM ferrozine, 6.5mM neocuprine, 2.5M ammonium acetate, and 1M ascorbic acid dissolved in DI-H_2O. The absorbance of the samples at 550nm was then measured using a SpectraMax i3 plate reader (Molecular Devices, Sunnyvale, CA). Standard curves were created using an iron standard solution.

Magnetic Resonance Imaging– Relaxometry measurements were performed using a Siemens Verio Open-Bore 3T Scanner to determine the transverse proton relaxation times of solutions of iron oxide nanoparticles via spin-echo pulse sequences. For measurements of aqueous MNP solutions, samples were placed in either 0.6 mL or 1.6mL plastic microfuge tubes and the tubes were placed in a gridded layout and secured in a container. The tubes were submerged in water spiked with copper sulfate ($CuSO_4$) to control background noise.

3.2.3 Tissue Mimicking MRI Phantoms

A previously reported procedure for the production of tissue mimicking materials was used as the basis to create magnetic resonance imaging phantoms (D'Souza et al. 2001). To make 200 mL of tissue mimicking phantom solution, 100 mL of 18 M-Ω DI-H_2O, 7.9 mL *n*-propanol, and 2.0 g of dry agarose were first added to a beaker and then heated to 95°C in a water bath and mixed until the solution clears. Next, 0.2 g of thimerosal was dissolved in 100 mL of condensed milk (Eagle Family Foods, Inc., El Paso, TX). The agarose solution is then cooled to 55°C while the condensed milk is heated to the same temperature. The two solutions are then combined and mixed thoroughly. Lastly, 0.206 g of EDTA and 0.12 g of $CuCl_2 \cdot 2H_2O$ was added and the solution is again mixed until homogeneity is achieved. The solution was maintained above 45°C to prevent premature gelation. To form the solid tissue mimicking phantoms, the desired volume was pipetted from the heated mixture and transferred to a small volume microfuge tube and allowed to cool to room temperature. In the case of concentration studies, the MNP suspensions were added to the microfuge tubes first followed by the addition of the phantom solution. The solutions were then mixed quickly via pipetting and then allowed to cool to room temperature.

3.2.4 Formation of Concentration Gradient through MRI Phantoms

To demonstrate the ability to identify and characterize concentration gradients through the tissue mimicking phantoms for future size-dependent diffusion studies, a series of known concentration gradients were prepared and their relaxometric properties measured. These gradients were prepared in 1.6 mL centrifuge tubes by first injecting 0.5

mL of the phantom solution into a tube and allowing it to gel. Next, 33.33 µL of MNP solution of a known iron concentration and 66.67 µL of phantom solution were mixed and then injected on top of the previously gelled phantom in the microfuge tube and allowed to cool and gel. This was then repeated for each of the known concentrations to be used within the gradient. The samples were then characterized using the MRI scanner as detailed above. The transverse relaxation times T_2 throughout the phantom were then determined using the obtained R_2 map shown in Figure 3.2. The regions of interest to be characterized in each tube were chosen by selecting a central pixel in the region of the gradient and then extracting the data for a 13 pixel x17 pixel area, the equivalent of an approximate 7.63 mm x 7.95 mm area of the sample. The y-axis value was chosen based on the estimated depth of the gradient (7.62mm) that was determined by assuming each injected volume of the different concentrations resulted in a cylindrical geometry upon gelation. For the x-axis, the value of 7.95 mm was chosen so that the resulting area of interest would be approximately 1 mm from each side of the microtube in order to limit the influence of edge effects on the data. Mean R_2 values were obtained for each horizontal "slice" down the gradient by averaging the R_2 values at all x-positions for each y-position within the region of interest.
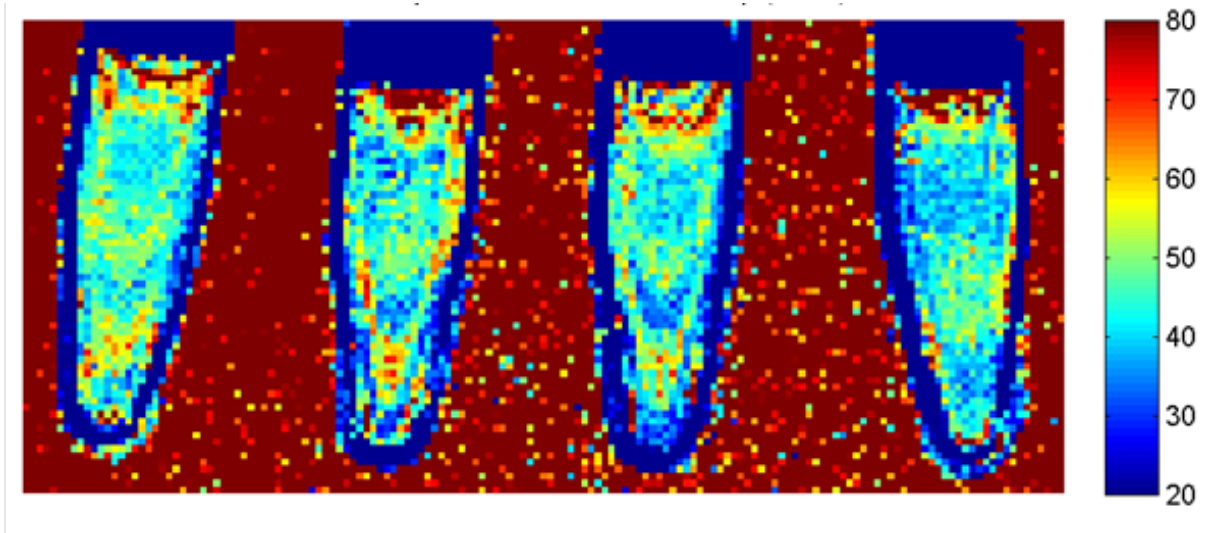
Figure 3.2 R_2 map for concentration gradients created using tissue mimicking phantom gels and known concentrations of MNP solutions. These gradients were produced using (from left to right) the MNP-O, MNP-96, MNP-124, and MNP-142 distributions. The units of the provided heat map are in s^{-1}.

3.3 Results and Discussion

3.3.1 Relaxometric Properties of "Original" MNPs

The relaxation times of the unseparated iron oxide nanoparticle solution were first determined in an aqueous suspension by creating a series of iron concentration dilutions in the range of 0.0-0.066 mg/mL. The inverse relaxation times R_2 for each sample were determined using a spin-echo sequence and then plotted as a function of iron weight concentration as shown in Figure 3.3b. A linear relationship (R^2 = 0.991) was found between the inverse relaxation time and iron concentration, which agrees well with previously reported data (Chertok et al. 2008). It was also determined that with the MRI sequence used, the relaxation time for the highest concentration of 0.066 mg/mL was too quick to be measured. Additionally, the resolution was too low to detect iron concentrations lower than 0.032×10^{-3} mg/mL and therefore the resulting relaxation times of these samples were found to be very similar to water. These results were then used to determine the range of iron concentrations to be used in subsequent relaxometry studies.
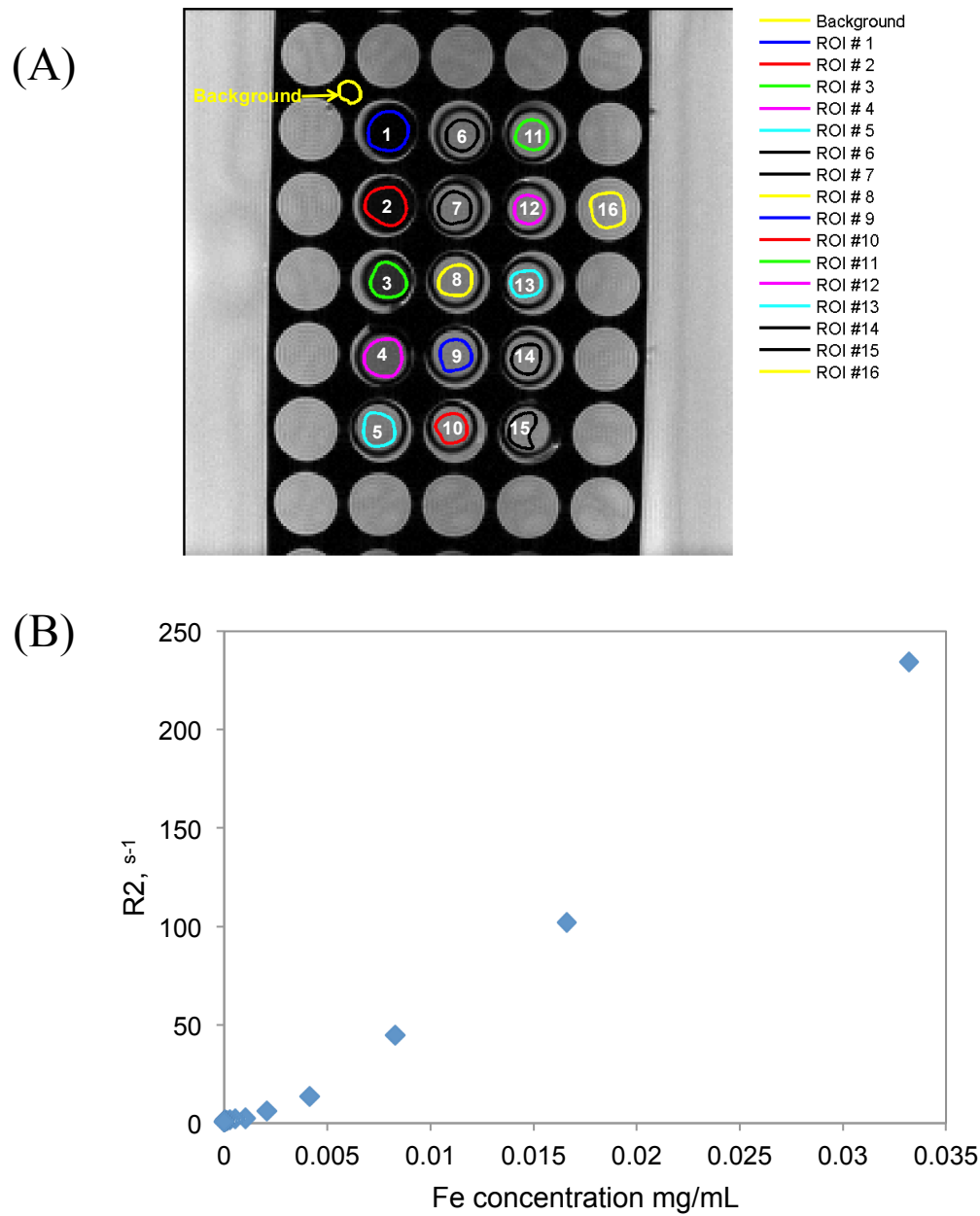
Figure 3.3 (A) Magnetic resonance image of a series of dilutions of the MNP-O distribution and (B) the measured transverse relaxivity R_2 values plotted with respect to iron concentration. A table of concentrations and corresponding R_2 values can be found in Appendix A.

3.3.2 Size Effect on the Relaxometric Properties of Aqueous Suspensions of MNPs

The effect of size on the transverse relxation time T2 of iron oxide nanoparticles in an aqueous suspension was studied using fractionated size distributions obtained by running the original MNP suspension through the MagCoil separator as detailed in the previous chapter. The hydrodynamic diameters of the obtained separations were measured by using DLS and the two distributions that were found to have the greatest difference in size, shown in Figure 3.4, were chosen to be used to illustrate the relationship between particle size and relaxation time. The two samples used, designated MNP-95 and MNP-151, possessed average sizes of 94.8 ± 7.7 nm and 151.2 ± 11.2 nm, respectively. A series of dilutions were made of each sample, as well as the original unseparated suspension (MNP-O), and the inverse relaxation times of each sample were determined using MRI.

Figure 3.5 shows that as the average hydrodynamic diameter of the MNPs increased, the transverse proton relaxation time also increased. Considering the inverse relaxation times at the highest concentration used, the R_2 values increased from 11.2 to 51.05 s^{-1} as the MNP size increased from 95 to 151 nm. This size-dependent behavior is similar to that previously reported for magnetic particles of hydrodynamic sizes less than 100 nm (Roca et al 2009). Additionally, it is interesting to note that the R_2 values of the MNP-O samples, which contains particles of the same size as both MNP-95 and MNP-151, as well as sizes between the two distributions, were consistenly between the R_2 values of MNP-95 and MNP-151. For example, the R_2 value for the MNP-O sample with an iron concentration of 0.009 mg/mL was determined to be 14.3 s^{-1} compared to the

values of MNP-95 and MNP-151 at the same concentration of 5.2 and 27.87 s^{-1}, respectively.

The relaxation times of each sample were determined by plotting the magnitude of the measured MR signal at each of the echo times used in the spin-echo sequence and using a curve-fitting MATLAB script. Using this approach normally produces data similar to that shown in Figure 3.6A, in which the signal magnitude decreases with increasing echo time. However, for the samples with an iron concentration of 0.0046 mg/mL and lower, an interesting behavior in the resulting signal vs. echo time curves was observed. Figure 3.6B shows that the signal initially increased with increasing echo time and then eventually began decreasing as the echo time continued to increase resulting a "hooking" pattern. In order to identify whether this phenomena was a result of the particle concentration or the MRI scanner, the scan was repeated using the same MNP suspensions and MRI sequence. Figure 3.7 shows repeating the scan successfully eliminated the "hooking" seen before while having negligible effect on the measured R_2 values, indicating that the behavior was most likely a result of the particles and not the MRI scanner. The source of this phenomena is unknown, however, and should be furthered explored in future studies.

Figure 3.4 Magnetic resonance image of a series of dilutions of the (A) MNP-95, (B) MNP-151 and (C) MNP-O distributions with their respective DLS measurements shown at the right. The iron concentration for each row is as follows: (1) 0.018, (2) 0.009, (3) 0.0046, (4) 0.0008, (5) 0.0004, (6) 0.0002, and (W) 0.00 mg/mL. A table of concentrations and corresponding R_2 values can be found in Appendix A.

Figure 3.5 Plot of the measured transverse relaxivity R_2 values for the MNP-95, MNP-151, and MNP-O distributions with respect to iron concentration.
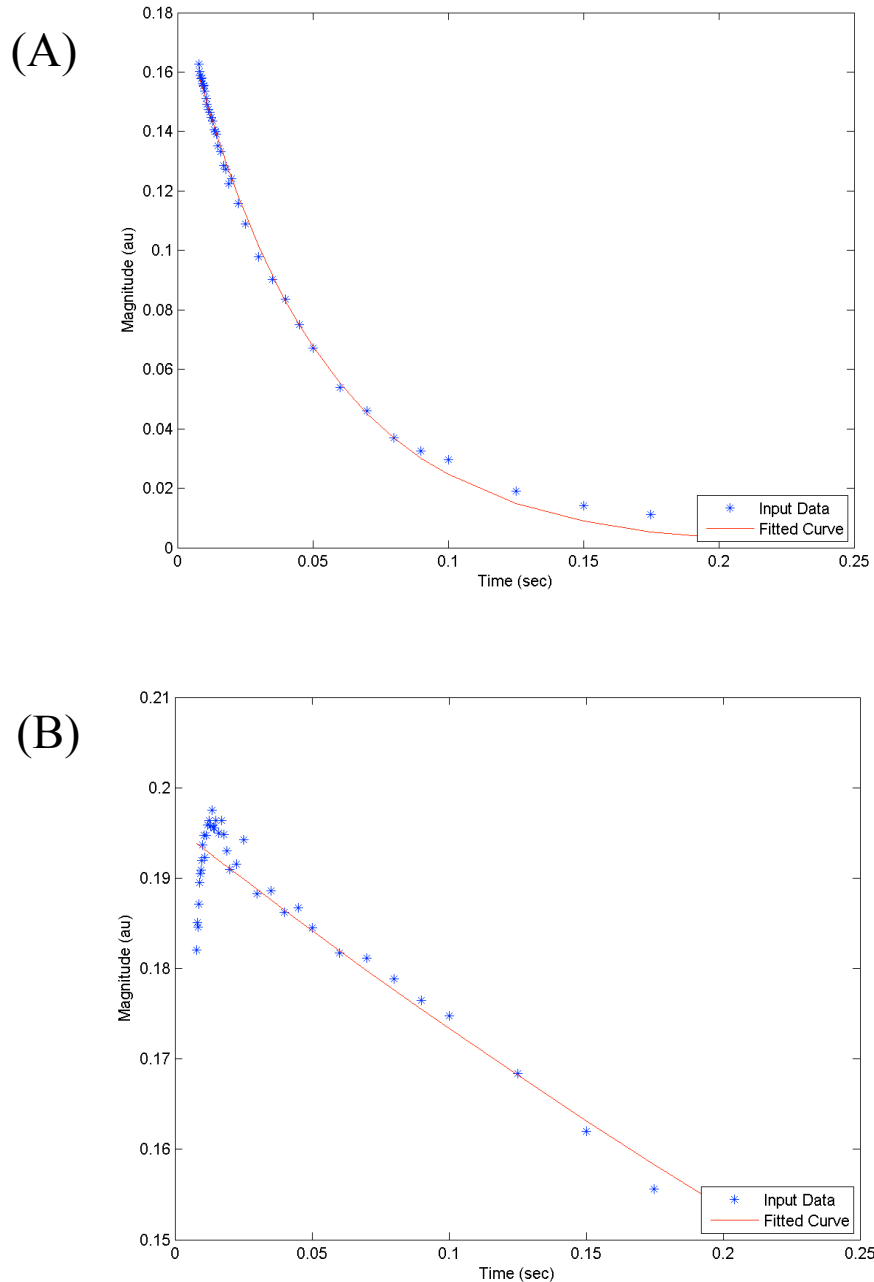
Figure 3.6 Magnetic resonance signal with respect to time for (A) higher concentration particle suspensions and (B) lower concentration particle suspensions illustrating the presence of the "hooking" behavior of the samples with lower iron content.
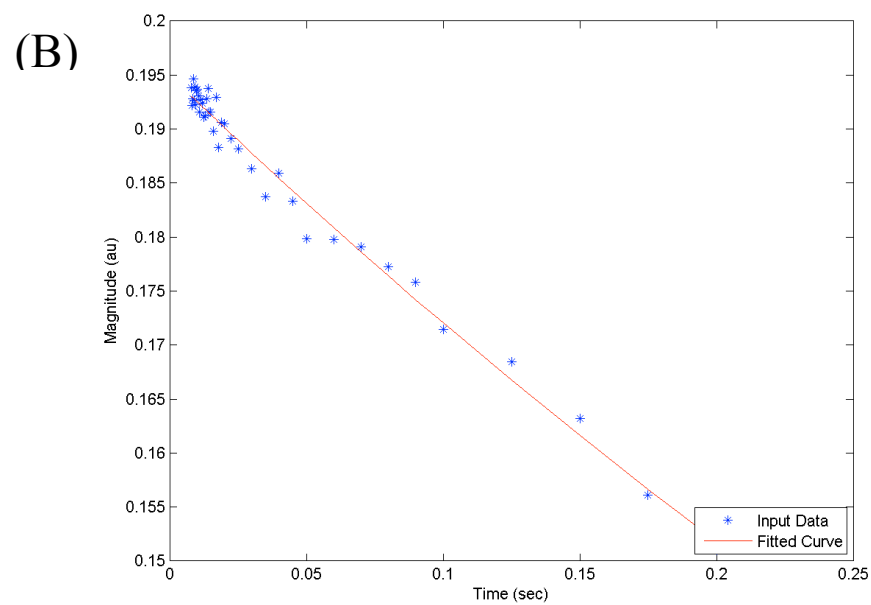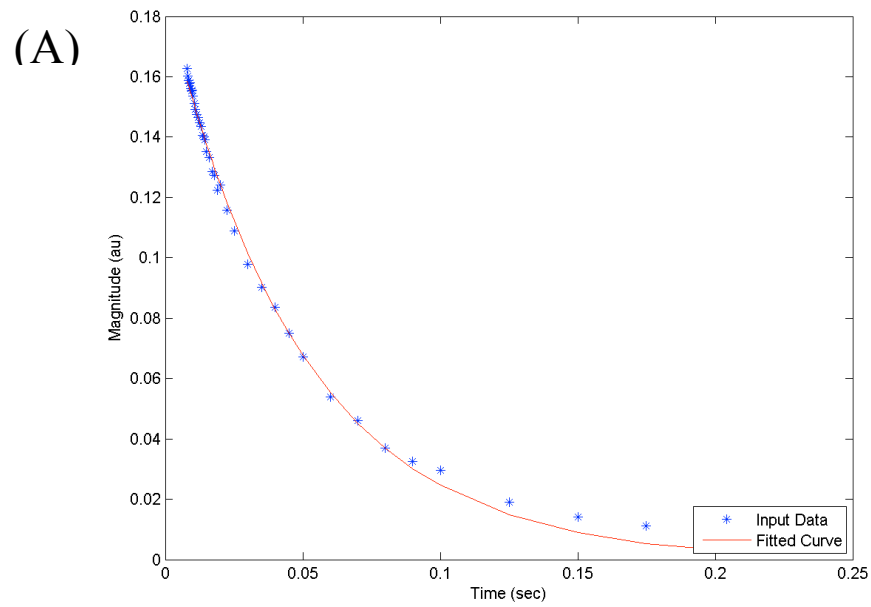
Figure 3.7 Magnetic resonance signal with respect to time for (A) higher concentration particle suspensions and (B) lower concentration particle suspensions for the MRI scan performed immediately following the one in which the "hooking" behavior was observed. Performing this second scan removed the presence of the abnormal behavior in the samples with lower iron content as seen in (B).
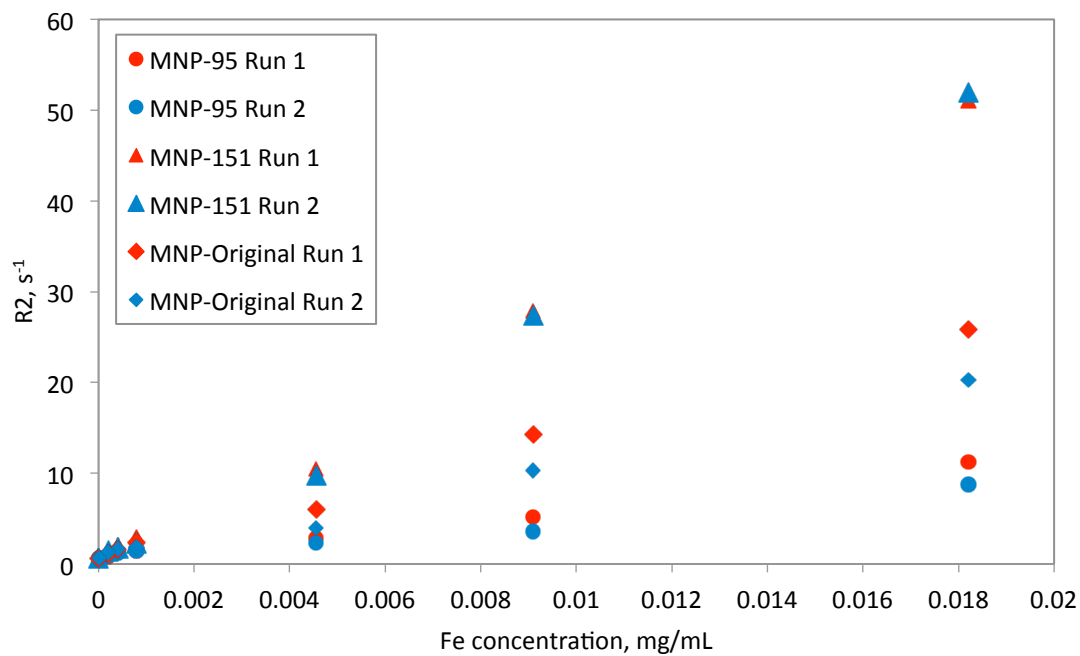
Figure 3.8 Comparison of the R_2 values measured for the run in which the "hooking" behavior was observed (Run 1) and the subsequent run in which the "hooking behavior was not detected (Run 2) showing that the elimination of the abnormal behavior had little effect on the measured relaxivities.

Despite the promising results from the initial studies, subsequent experiments produced conflicting data. Similar to before, distinct size distributions were obtained from MNP-O using the MagCoil. For this experiment, three size distributions were selected to be characterized as shown in Figure 3.9. The hydrodynamic diameters were measured using DLS and were found to be 96.3 ± 9.0, 123.6 ± 7.9, and 141.5 ± 10.8 nm for distributions MNP-96, MNP-124, and MNP-142, respectively. A series of dilutions in the range of 0.0-0.025 mg/ml was made for each distribution, including MNP-O, and the samples were scanned using MRI as seen in Figure 3.9.

Upon determination of each samples respective inverse relaxation time, the results were found to be considerably different from the first experiment despite using very similar size distributions and iron concentrations. Figure 3.10 shows that no single linear trend was observed for any of the distributions in the concentration range of 0.0-0.015 mg Fe/mL. These results conflict with the first experiment in which the R_2 values were shown to decrease in a linear fashion with decreasing concentrations in the range of 0.0-0.0182 mg Fe/mL. Additionally, when the R_2 values for each distribution were compared to one another, no trend was found with respect to size. For example, at a concentration of 0.015 mg Fe/mL, MNP-96 had the highest R_2 value of 148.0 s^{-1} and MNP-O had the lowest R_2 value at 125.1 s^{-1}, but for the samples at a concentration of 0.01 mg Fe/mL the highest R_2 value was that of MNP-142 at 76.0 s^{-1} while MNP-124 was found to have the lowest R value at 25.4 s^{-1}. The discrepancies between the two experiments could be the result of several possibilities including inconsistencies in the measurement of iron concentrations, MRI scan conditions, and the reduction of the MRI data. These

experiments should therefore be repeated to definitively identify the relationship between

size and relaxation times for particles of hydrodynamic diameters greater than 100 nm.
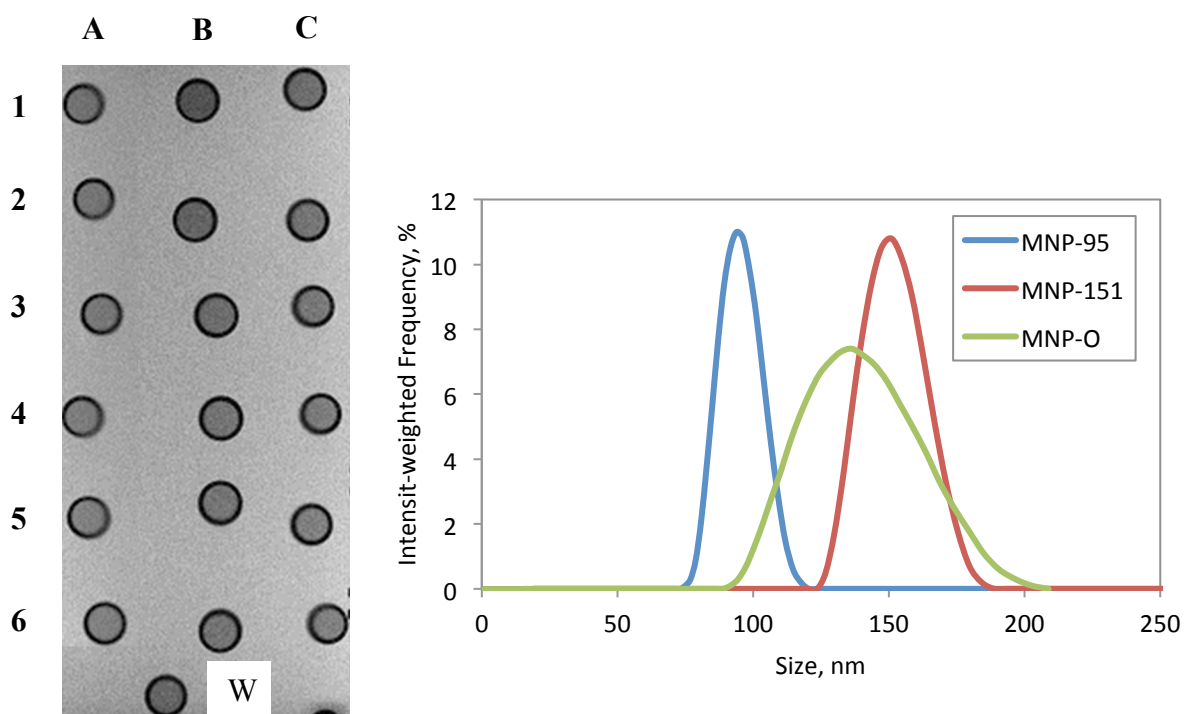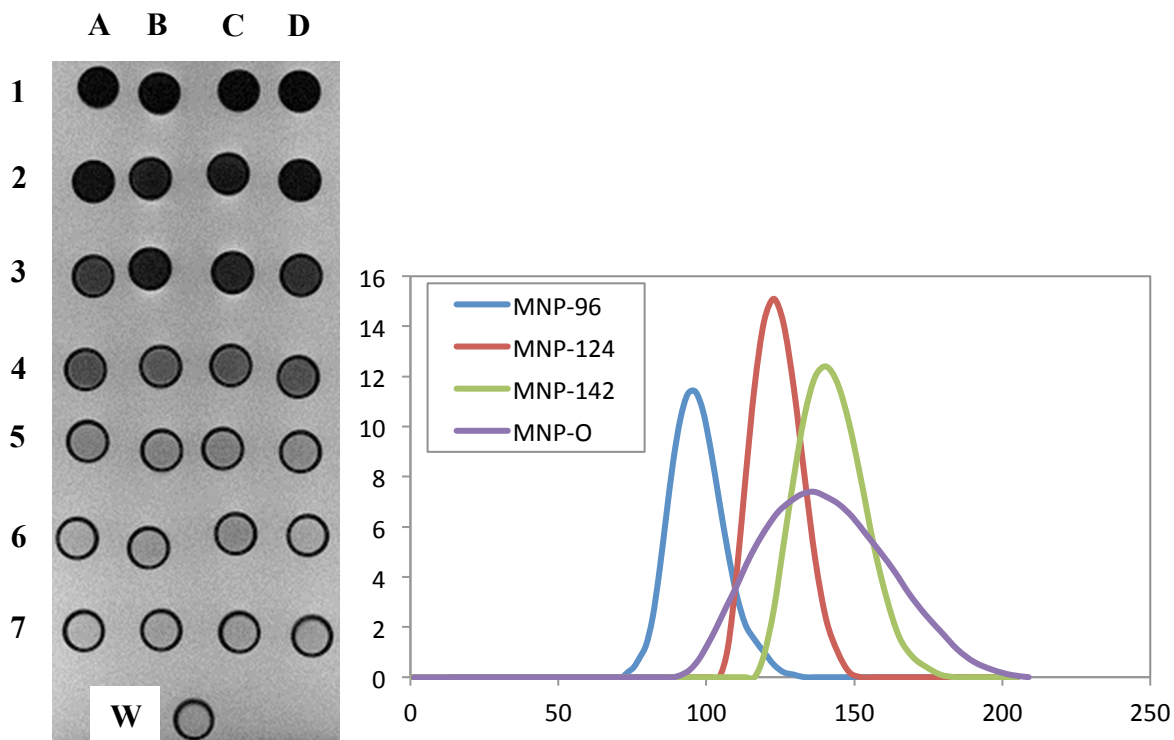
Figure 3.9 Magnetic resonance image of a series of dilutions of the (A) MNP-O, (B) MNP-96, (C) MNP-124, and (D) MNP-142 distributions with their respective DLS measurements shown at the right. The iron concentration for each row is as follows: (1) 0.025, (2) 0.020, (3) 0.015, (4) 0.010, (5) 0.005, (6) 0.0025, (7) 0.001, and (W) 0.00 mg/mL. A table of concentrations and corresponding R_2 values can be found in Appendix A.
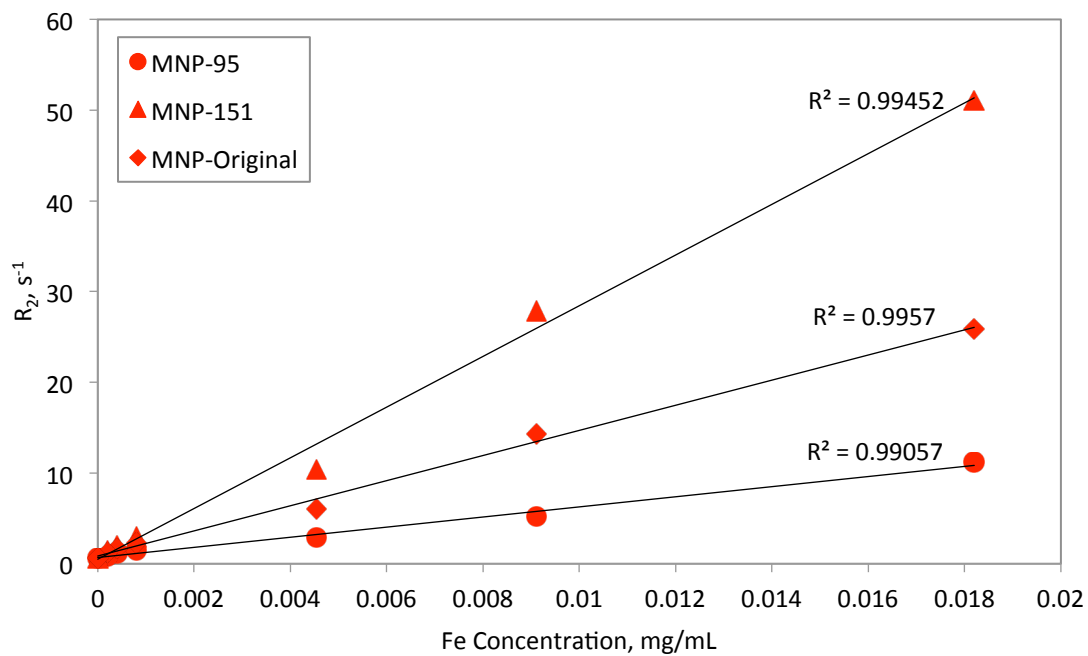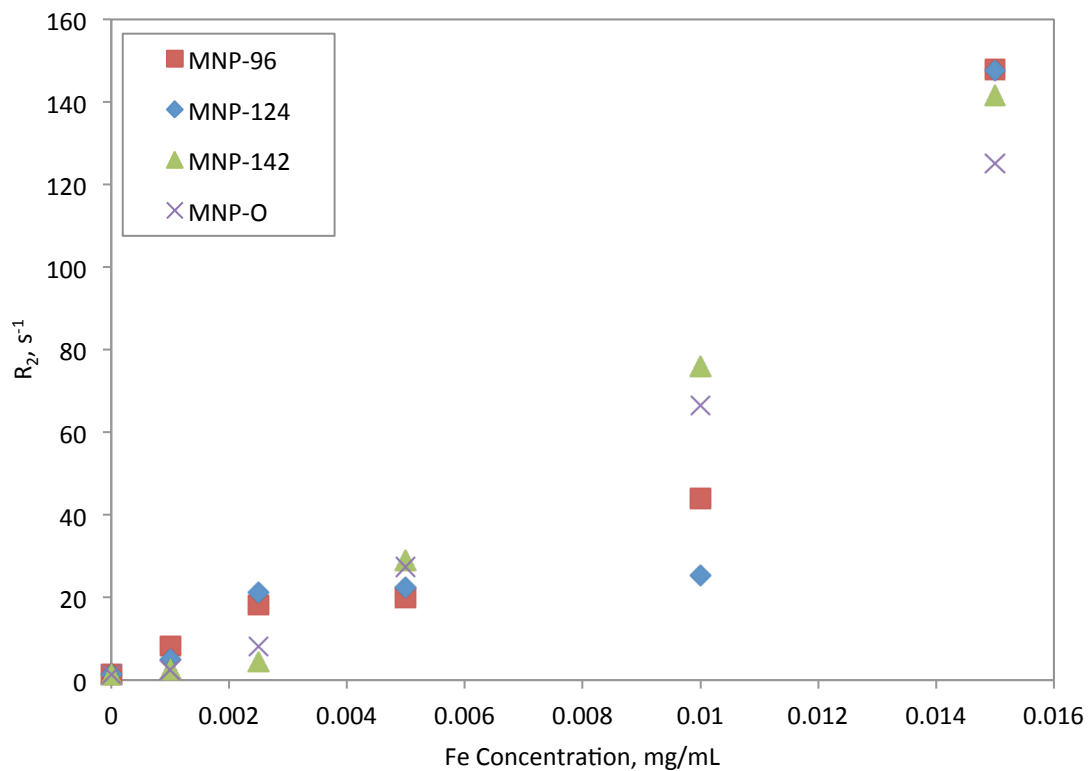
Figure 3.10 Transverse relaxivity R_2 values calculated for the imaged dilutions of the MNP-96, MNP-124, MNP-142, and MNP-O distributions.

3.3.3 Size Effect on Relaxometric Properties of MNPs in Tissue Mimicking Phantoms

While characterizing MNPs in aqueous suspensions allows for the determination of the relaxometric properties of the particles for research purposes, it is not truly reflective of the particles' imaging capabilities *in vivo*. Tissue mimicking phantom gels were therefore produced according to methods previously developed by D'Souza et al. for the purpose of optimizing the MNPs for use as MRI contrast agents. The gel solution was created according to the process outlined for the prostate mimicking material and then a series of MNP/gel mixtures were made with varying dilutions of the MNP-O suspension for MRI analysis as shown in Figure 3.11. A control mixture was included that did not include MNPs in order to characterize the properties of the phantom. The transverse relaxation time was found to decrease linearly with decreasing iron concentration as can be seen in Figure 3.11. The control phantom was found to possess an inverse relaxation time R_2 of 29.36 s^{-1}. Comparing this value to the values obtained by D'Souza et al., the relaxometric properties exhibited by the phantom gel made for this experiment are fairly close to the reported properties of the prostate mimicking materials ($R_2 = 22.57$ s^{-1}).
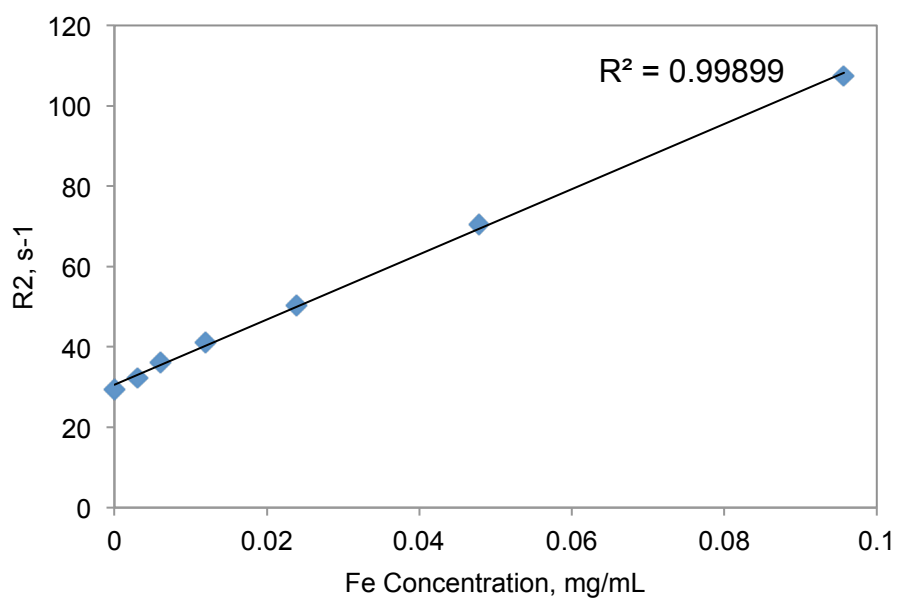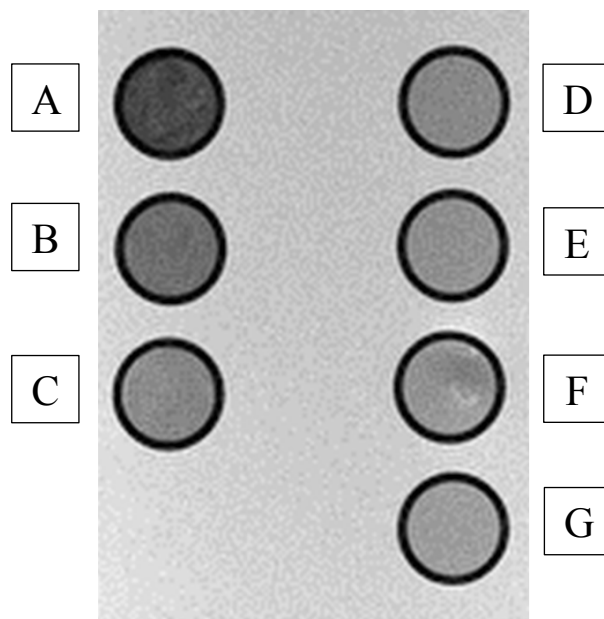
Figure 3.11 Magnetic resonance image of the series of dilutions made using the MNP-O distribution within the tissue mimicking phantoms and the corresponding R_2 values plotted with respect to iron concentration. The concentrations of the dilutions were (A) 0.096, (B) 0.048, (C) 0.024, (D) 0.012, (E) 0.006, (F) 0.003, and (G) 0.00 mg Fe/mL.

With the successful characterization of the prostate mimicking phantom, a series of MNP dilutions were made using the gel and the previously obtained MNP-96, MNP-124, MNP-142, and MNP-O distributions in order to analyze the size effect on relaxation times within tissue mimicking materials. Compared to the previous experiment, the measured R_2 value for the gel was found to be slightly higher (36.8 s^{-1} vs. 29.4 s^{-1}). Figure 3.12 shows that each distribution displayed a similar trend with decreasing iron concentration, as the R_2 values appear to decrease linearly with decreasing concentration from 0.015 mg Fe/mL to 0.005 mg Fe/mL. For the concentrations lower than 0.005 mg Fe/mL, however, it seems that the concentration of MNPs is too low to detect within the gel. This conflicts somewhat with the previous study in which concentrations down to 0.002 mg Fe/mL were detectable. Additionally, while the expected linear trend looks as if it begins for concentrations above 0.005 mg Fe/mL, comparing the R_2 values for each distribution at the concentrations in that range does not result in any trend with respect to size. For the samples with an iron concentration of 0.015 mg/mL, MNP-96 was found to have the highest R_2 value at 94.9 s^{-1} while MNP-O had the lowest at 73.9 s^{-1}. At 0.01 mg Fe/mL, MNP-142 had the highest R_2 value and MNP-124 had the lowest at 50.1 s^{-1}. This lack of trend is not surprising however, as the same aqueous suspensions of MNP-96, MNP-124, MNP-142, and MNP-O were used in both the aqueous suspension and phantom gel experiments. As before, this experiment should be repeated while ensuring the accuracy of the iron content determination.
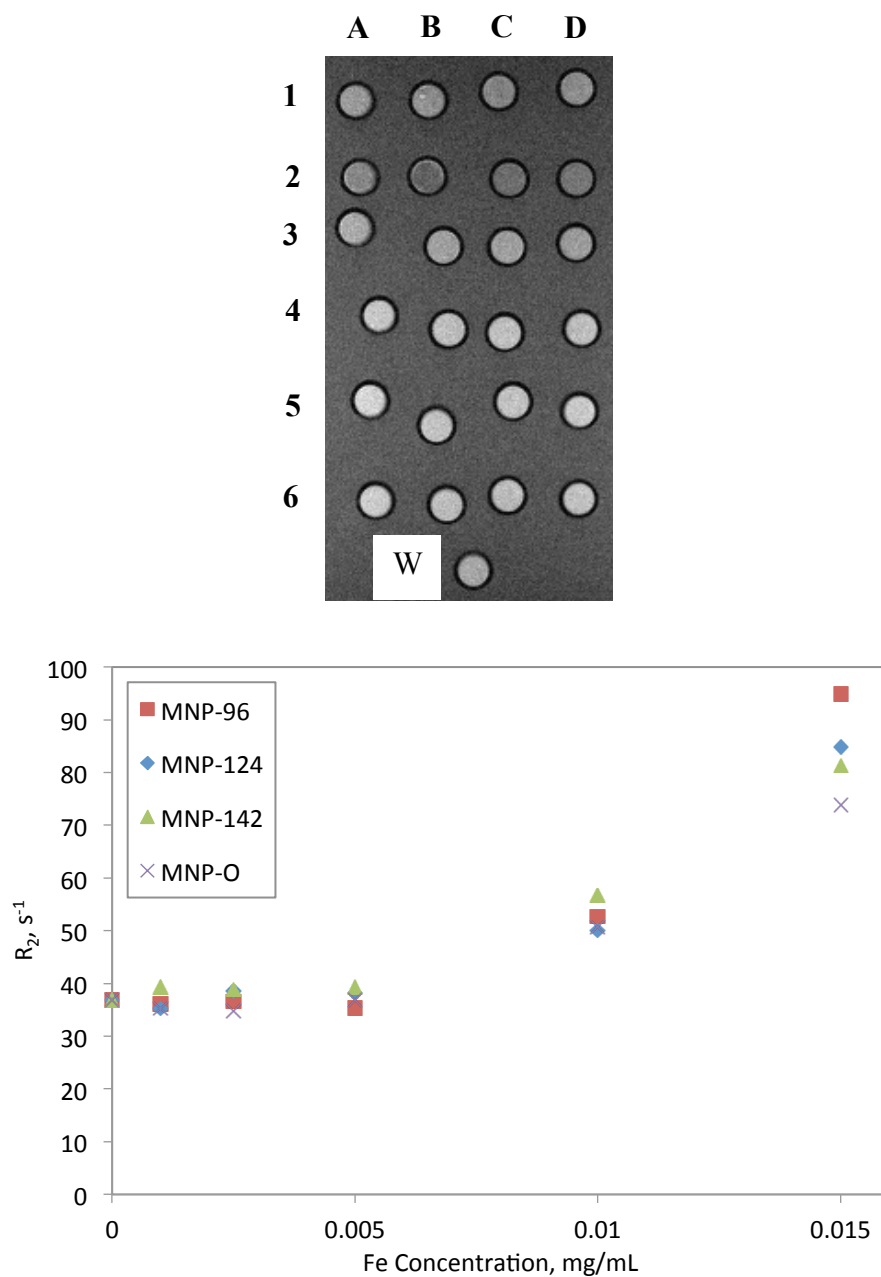
Figure 3.12 Transverse relaxivity R_2 values calculated plotted with respect to iron concentration for the imaged dilutions of the (A) MNP-O, (B) MNP-96, (C) MNP-124, and (D) MNP-142 distributions. The iron concentration for each row is as follows: (1) 0.020, (2) 0.015, (3) 0.010, (4) 0.005, (5) 0.0025, (6) 0.001, and (W) 0.00 mg/mL. A table of concentrations and corresponding R_2 values can be found in Appendix A.

3.3.4 Characterization of Artificial Diffusion Gradients

In preparation for future size-dependent diffusion studies, artificial diffusion gradients were produced in tissue mimicking phantom gels using known iron concentrations of the MNP-96, MNP-124, MNP-142, and MNP-O size distributions. The samples were scanned in the sagittal plane and an R_2 heat map was created as shown in Figure 3.14. From the selected regions of interest in each tube, a 5 pixel and 15 pixel average R_2 was determined for each position through the depth in the y-direction. Two different average R_2 values were calculated in order to determine the presence and magnitude of possible edge effects. Edge effects can occur near materials boundaries and can lead to erroneous relaxometric measurements depending on the quality of the scan's resolution (Babcock et al. 1985). The 5 pixel average was calculated from the 5 most centrally located pixels at each y-position in the region of interest while the 15 pixel average was calculated over the entire distance in the x-direction (15 pixels) at each y-position. The 5 pixel average reduces the chance of error due to edge effects by limiting the data to the center of each sample, but greatly reduces the data points used to calculate the mean. Conversely, the 15 pixel average utilizes the maximum amount of data points within the region of interest to calculate the mean but increases the chance of error due to edge effects. The values for each approach were plotted along with the expected R_2 values through the depth. The expected R_2 values were determined from controls of each concentration in the gradient for each size distribution that were also scanned along with the artificial gradients as shown in Figure 3.15. For each size distribution, the use of the 5 pixel average reduced the standard deviation for each data point, indicating that edge possible edge effects present in the 15 pixel average. In addition, the 5 pixel average

improved the agreeability between the calculated average R_2 and expected R_2 values for MNP-O, MNP-96, and MNP-142 samples.

All four samples appeared to exhibit the expected decreasing trend in R_2 values as the depth in the y-direction increased, although not in a step-wise manner as predicted based on the assumptions made for the expected R_2 values. This deviation from the expected behavior could be attributed to several sources. Firstly, it was assumed that each MNP/gel mixture that was injected formed a perfect cylinder within the tube upon gelation. However, it is more likely that a meniscus formed at the top of each liquid phantom mixture upon injection resulting in a warped cylindrical geometry for each layer. This line of thinking seems to be more accurate as evidenced by the curved appearance of the R_2 values in Figure 3.14A. Additionally, the MRI sequence used has not been optimized for the imaging of these gradients and therefore it is possible that more accurate data could be obtained by improving the resolution of the scans and increasing the number or positions through the sagittal plane in which the gradients are imaged. This experiment should be repeated in the future using an optimized MRI scan sequence and higher iron concentrations throughout the gradient to improve the resulting images and data. Despite the need to improve the experiment, it has been shown that gradients of different size distributions can be imaged and characterized using MRI which will allow for future experiments to be conducted to determine the effect of MNP size on diffusion through tissue mimicking materials.
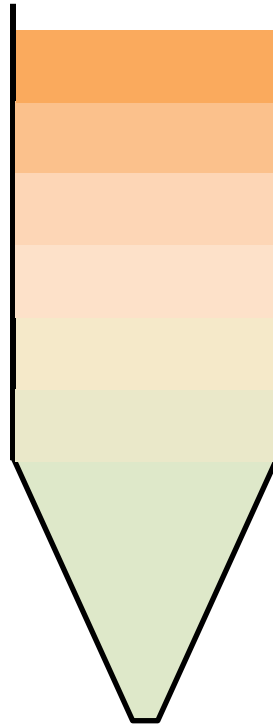
Figure 3.13 Illustration of the artificial diffusion gradient "slices" within a microfuge tube where the dark brown color indicates the highest concentration of nanoparticles and the pale green color represents the phantom gel with no nanoparticles present.
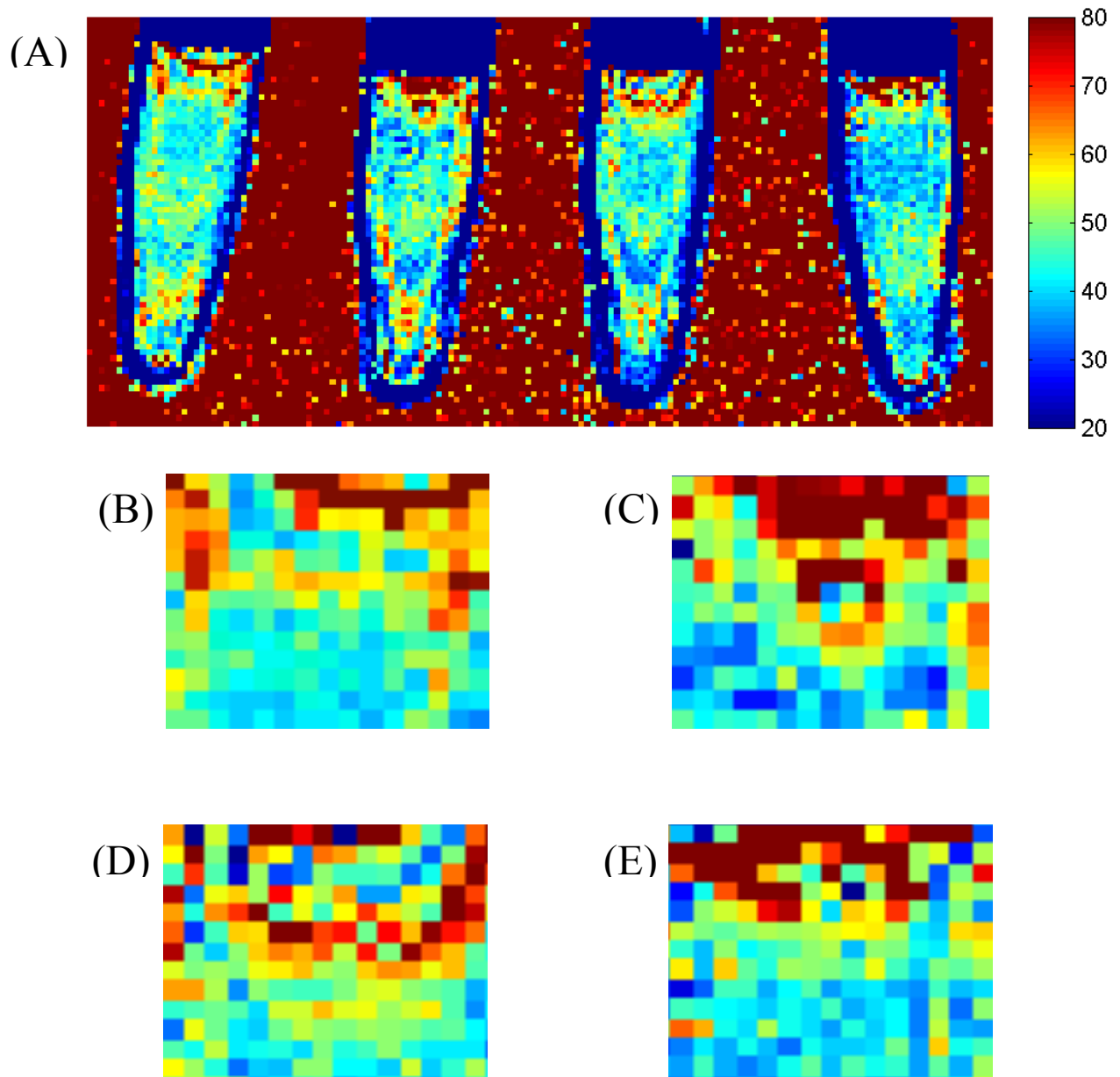
Figure 3.14 (A) R$_2$ map for concentration gradients created using tissue mimicking phantom gels and known concentrations of MNP solutions. From this map, a region of interest was isolated for (B) MNP-O, (C) MNP-96, (D) MNP-124, and MNP-142 for analysis.
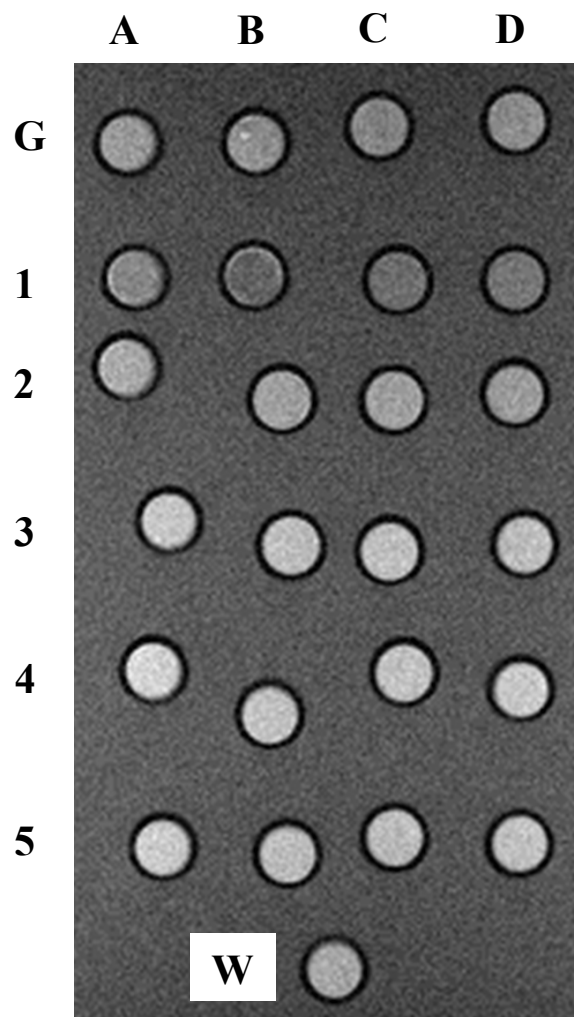
Figure 3.15 Magnetic resonance image used to calculate the expected R_2 values through the gradients for (A) MNP-O, (B) MNP-96, (C) MNP-124, and (D) MNP-142. The gradient samples created for each distribution are located in the top row and the subsequent rows are made of known dilutions of each distribution for the purpose of determining the R_2 at each known iron concentration. The iron concentration for each row is as follows: (1) 0.015, (2) 0.010, (3) 0.005, (4) 0.0025, (5) 0.001, and (W) 0.00 mg/mL. A table of concentrations and corresponding R_2 values can be found in Appendix A.
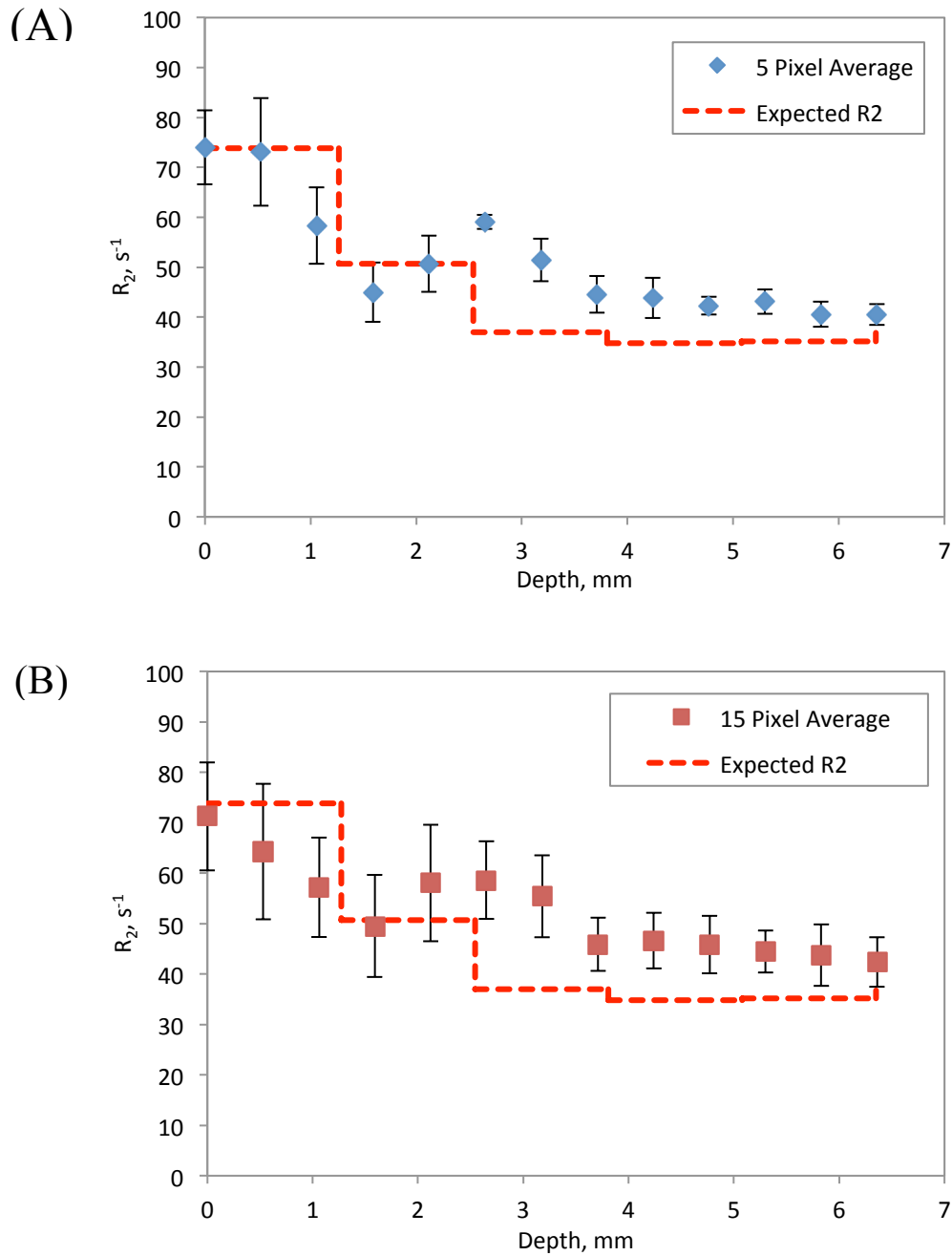
Figure 3.16 The transverse relaxivity R_2 measured through the depth of the artificial gradient using (A) a 5 pixel average and (B) a 15 pixel average at each y-position compared to the expected R_2 values for the MNP-O distribution. Error bars indicate standard deviation for each calculated R_2 value.
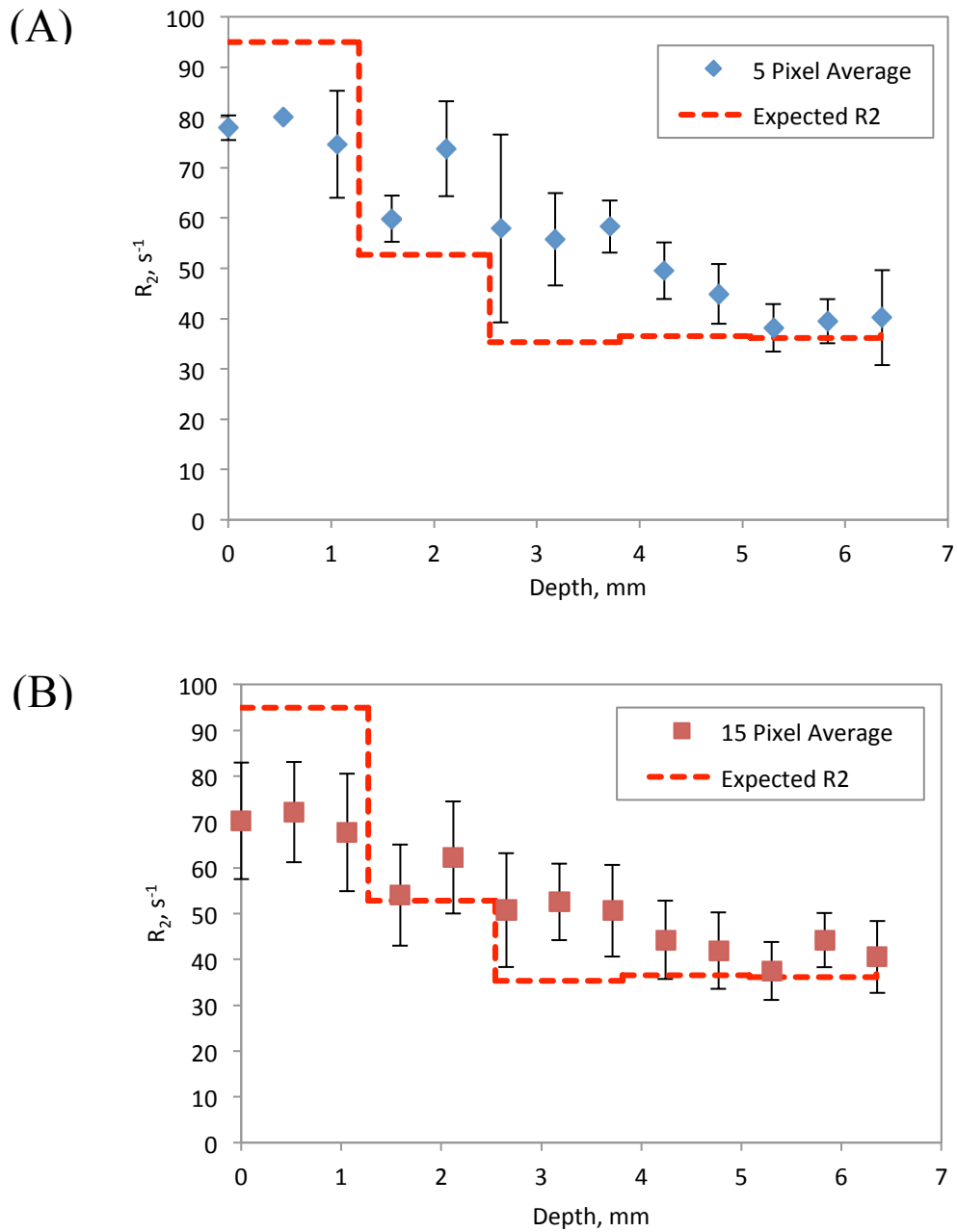
Figure 3.17 The transverse relaxivity R_2 measured through the depth of the artificial gradient using (A) a 5 pixel average and (B) a 15 pixel average at each y-position compared to the expected R_2 values for the MNP-96 distribution. Error bars indicate standard deviation for each calculated R_2 value.
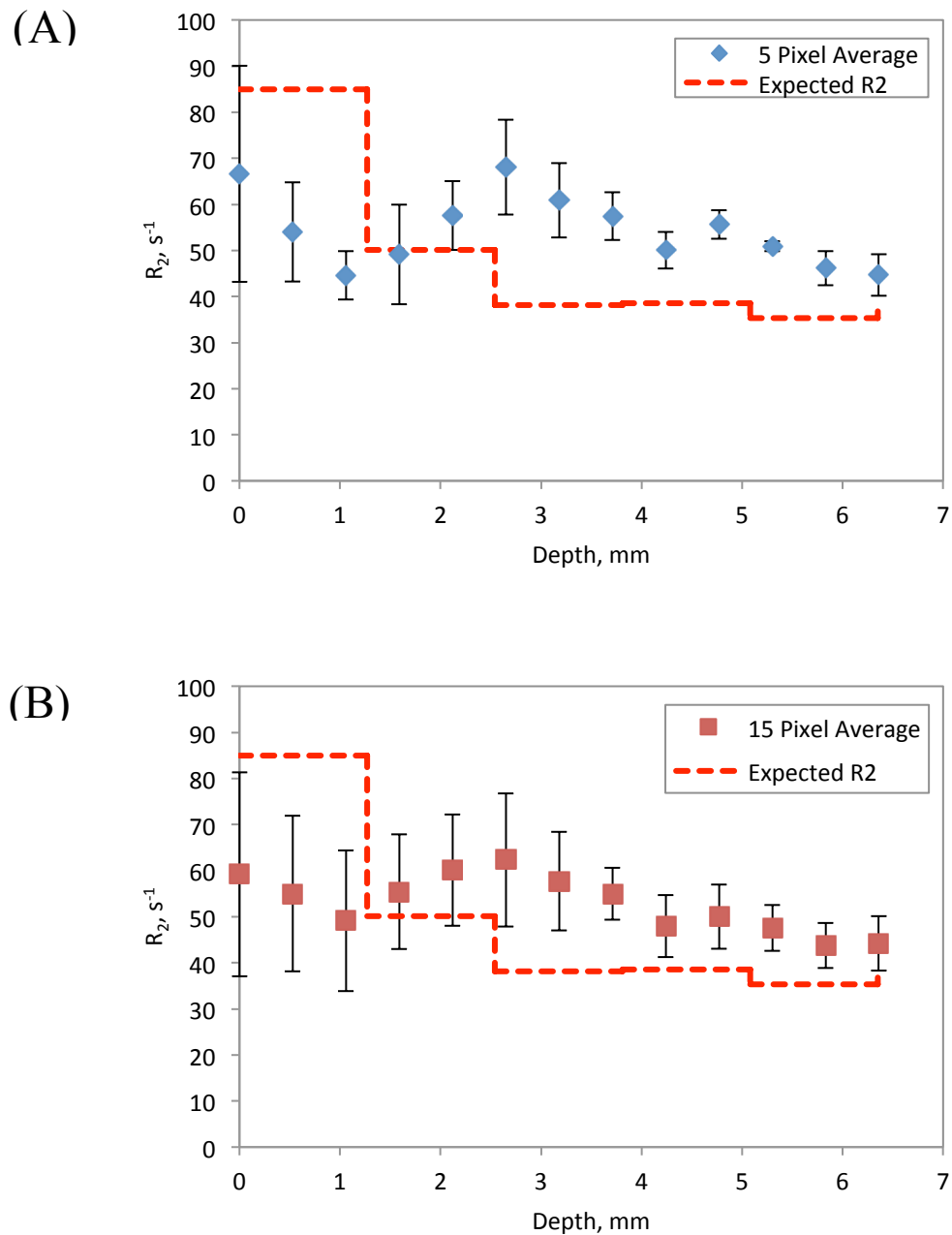
Figure 3.18 The transverse relaxivity R_2 measured through the depth of the artificial gradient using (A) a 5 pixel average and (B) a 15 pixel average at each y-position compared to the expected R_2 values for the MNP-124 distribution. Error bars indicate standard deviation for each calculated R_2 value.
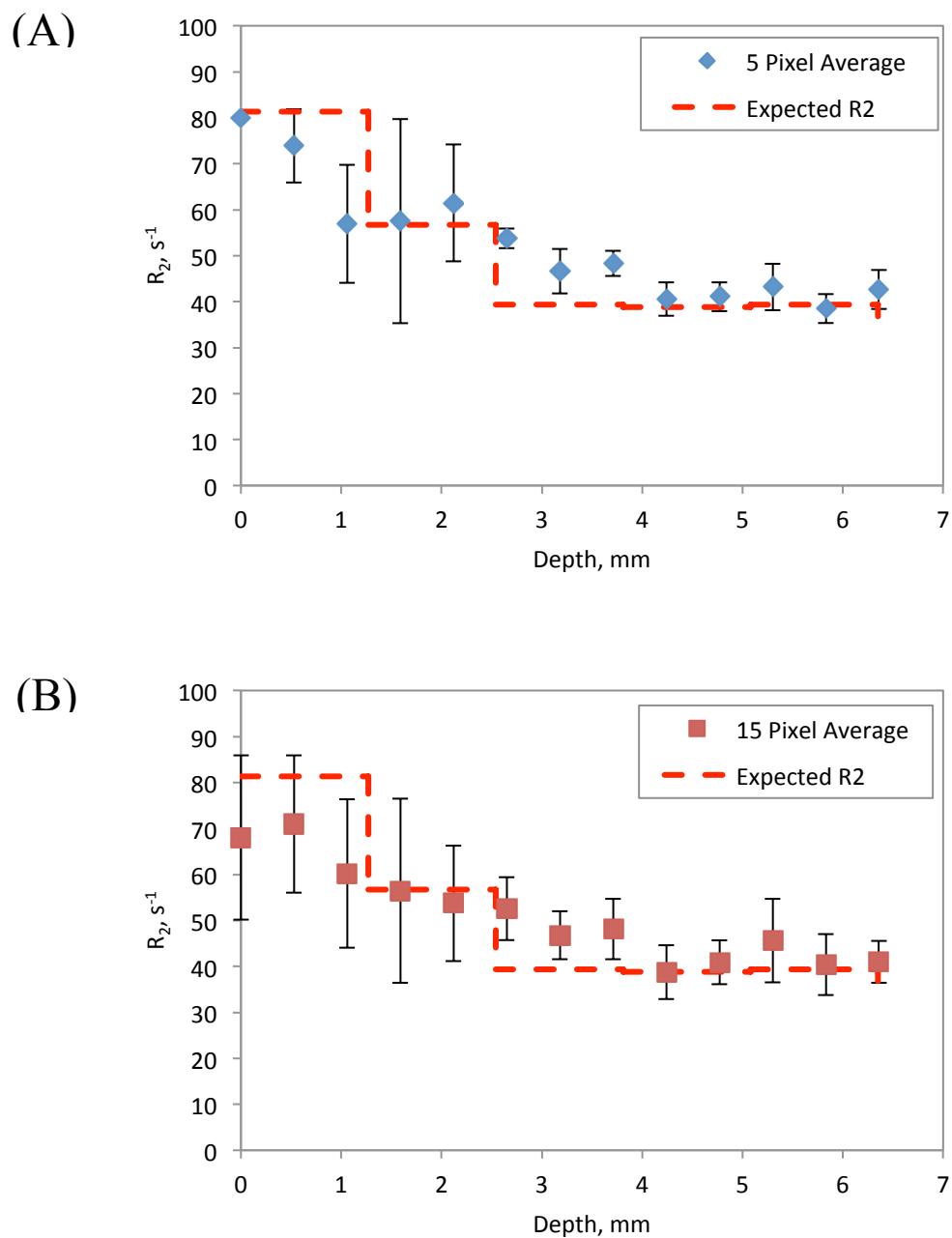
Figure 3.19 The transverse relaxivity R_2 measured through the depth of the artificial gradient using (A) a 5 pixel average and (B) a 15 pixel average at each y-position compared to the expected R_2 values for the MNP-142 distribution. Error bars indicate standard deviation for each calculated R_2 value.

3.4 Conclusions

It has been previously reported for magnetic nanoparticles with hydrodynamic diameters less than 100 nm that the transverse relaxivity R_2 is a size-dependent property (Roca et al. 2008). In this chapter, iron oxide nanoparticles of different sizes obtained using the methods detailed in Chapter 2 were used in a series of MRI studies to investigate the relationship between size and R_2 values for particles possessing hydrodynamic diameters above 100 nm. While initial results indicated that the previously reported size dependency held true for particles of larger size, subsequent experiments, in both aqueous and phantom suspensions, provided conflicting results. The experiments detailed here should be repeated in future studies to correctly establish the effect of size on the transverse relaxivity for the size range investigated. Additionally, a preliminary study was conducted in which artificial diffusion gradients were created using tissue mimicking MRI phantoms and different size distributions of iron oxide nanoparticles. The results of this study illustrated the ability to identify concentration gradients of magnetic nanoparticles within the tissue mimicking gels by analysis of the transverse relaxivity values through the depth of the gel. This ability will be of critical importance for *in vitro* size-dependent diffusion studies to be conducted in the near future.

Chapter 4

Overall Conclusions and Future Directions

Nanomedicine is a rapidly growing field that could provide solutions to some of the biggest problems in medicine including improved accuracy of diagnosis and more effective therapies for diseases such as cancer. However, a lack of thorough understanding on the effect of the physical and chemical properties of nanomaterials on biological systems greatly hinders development of optimal nanomedicine technologies. A good example of this issue can be found in the case of iron oxide nanoparticles used as contrast agents and magnetically targeted therapies. While iron oxide nanoparticles possess attractive properties for these types of applications, such as superparamagnetism, the inability to synthesize them in a monodisperse manner makes it difficult to identify optimal size ranges for different applications. It has been shown previously that the size of these particles has a direct effect on their magnetic properties, in vivo biodistribution and clearance, and their effectiveness as contrast agents for MRI. It is clear that methods are needed that enable size effect studies research to be conducted by producing monodisperse distributions of iron oxide nanoparticles. The research detailed within this thesis presents a solution to the issue of creating monodisperse distributions of iron oxide nanoparticles for biomedical applications as well as preliminary studies that sought to investigate the effect of nanoparticles size on their relaxometric properties when used in magnetic resonance imaging.

In Chapter 2, the development of a novel system for the size-selective separation of magnetic nanoparticles using a form of field-flow fractionation is detailed. Using this system, an original polydisperse suspension of magnetic nanoparticles was size-selectively separated into a series more distinct size distributions by applying varying drag forces to nanoparticles in a constant magnetic field gradient. This technique was then used to obtain differently sized particles that were then used in MRI experiments in an attempt to determine how size affects the relaxometric properties of particles above 100 nm in diameter, as presented in Chapter 3. Initial results indicated that the inverse relaxivity R2 was a size-dependent property that decreased with decreasing particle size. However, when this experiment was repeated using similarly size distributions, no correlation was found between nanoparticle size and R2 values thus demonstrating the need for additional studies in the future to correctly identify any trend that may occur. Additionally, the ability to characterize artificial diffusion gradients using MRI was demonstrated for the purpose of future size-dependent diffusion studies.

The results of the research presented here reveal that the post-synthesis size-selective separation of polydisperse magnetic nanoparticles is possible. This is an important development in terms of nanomedicine optimization as this novel system will allow future studies to be conducted in order to establish a fundamental understanding of the effect of magnetic nanoparticle particle size on their physical properties and interactions with biological systems. It is believed that the current state of design for the proposed system can be further improved to make it a more scalable and effective process. The underlying mechanism of the field-flow fractionation process is currently being applied to a new design in which magnetic beads within a column are used to

separate larger volumes of nanoparticle suspension by size as shown in Figure 4.1. The ability to apply the developed techniques to such a setup would greatly increase the scalability of the system. Future work will include characterizing the effectiveness of the new setup compared to the current MagCoil and investigating the effect of utilizing a variable electromagnet as opposed to the solid neodymium magnets currently used. Furthermore, the current approach to size separation will be used to conduct various *in vitro* and *in vivo* experiments in order to study the effect of particle size on such properties as diffusion into tumor-like tissues compared to healthy tissue, R_2 when used as contrast agents, and *in vivo* biodistribution and pharmacokinetics. It is hoped that the further development and improvement of these size-selective separation techniques will enable the optimization of magnetic nanoparticles according to their specific application.

Figure 4.1 Digital image of the proposed magnetic field-flow fractionation device composed of a column packed with magnetic beads.

References

Albanese, A., Tang, P.S., & Chan, W.C.W., 2012. The Effect of Nanoparticle Size, Shape, and Surface Chemistry on Biological Systems. *Annual Review of Biomedical Engineering*, 14, pp.1-16.

Babcock, E.E., Brateman, L., Weinreb, J.C., Horner, S.D., & Nunally, R.L., 1985. Edge Artifacts in MR Images: Chemical Shift Effect. *Journal of Computed Assisted Tomography*, 9:2, 252-57.

Bautista, M.C., Bomati-Miguel, O., del Puerto Morales, M., Serna, C.J., & Veintemillas-Verdaguer, S., 2005. Surface characterization of dextran-coated iron oxide nanoparticles prepared by laser pyrolysis and coprecipitation. *journal of Magnetism and Magnetic Materials*, 292:1, pp. 20-27.

Berg, H.C., 1993. Random Walks in Biology. Princeton, NJ: Princeton University Press. pp11-12.

Beveridge, J.S., Stephens, J.R., Latham, A.H., & Williams, M.E., 2009. Differential Magnetic Catch and Release: Analysis and Separation of Magnetic Nanoparticles. *Analytical Chemistry*, 81(23), pp.9618-24.

Beveridge, J.S., Stephens, J.R., & M.E. Williams, 2011. Differential magnetic catch and release: experimental parameters for controlled separation of magnetic nanoparticles. *Analyst*, 136, 2564-71.

Bird, R.B., Stewart, W.E., & Lightfoot, E.N., 1963. Transport Phenomena. New York: Wiley, pp.59-60.

Becker, E.D. 1980. High Resolution NMR: Theory and Chemical Applications. New York: Academic Press. pp. 13-15.

Berret, J., Schonbeck, N., Gazeau, F., Kharrat, D.E., Sandre, O., Vacher, A., & Airiau, M., 2006. Controlled Clustering of Superparamagnetic Nanoparticles Using Block Copolymers: Design of New Contrast Agents for Magnetic Resonance Imaging. *Journal of the American Chemical Society*, 128, pp.1755-61.

Beveridge, J.S., Stephens, J.R., Latham, A.H., & Williams, M.E., 2009. Differential Magnetic Catch and Release: Analysis and Separation of Magnetic Nanoparticles. *Analytical Chemistry*, 81(23), pp.9618-624.

Bitounis, D., Fanciullino, R., Iliadis, A., & Ciccolini, J., 2011. Optimizing Druggability through Liposomal Formulations: New Approaches to an Old Concept. *ISRN Pharmaceutics*, Vol. 2012, Article ID 738432, pp. 1-11.

Burda, C., Chen, X., Narayanan, R., & El-Sayed, M.A., 2005. Chemistry and Properties of Nanocrystals of Different Shapes. *Chemical Reviews*, 105:4, pp. 1025-92.

Bulte, J.W., Ma, L.D., Magin, R.L., Kamman, R.L., Hulstaert, C.E., Go, K.G., & Leij, LD., 1993. Selective MR imaging of labeled human peripheral blood mononuclear cells by liposome mediated incorporation of dextran-magnetite particles. *Magnetic Resonance in Medicine*, 29:1, pp. 32-27.

Bulte, J.W.M., de Cuyper, M., Despres, D., & Frank, J.A., 1999. Preparation, relaxometry, and biokinetics of Pegylated magnetoliposomes as MR contrast agent. *Journal of Magnetism and Magnetic Materials*, 194, pp. 204-09.

Byrne, J., Betancourt, T., & Brannonpeppas, L., 2008. Active Targeting Schemes for Nanoparticle Systems in Cancer Therapeutics. Advanced Drug Delivery Reviews 60(15), pp.1615-26.

Carpino, F., Moore, L.R., Zborowski, M., Chalmers, J.J., Williams, P.S., 2005. Analysis of magnetic nanoparticles using quadrupole magnetic field-flow fractionation. *Journal of Magnetism and Magnetic Materials*, 293, pp.546-52.

Chertok, B., Moffat, B.A., David, A.E., Yu, F., Bergemann, C., Ross, B.D., & Yang, V.C., 2007. Iron oxide nanoparticles as a drug delivery vehicle for MRi monitored magnetic targeting of brain tumors. *Biomaterials*, 29, pp. 487-96.

Choi, H.S., Liu, W., Misra, P., Tanaka, E., Zimmer, J.P., Ipe, B.I., Bawendi, M.G., & Frangioni, J.V., 2007. Renal clearance of quantum dots. *Nature Biotechnology*, 25, pp.1165-70.

Chouly, C., Pouliquen, D., Lucet, I., Jeune, J., & Jallet, P., 1996. Developemtn of Superparamagnetic nanoparticles for MRI: the effect of particle size, charge, and surface nature on biodistribution. *Journal of Microencapsulation*, 13(3), pp.245-55.

Clift, M.J.D., Rothen-Rutishauser, B., Brown, D.M., Duffin, R., Donaldson, K., Proudfoot, L., Guy, K., & Stone, V., 2008. The impact of different nanoparticle surface chemistry and size on uptake and toxicity in a murine macrophage cell line. *Toxicology and Applied Pharmacology*, 232, pp.418-27.

Cole, A.J., David, A.E., Wang, J., Galban, C.J., Hill, H.L., & Yang, V.C., 2010. Polyethylene glycol modified, cross-linked starch-coated iron oxide nanoparticles for enhanced magnetic tumor targeting. *Biomaterials*, 32, pp.2183-2193.

Cole, A.J., Yang, V.C., & David, A.E., 2011. Cancer Theranostics: The Rise of Targeted Magnetic Nanoparticles. *Trends in Biotechnology*, 29, pp.323–332.

Corot, C., Robert, P., Idee, J., & Port, M., 2006. Recent Advances in Iron Oxide Nanocrystal Technology for Medical Imaging. *Advanced Drug Delivery Reviews* 58(14), pp.1471-1504.

Dessai, M.M., Gee, M.S., Harisinghani, M.G., Tabatabaei, S., 2009. Molecular Imaging in Urologic Surgery. *Urologic Clinics of North America*, 36(2), pp. 125-132.

Doane, T.L., & Burda, C., 2011. The unique role of nanoparticles in nanomedicine: imaging, drug delivery and therapy. *Chemical Society Reviews*, 41, pp. 2885-911.

Dobrovolskaia, M.A., Aggarwalk, P., Hall, J.B., McNeil, S.E., 2008. Preclinical Studies to Understand Nanoparticle Interaction with the Immune System and Its Potential Effects on Nanoparticle Biodistribution. *Molecular Pharmaceutics*, 5(4), pp.487-95.

D'Souza, W.D., Madsen, E.L., Unal, O., Vigen, K.K., Frank, G.R., & Thomadsen, B.R., 2001. Tissue mimicking materials for a multi-imaging modality prostate phantom. *Medical Physics*, 28:4, pp.688-700.

Duan, H., Kuang, M., Wang, X., Wang, Y.A., Mao, H., & Nie, S., 2008. Reexamning the Effects of Particle Size and Surface Chemistry on the Magnetic Properties of Iron Oxide Nanocrystals: New Insights into Spin Disorder and Proton Relaxivity. *The Journal of Physical Chemistry Letters C*, 112, pp. 8127-31.

Farokhzad, O.C., 2004. Nanoparticle-Aptamer Bioconjugates: A New Approach for Targeting Prostate Cancer Cells. *Cancer Research* 64(21), pp.7668-672.

Filler, A.G., 2009. The history, development and impact of computed imaging in neurological diagnosis and neurosurgery: CT, MRI, and DTI. *Nature Precedings*, 7(1), pp. 1-69.

Freitas Jr., R.A., 1999. Nanomedicine, Volume I: Basic Capabilities. Landes Bioscience.

Gonzales, M., & Krishnan, K.M., 2005. Synthesis of magnetoliposomes with monodisperse iron oxide nanocrystals cores for hyperthermia. *Journal of Magnetism and Magnetic Materials*, 293:1, pp. 265-70.

Gupta, A.K. and Gupta, M., 2004. Synthesis and Surface Engineering of Iron Oxide Nanoparticles for Biomedical Applications. *Biomaterials*, 26, 3995-4021.

Hillaireau, H, & Couvreur, P., 2009. Nanocarriers' entry into the cell: relevance to drug delivery. *Cellular and Molecular Life Sciences*, 66(17), pp.2873-896.

IMV Medical Information Division, Inc. IMV Benchmark Report MR. 2012.

Jager, G.J., Ruijter, E.T., Kaa, C., la Rosette, J.J., Oosterhof, G.O., Thornbury, J.R., & Barentsz, J.O., 1996. Local Staging of Prostate Cancer with Endorectal MR Imaging: Correlation with Histopathology. *American Journal of Roentgenology,* 166, pp.845–52.

Jeon, S.I., Lee, J.H., Andrade, J.D., & De Gennes, P.G., 1991. Protein-surface interactions in the presence of polyethylene oxide: I. simplified theory. *Journal of Colloid and Interface Science*, 142(1), pp.149-58.

Johannsen, M., Gneveckow, U., Thiesen, B., Taymoorian, K., Cho, C., N. Waldofner, R. Scholz, A. Jordan, S. Loening, and P. Wust. "Thermotherapy of Prostate Cancer Using Magnetic

Nanoparticles: Feasibility, Imaging, and Three-Dimensional Temperature Distribution." *European Urology* 52.6 (2007): 1653-662.

Jolivet, J.P., Belleville, E.T., & Livage J., 1992. Influence of Fe(II) on the Formation of the Spinel Iron Oxide in Alkaline Medium. *Clays and Clay Minerals*, 40:5, pp. 531-39.

Jun, Y., Huh, Y., Choi, J., Lee, J., Song, H., Kim, S., Yoon, S., Kim, K., Shin., J., Suh, J., & Cheon, J., 2005. Nanoscale Size Effect of Magnetic Nanocrystals and Their Utilization for Cancer Diagnosis via Magnetic Resonance Imaging. *Journal of the American Chemical Society*, 127, 5732-33.

Jun, Y., Lee, J., & Cheon, J., 2007. Nanoparticle Contrast Agents for Molecular Magnetic Resonance Imaging. *Nanobiotechnology II: More Concepts and Applications*, Wiley-VCH Verlag GmBH & Co. KGaA, Weinheim, Germany.

Kettiger, H., Schipanski, A., Wick, P., & Huwyler, J., 2013. Engineered nanomaterial uptake and tissue distribution: from cell to organism. *International Journal of Nanomedicine*, 2013(8), pp. 3255-269.

Kim, B.H., Nohyun, L., Kim, H., An, K., Park, Y.I., Choi, Y., Shin, K., Lee, Y., Kwon, S.G., Na, H.B., Park, J., Ahn, T., Kim, Y.W., Moon, W.K., Choi, S.H., & Hyeon, T., 2011. Large-Scale Synthesis of Uniform and Extremely Small-Sized Iron Oxide Nanoparticles for High-Resolution Magnetic Resonance Imaging Contrast Agents. *Journal of the American Chemical Society* 133(32), pp.12624-12631.

Kim, B.Y.S., Rutka, J.T., & Chan, W.C.W., 2010. Nanomedicine. *The New England Journal of Medicine*, 363, pp. 2434-43.

Kourki, H. & Famili, M.H.N., 2011. Particle-sedimentation: effect of polymer concentration on particle-particle interaction. *Poweder Technology*, 221, pp.137-43.

Krpetić, Z., Porta, F., Caneva, E., Del Santo, V., Scarì, G., 2010. Phagocytosis of biocompatible gold nanoparticles. *Langmuir*, 26(18), pp.14799-805.

Latham, A.H., Freitas, R.S., Schiffer, P., and Willams, M.E., 2005. Capillary Magnetic Field Flow Fractionation and Analysis of Magnetic Nanoparticles. *Analytical Chemistry*, 77, pp.5055-62.

Laurent, S., Forge, D., Port, M., Roch, A., Robic, C., Elst, L.V., & Muller, R.N., 2008. Magnetic Iron Oxide Nanoparticles: Synthesis, Stabilization, Vectorization, Physiochemical Characterizations, and Biological Applications. *Chemical Reviews*, 108, pp.2064-110.

Lee, H.Y., Li, Z., Chen, K., Hsu, A.R., Xu, C., Xie, J., Sun, S., & Chen, X., 2008. PET/MRI Dual-Modality Tumor Imaging Using Arginine-Glycine-Aspartic (RGD)-Conjugated Radiolabeled Iron Oxide Nanoparticles. *Journal of Nuclear Medicine*, 49(8), pp.1371-379.

Lee, Y., Lee, J., Bae, C.J., Park, J.G., Noh, H.J, Park, J.H. & Hyeon, T., 2005. Large-Scale Synthesis of Uniform and Crystalline Magnetite Nanoparticles Using Reverse Micelles as Nanoreactors under Reflux Conditions. *Advanced Functional Materials* 15(3), pp.503-509.

Li, S. & Huang, L., 2008. Pharmacokinetics and Biodistribution of Nanoparticles. *Molecular Pharmaceutics*, 5(5), pp. 496-504.

Lodhia, J., Mandarano, G., Ferris, N., Eu, P., & Cowell, S., 2010. Development and Use of Iron Oxide Nanoparticles: Synthesis of Iron Oxide Nanoparticles for MRI. *Biomedical Imaging and Intervention Journal,* 6(2), e(12).

Maeda, H., Wu, J., Sawa, T., Matsumura, Y., & Hori, K., 2000. Tumor vascular permeability and the EPR effect in macromolecular therapeutics: a review. *Journal of Controlled Release*, 65(1-2), pp.1721-30.

Martinez-Möller, A., Eiber, M., Nekolla, S.G., Souvatzoglou, M., Drzezga, A., Ziegler, S., Rummeny, E.J., Schwaiger, M., & Beeer, A.J., 2012. Workflow and Scan Protocol Consideration for Integrated Whole-Body PET/MRI in Oncology. *Journal of Nuclear Medicine*, 53:9, pp. 1415-26.

Meyer, C., Hahn, U., & Rentmeister, A., 2011. Cell-Specific Aptamers as Emerging Therapeutics. *Journal of Nucleic Acids*, 2011, pp.1-18.

Meyer, H.A., Ahrens-Fath, I., Sommer, A., & Haendler, B., 2004. Novel Molecular Aspects of Prostate Carcinogenesis. *Biomedicine & Pharmacotherapy*, 58(1), pp.10-16.

Moghimi, S.M., Andersen, A.J., Hashemi, S.H., Lettiero, B., Ahmadvand, D., Hunter, A.C., Andresen, T.L. Hamad, I., & Szebeni, J., 2010. Complement activation cascade triggered by PEG-PL engineered medicines and carbon nanotubes: The challenges ahead. *Journal of Controlled Release*, 146(2), pp.175-81.

Moghimi, S.M., Hunter, A.C., & Murray, J.C., 2001. Long-Circulating and Target-Specific Nanoparticles: Theory to Practice. *Pharmalogical Reviews*, 53(2), pp.283-18.

Moghimi, S.M., Hunter, A.C., Murray, J.C., 2005. Nanomedicine: current progress and future prospects. *The FASEB Journal*, 19, pp.311-30.

Moghimi, S.M., Hunter, A.C., Andresen, T.L., 2012. Factors Controlling Nanoparticle Pharmacokinetics: An Integrated Analysis and Perspective. *Annual Review of Pharmacology and Toxicology*, 52, pp.481-503.

Moghimi, S.M., Porter, C.J.H., Muir, I.S., Illum, L., & Davis, S.S., 1991. Non-phagocytic uptake of intravenously injected microspheres in rat spleen: influence of size and hydrophilic coating. *Biochemical and Biophysical Research Communications*, 177, pp.766-68.

Naqvi, S., Samim, M., Abdin, M.Z., Ahmed, F.J, Maitra, A.N., Prashant, C.K., Dinda, A.K., 2010. Concentration-dependent toxicity of iron oxide nanoparticles mediated by increased oxidative stress. *International Journal of Nanomedicine*, 5, pp.983-89.

Padhani, A., 2000. Dynamic Contrast Enhanced MRI of Prostate Cancer: Correlation with Morphology and Tumour Stage, Histological Grade and PSA,. *Clinical Radiology*, 55(2), pp.99-109.

Pankhurst, Q.A., Connolly, J., Jones, S.K., & Dobson, J., 2003. Applications of magnetic nanoparticles in biomedicine. *Journal of Physics D: Applied Physics*, 36, pp.R167-R181.

Parry, David A., Booth, Timothy, Roland, Peter. Advantages of Magnetic Resonance Imaging over Computed Tomography in Preoperative Evaluation of Pediatric Cochlear Implant Candidates. Otology & Neurotology 26:976–982. 2005.

Patel, H.M., 1992. Serum opsinins and liposomes: their interaction and opsonophagocytosis. *Critical Reviews in Therapeutic Drug Carrier Systems*, 9, pp.39-90.

Perrault, S.D., Walkey, C., Jennings, T., Fischer, H.C., & Chan, W.C.W., 2009. Mediating Tumor Targeting Efficiency of Nanoparticles Through Design. *Nano Letters*, 9(5), pp.1909-915.

Petersson, F., Aberg, L., Sward-Nilsson, A., & Laurell, T., 2007. Free Flow Acoustophoresis: Microfluidic-Based Mode of Particle and Cell Separation. *Analytical Chemistry*, 79:14, pp. 5117-213.

Qiao, R., Chunhui, Y., & Gao, M., 2009. Superparamagnetic Iron Oxide Nanoparticles: From Preparations to in Vivo MRI Applications. *Journal of Materials Chemistry*, 19(35), pp. 6274.

Ranganathan, R., Madanmohan, S., Kesavan, A., Baskar, G., Krishnamoorthy, Y.R., Santosham, R., Ronraju, D., Rayala, S.K., Venkatraman, G., 2012. Nanomedicine: towards development of patient-friendly drug-delivery systems for oncological applications. *International Journal of Nanomedicine*, 7, 1043-60.

Renshaw, P.F., Owen, C.S., McLaughlin, A.C., Frey, T.G., & Leigh, J.S., 1986. Ferromagnetic Contrast Agents: A New Approach. *Magnetic Resonance in Medicine* 3(2), pp.217-25.

Roca, A.G., Veintemillas-Verdaguer, S., Port, M., Robic, C., Serna, C.J., & Morales, M.P., 2009. Effect of nanoparticle and Aggregate Size on the Relaxometric Properties of MR Contrast Agents Based on High Quality Magnetite Nanoparticles. *Journal of Physical Chemistry*, 113, pp. 7033-39.

Segur, J.B., & Oberstar, H.E., 1951. Viscosity of Glycerol and Its Aqueous Solutions. *Industrial and Engineering Chemistry*, 43:9, pp.2117-20.

Shah RV, Smith HK, Chung J, Hegazi A, Racz GB. Cervical spinal cord neoplasm in a patient with an implanted cervical spinal cord stimulator: the controversial role of magnetic resonance imaging. Pain Physician. 2004 Apr;7(2):273-8.

Shevkoplyas, S.S., Siegel, A.A., Westervelt, R.M., Prentiss, M.G., & Witesides, G.M., 2007. The force acting on a superparamagnetic bead due to an applied magnetic field. *Lab Chip*, 7, pp.1294-302.

Suetens, P., 2002. *Fundamentals of Medical Imaging*. Cambridge, UK: Cambridge University Press.

Tartaj, P., & Serna, C.J., 2002. Microemulsion-Assisted Synthesis of Tunable Superparamagnetic Composites. *Chemistry of Materials*, 14:10, pp. 4396-402.

Thorek, D.L.J. & Tsourkas, A., 2008. Size, charge, and concentration dependent uptake of iron oxide particles by non-phagocytic cells. *Biomaterials*, 29, pp.3583-3590.

Tromsdorf, U.I., Bigall, N.C., Kaul, M.G., Bruns, O.T., Nikolic, M.S., Mollwitz, B., Sperling, R.A., Reimer, R., Hohenberg, H., Parak, W.J., Förster, S., Beisiegel, U., Adam, G., & Weller, H., 2007. Size and Surface Effects on the MRI Relaxivity of Manganese Ferrite Nanoparticle Contrast Agents. *Nano Letters*, 7:8, pp. 2422-27.

Xie, J., Huang, J., Li, X., Sun, S., & Chen, X., 2009. Iron Oxide Nanoparticle Platform for Biomedical Applications. *Current Medicinal Chemistry*, 16, pp.1278-294.

Walkey, C.D. & Chan, W.C.W., 2012. Understanding and controlling the interaction of nanomaterials with proteins in the physiological environment. *Chemical Society Reviews*, 41, pp.2780-799.

Walkey, C.D., Olsen, J.B., Guo, H., Emili, A., Chan, W.C.W, 2011. Nanoparticle Size and Surface Chemistry Determine Serum Protein Adsorption and Macrophage Uptake. *Journal of the America Chemical Society*, 134, pp.2139-147.

Win, K.Y. & and Feng, S., 2004. Effects of particle size and surface coating on cellular uptake of polymeric nanoparticles for oral delivery of anticancer drugs. *Biomaterials*, 26, pp.2713-722.

Yoon, S.J., Soo, Y.J., Kwon, A.S., Kang, S.H., Jeong, Y.Y., Park, I.K., Cho, C.S., Kim, Y.K., Kim, W.J., & Namgung, R., 2012. MRI Contrast Agent Coated with Carboxylated Mannan and Method for Producing the Same. Intron Biotechnology, INC., assignee. Patent 20120230919.

Yuan, F., Dellian, M., Fukumura, D., Leunig, M., Berk, D.A., Torchilin, V.P., & Jain, R.K., 1995. Vascular Permeability in a Human Tumor Xenograft: Molecular Size Dependence and Cutoff Size. *Cancer Research*, 55, pp.3752-756.

Appendix A

Iron Concentration and Corresponding R$_2$ Value Tables for MRI Experiments

Region of Interest	Concentration × 10^3 (mg/mL)	R_2 (s^{-1})
1	66.4	-
2	33.2	234.2
3	16.6	102.2
4	8.3	44.9
5	4.2	13.46
6	2.1	5.99
7	1.0	2.44
8	0.52	2.12
9	0.26	1.996
10	0.13	1.11
11	0.065	1.73
12	0.032	1.342
13	0.016	0.695
14	0.008	0.695
15	0.004	0.697
16	0.00	0.662

Table A.1 Concentration and relaxivity data for initial MRI scan using MNP-O distribution.

		R$_2$ Values, s^{-1}		
Row	Iron Concentration mg/mL	A	B	C
1	0.0182	11.20	51.05	25.90
2	0.0091	5.16	27.87	14.30
3	0.0046	2.90	10.44	6.00
4	0.0008	1.51	2.96	2.33
5	0.0004	1.18	2.02	1.64
6	0.0002	0.80	1.44	0.121

Table A.2 Concentration and relaxivity data for MRI scan of the dilutions of the (A) MNP-95, (B) MNP-151, and (C) MNP-O distributions.

		R_2 Values, s^{-1}			
Row	Iron Concentration mg/mL	A	B	C	D
1	0.025	-	-	-	-
2	0.020	-	-	-	-
3	0.015	125.11	148.01	147.57	141.61
4	0.010	66.61	43.88	25.39	76.00
5	0.005	27.41	20.14	22.45	28.98
6	0.0025	8.09	18.28	21.34	4.46
7	0.001	2.32	8.26	5.06	2.59

Table A.3 Concentration and relaxivity data for MRI scan of the dilutions of the (A) MNP-O, (B) MNP-96, (C) MNP-124, and (D) MNP-142 distributions.

Iron Concentration mg/mL	$R2, s^{-1}$			
	MNP-O	MNP-96	MNP-124	MNP-142
0.015	73.87	94.93	84.92	81.35
0.01	50.68	52.74	50.06	56.65
0.005	36.96	35.32	38.18	39.40
0.0025	34.79	36.51	38.54	38.88
0.001	35.19	36.11	35.26	39.35
0.0	36.80	36.80	36.80	36.80

Table A.4 Concentration and relaxivity data used to determine the expected R_2 values through the artificial diffusion gradients.

Appendix B

DLS Size Distributions for Various Flow Rates Using Magnetic Separation

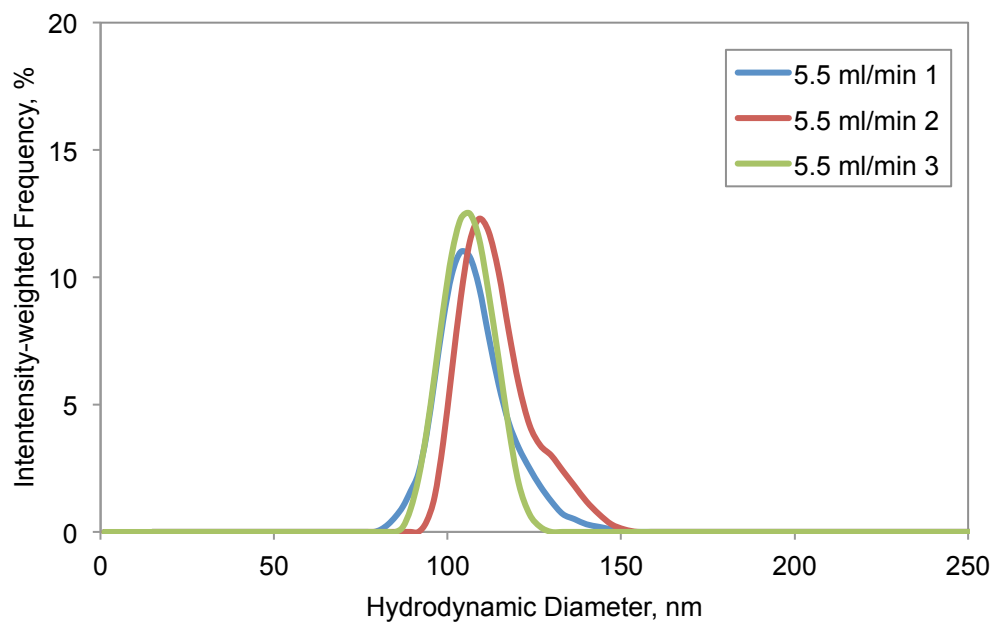**Prototypes Illustrating the Repeatability of Each Design**
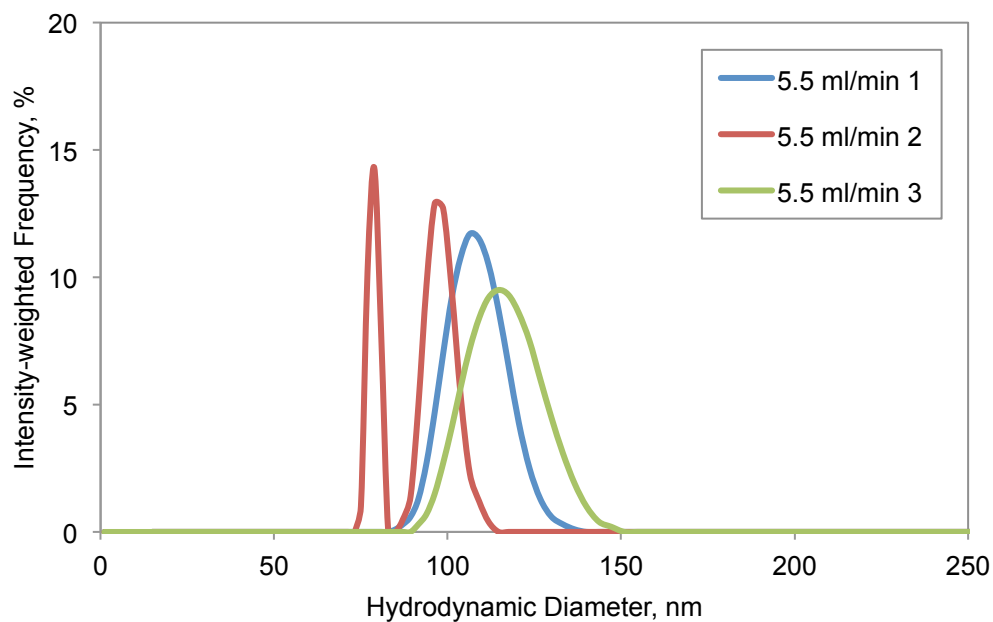
Figure B.1 DLS size distributions obtained for the triplicate experiments run using the MagLine prototype at a flow rate of 5.5 mL/min.
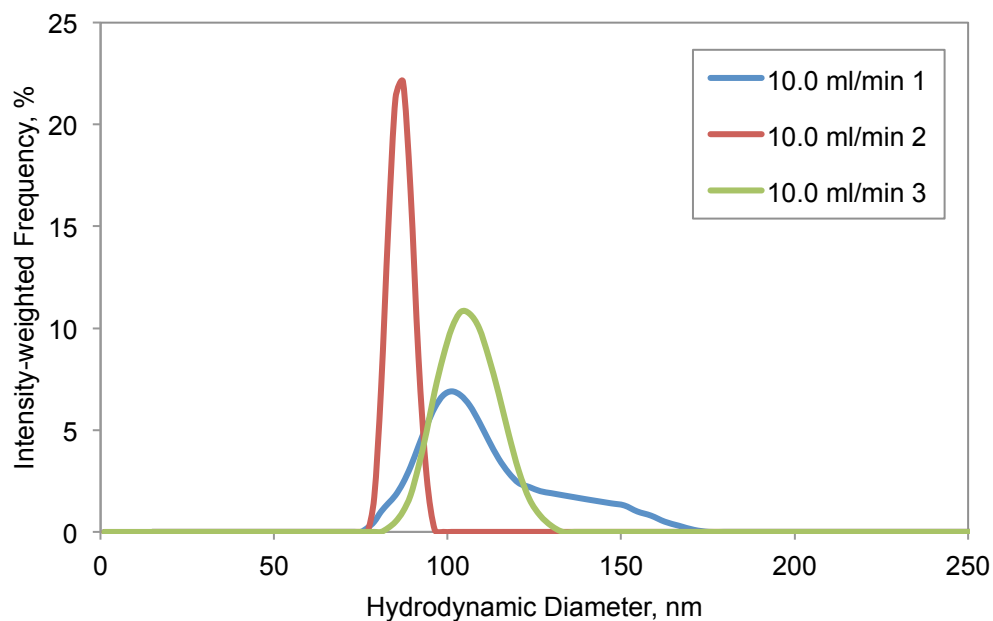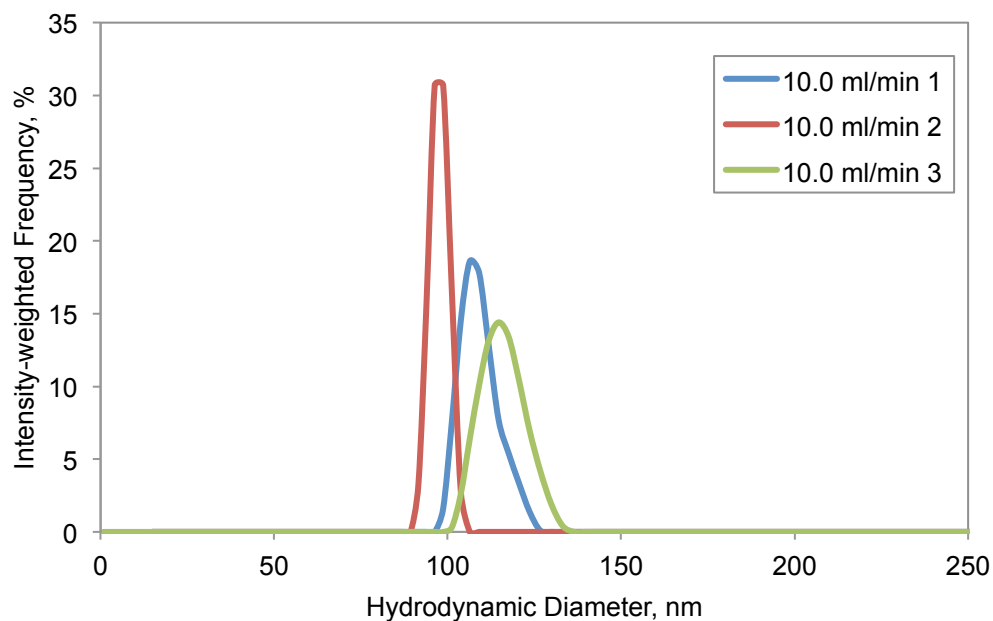

Figure B.2 DLS size distributions obtained for the triplicate experiments run using the MagLine prototype at a flow rate of 10.0 mL/min.
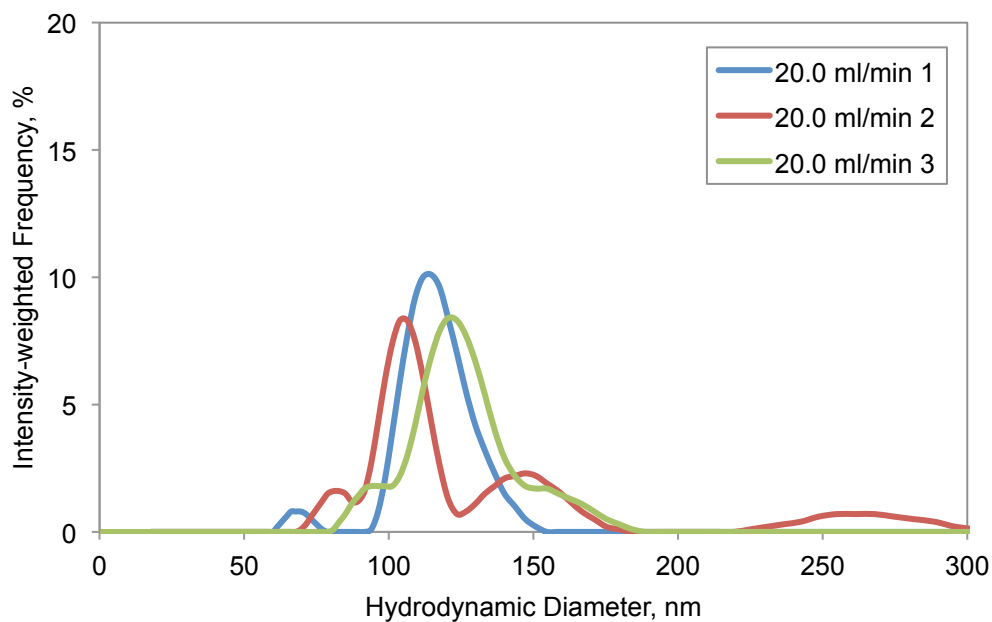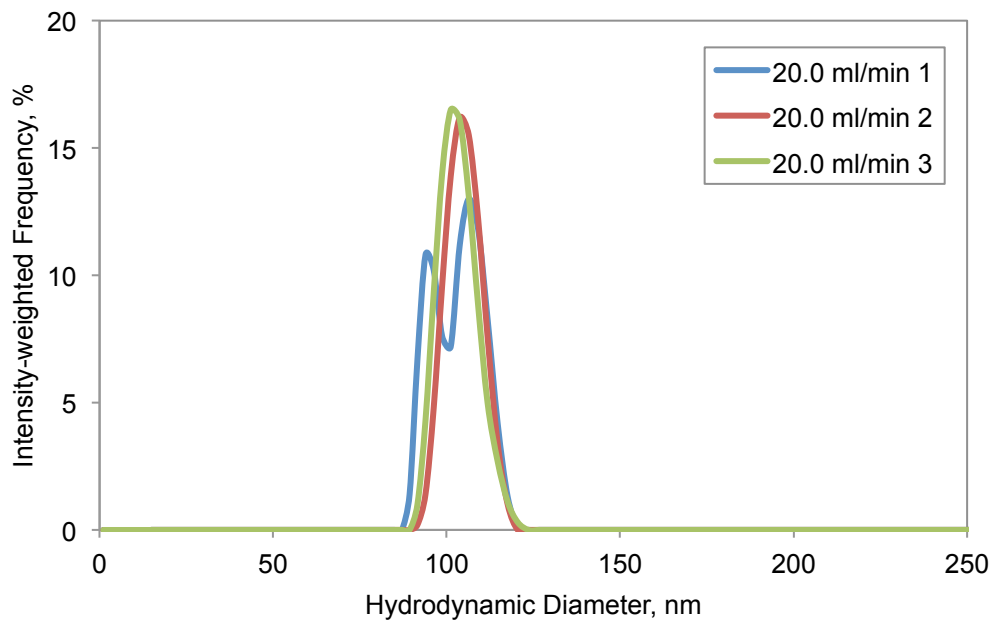
Figure B.3 DLS size distributions obtained for the triplicate experiments run using the MagLine prototype at a flow rate of 20.0 mL/min.
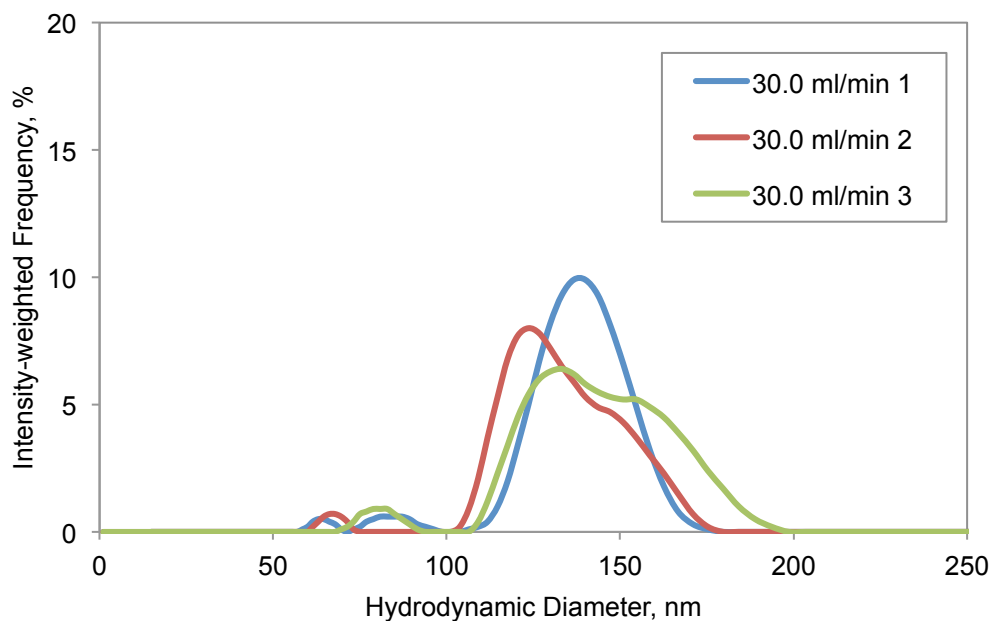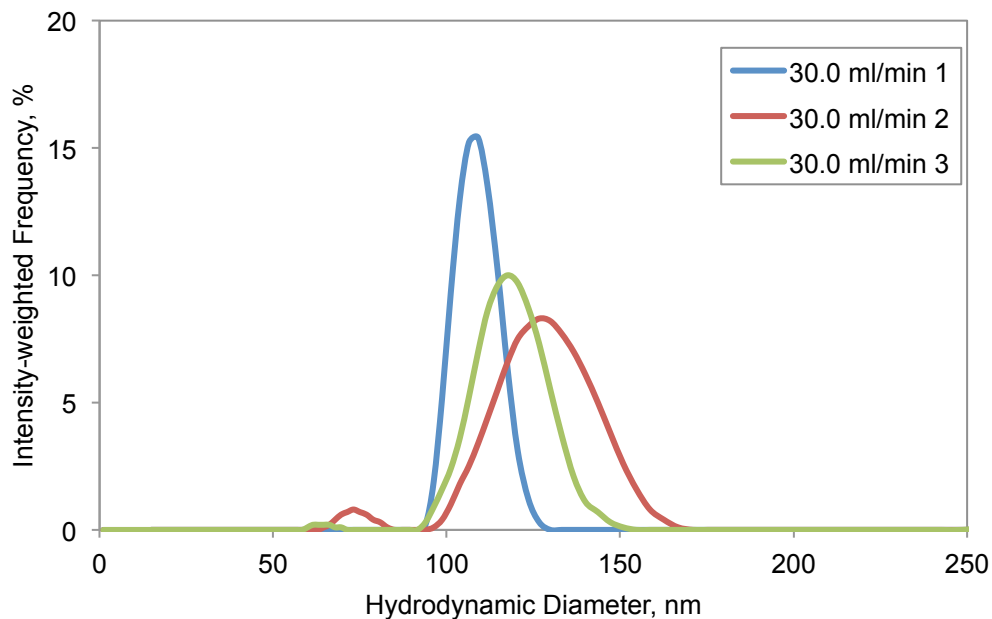

Figure B.4 DLS size distributions obtained for the triplicate experiments run using the MagLine prototype at a flow rate of 30.0 mL/min.
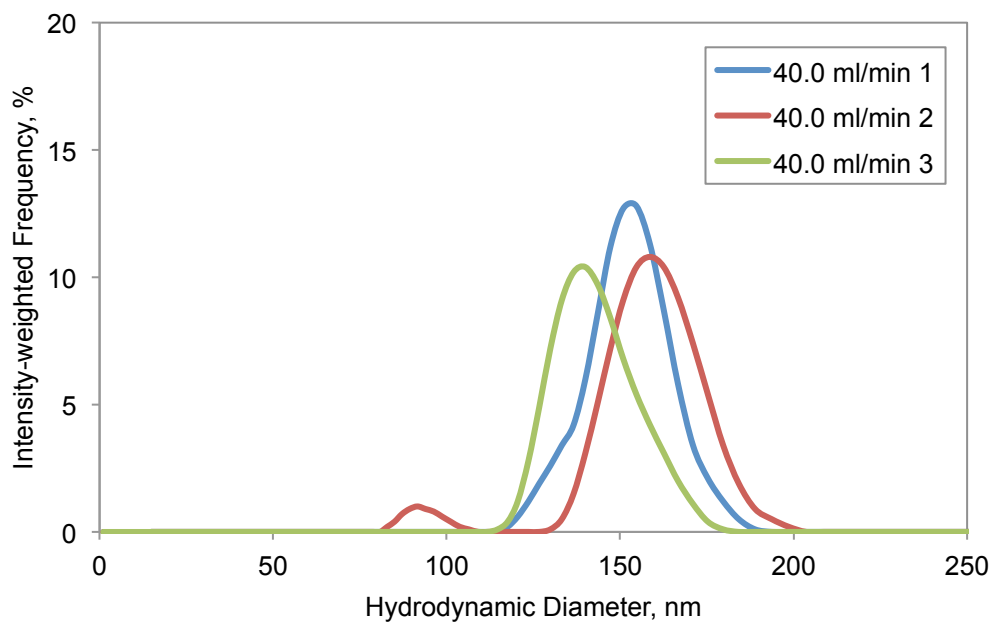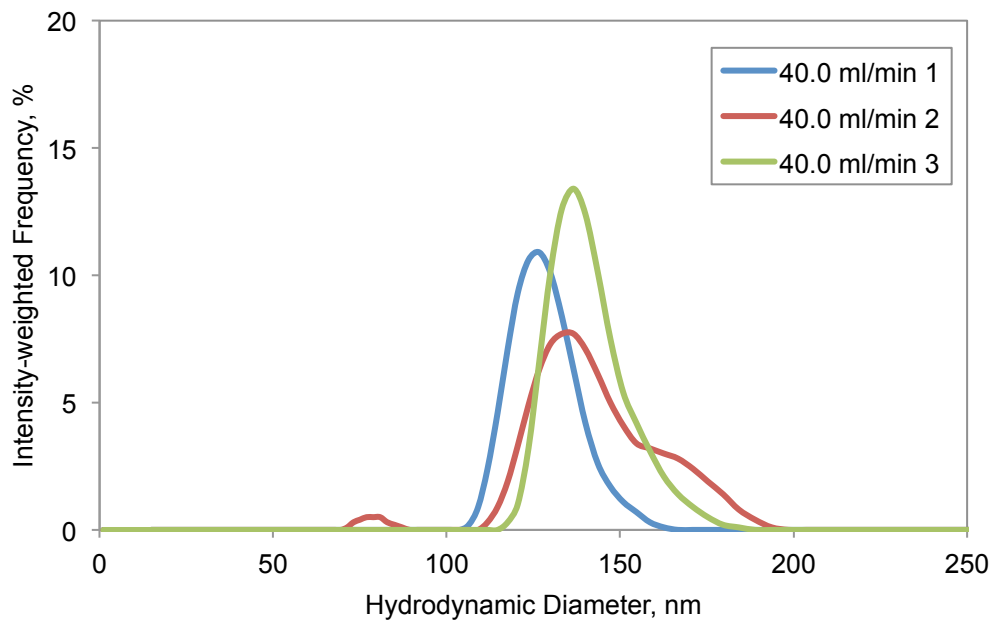
Figure B.5 DLS size distributions obtained for the triplicate experiments run using the MagLine prototype at a flow rate of 40.0 mL/min.
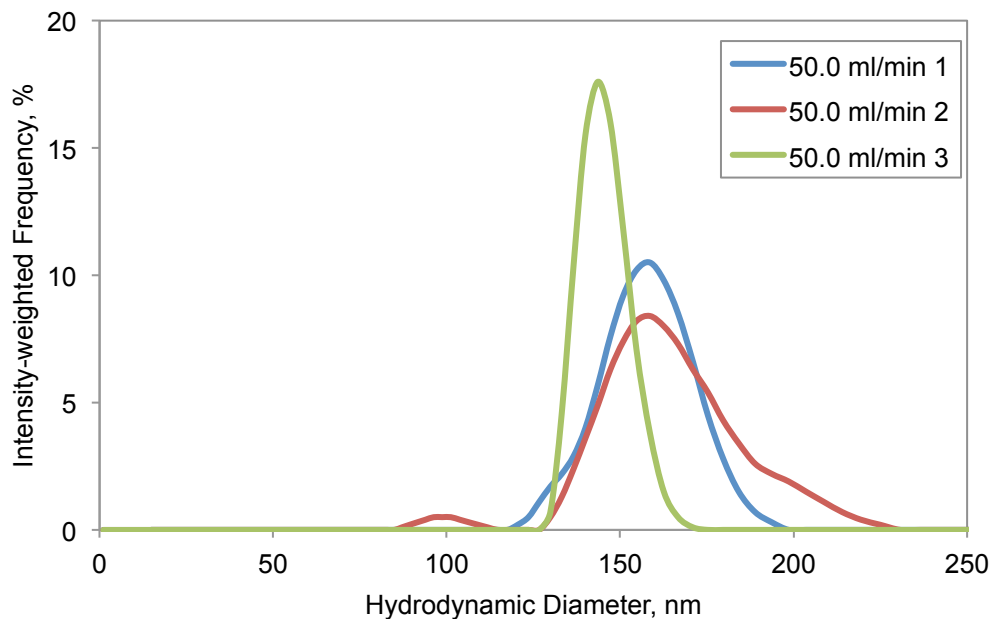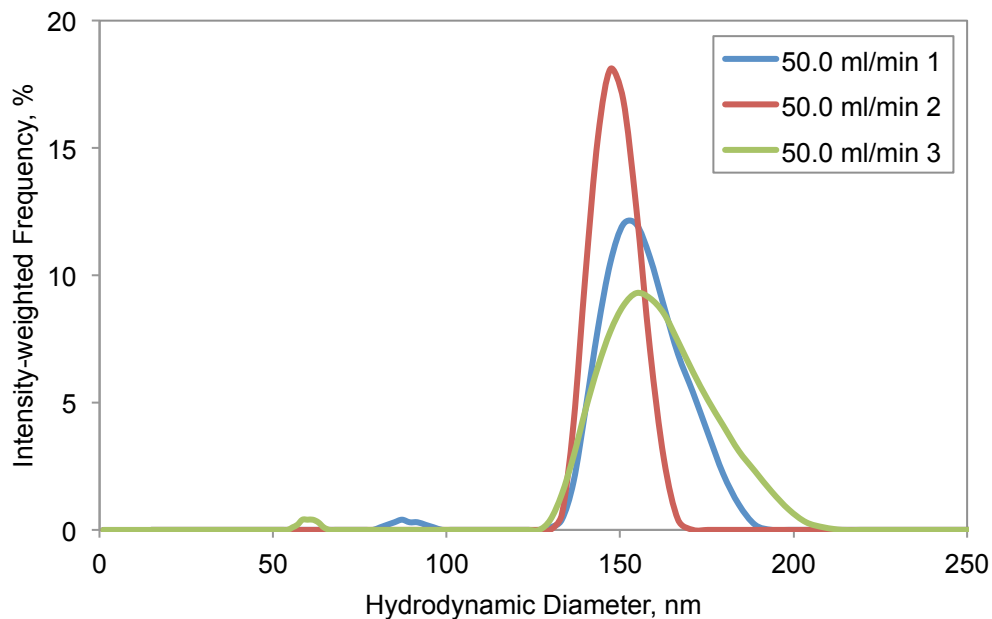

Figure B.6 DLS size distributions obtained for the triplicate experiments run using the MagLine prototype at a flow rate of 50.0 mL/min.
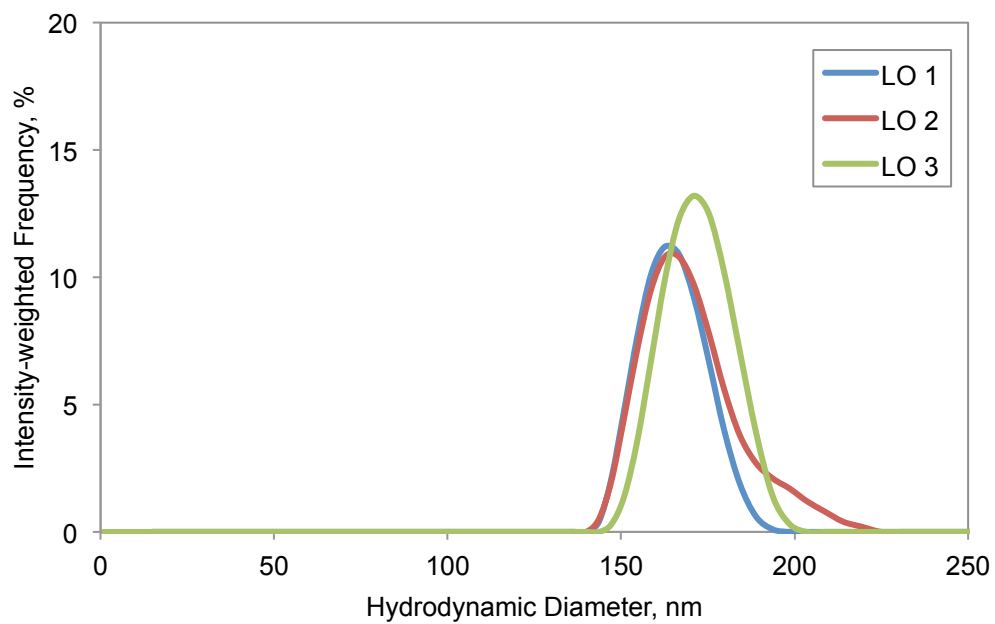
Figure B.7 DLS size distributions obtained for the triplicate experiments run using the MagLine prototype for the MNPs retained after all flow rates were applied.

Figure B.8 DLS size distributions obtained for the triplicate experiments run using the MagWrap prototype at a flow rate of 5.5 mL/min.

Figure B.9 DLS size distributions obtained for the triplicate experiments run using the MagWrap prototype at a flow rate of 10.0 mL/min.

Figure B.10 DLS size distributions obtained for the triplicate experiments run using the MagWrap prototype at a flow rate of 20.0 mL/min.
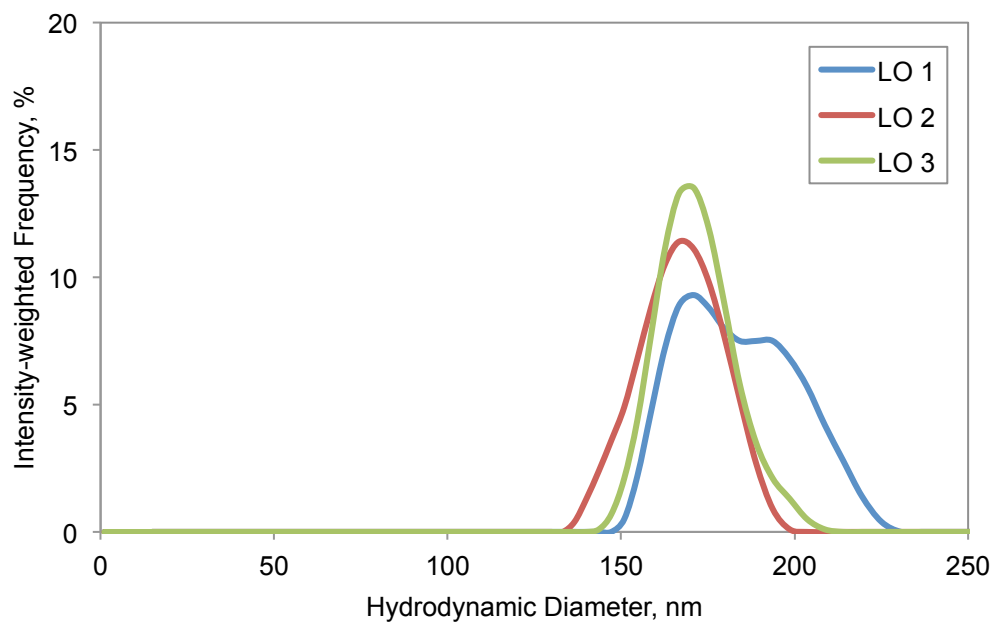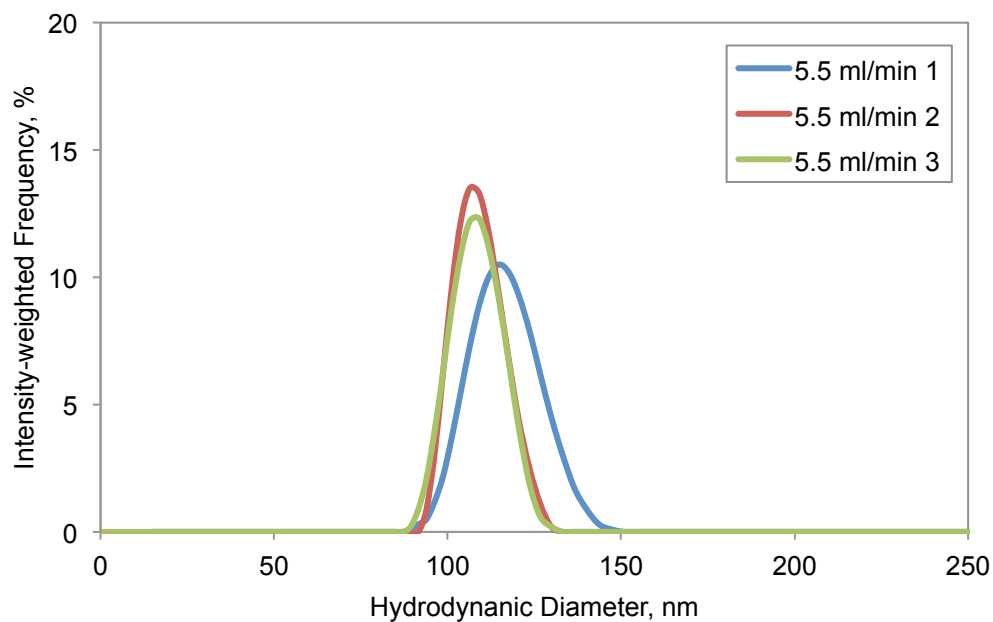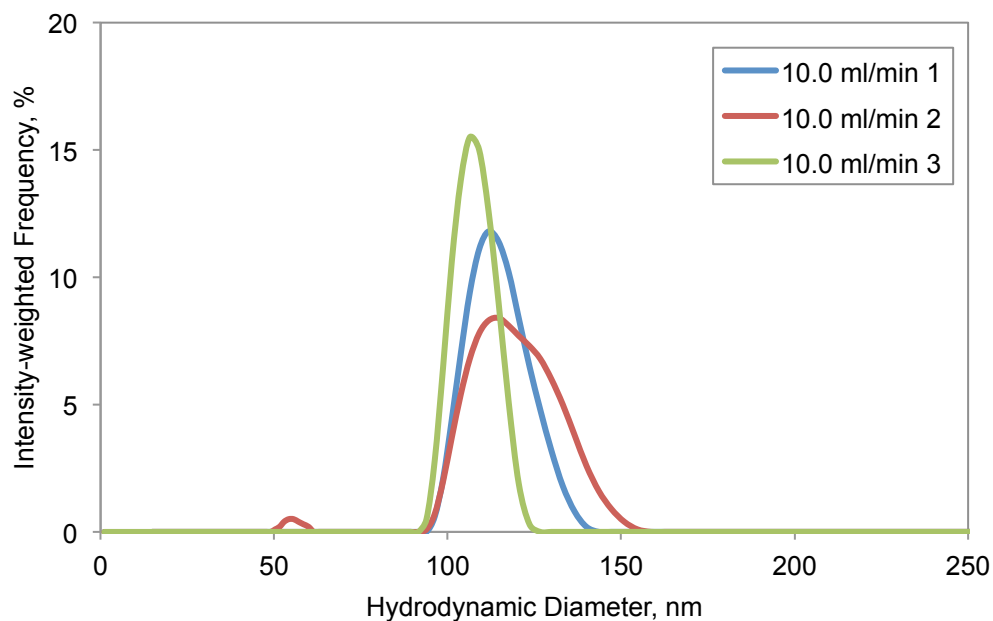

Figure B.11 DLS size distributions obtained for the triplicate experiments run using the MagWrap prototype at a flow rate of 30.0 mL/min.

Figure B.12 DLS size distributions obtained for the triplicate experiments run using the MagWrap prototype at a flow rate of 40.0 mL/min.

Figure B.13 DLS size distributions obtained for the triplicate experiments run using the MagWrap prototype at a flow rate of 50.0 mL/min.

Figure B.14 DLS size distributions obtained for the triplicate experiments run using the MagWrap prototype for the MNPs retained after all flow rates were applied.

Figure B.15 DLS size distributions obtained for the triplicate experiments run using the MagCoil prototype at a flow rate of 5.5 mL/min.

Figure B.16 DLS size distributions obtained for the triplicate experiments run using the MagCoil prototype at a flow rate of 10.0 mL/min.
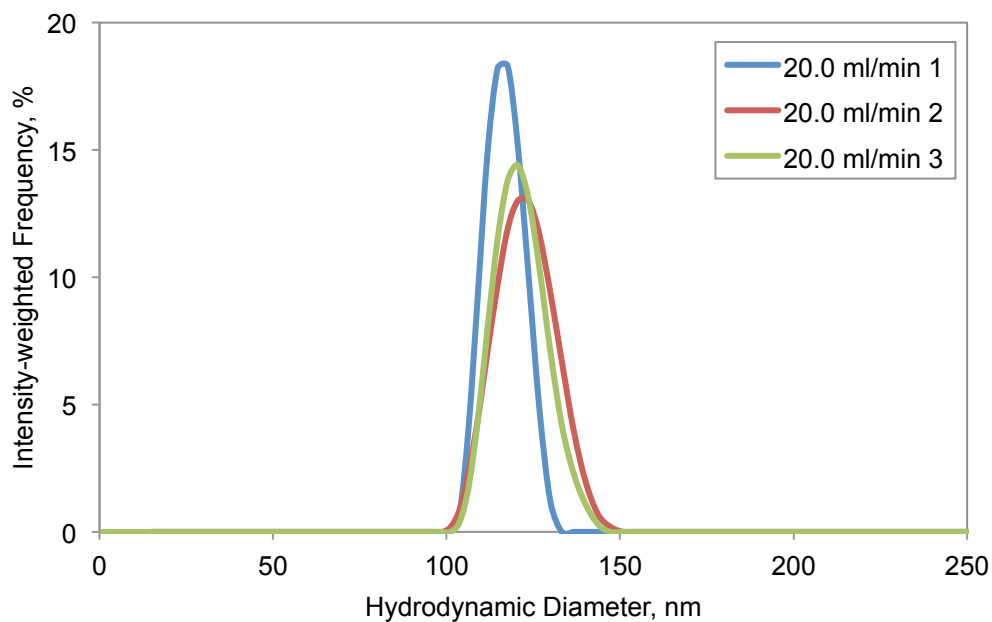
Figure B.17 DLS size distributions obtained for the triplicate experiments run using the MagCoil prototype at a flow rate of 20.0 mL/min.
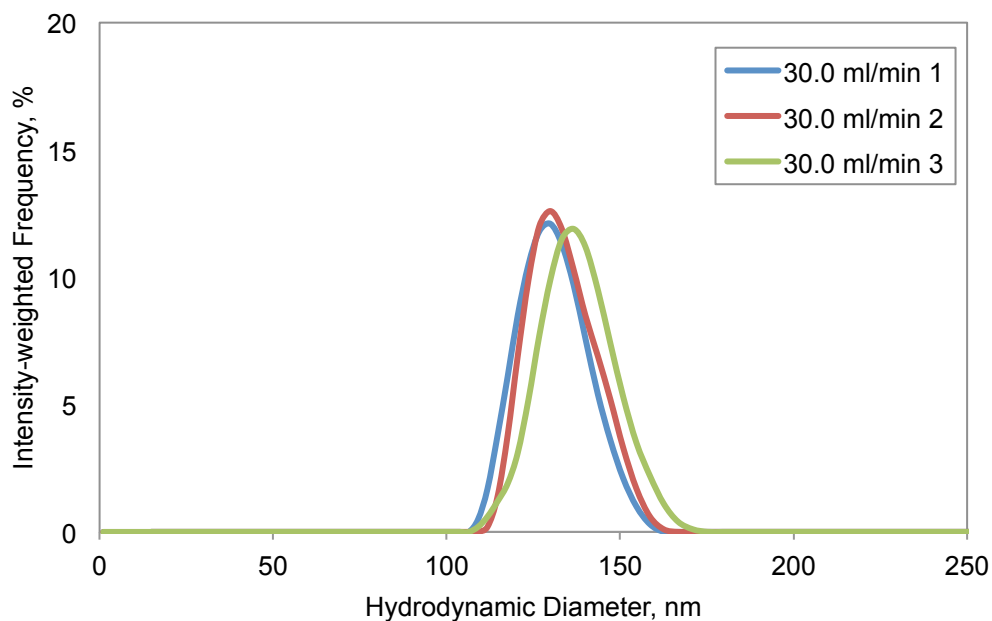

Figure B.18 DLS size distributions obtained for the triplicate experiments run using the MagCoil prototype at a flow rate of 30.0 mL/min.
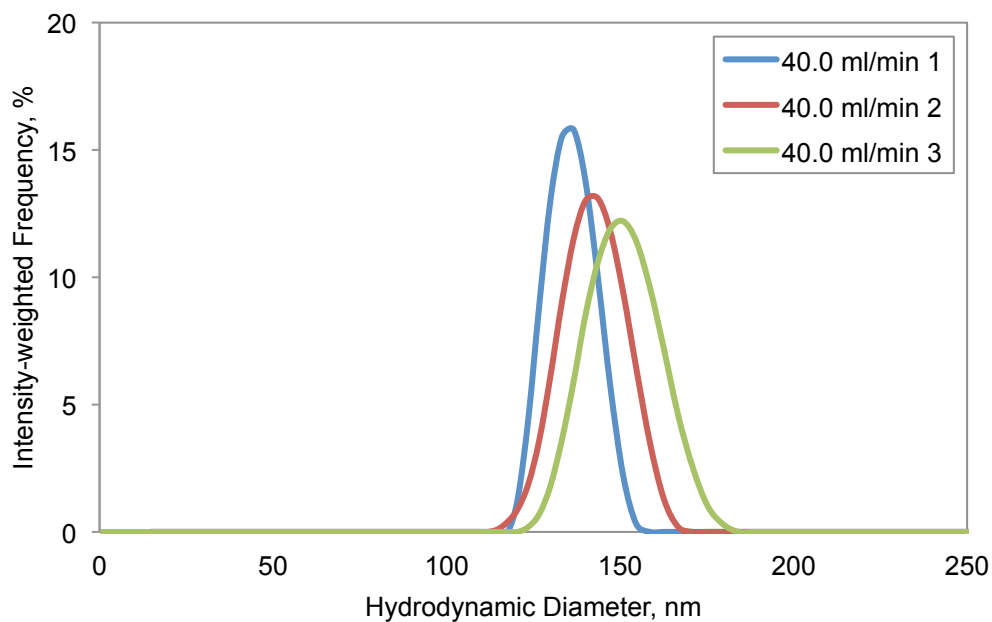
Figure B.19 DLS size distributions obtained for the triplicate experiments run using the MagCoil prototype at a flow rate of 40.0 mL/min.
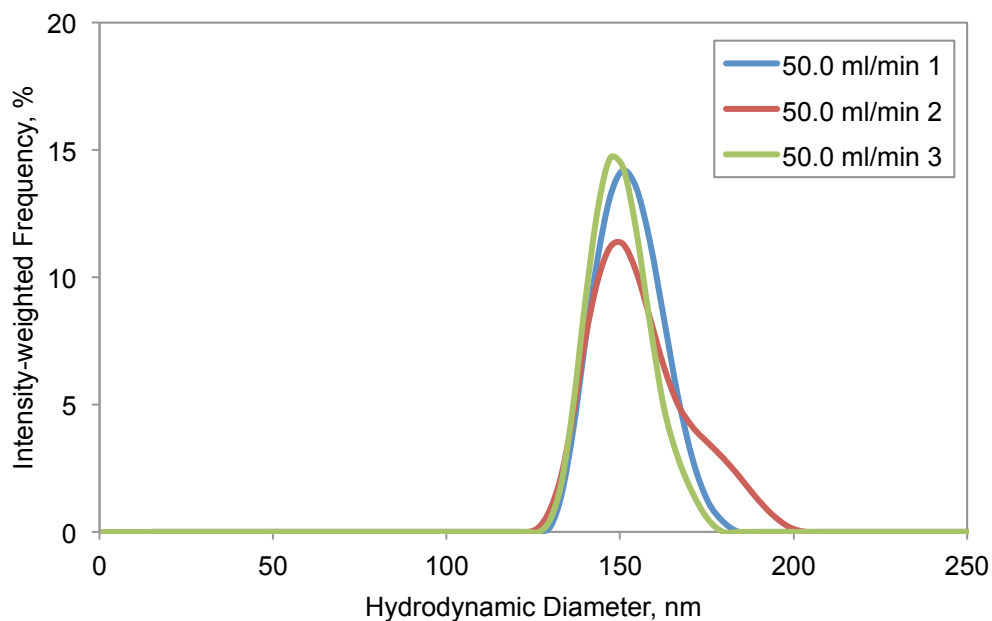

Figure B.20 DLS size distributions obtained for the triplicate experiments run using the MagCoil prototype at a flow rate of 50.0 mL/min.
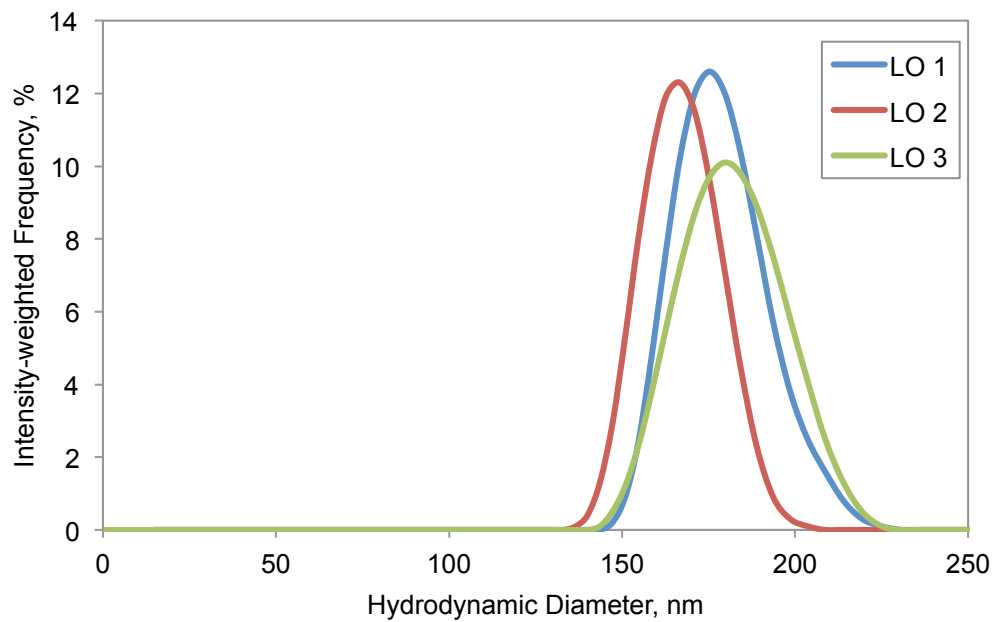
Figure B.21 DLS size distributions obtained for the triplicate experiments run using the MagCoil prototype for the MNPs retained after all flow rates were applied.